

Anne-Marte Padøy Mathiesen

# Towards the incorporation of surface acoustic waves for improving the detection of nanoplasmonic biosensors

Master's thesis in Mechanical Engineering

Supervisor: Carlos Alberto Dorao

Co-supervisor: Diego Sánchez Saldaña

March 2021





Anne-Marte Padøy Mathiesen

# **Towards the incorporation of surface acoustic waves for improving the detection of nanoplasmonic biosensors**

Master's thesis in Mechanical Engineering  
Supervisor: Carlos Alberto Dorao  
Co-supervisor: Diego Sánchez Saldaña  
March 2021

Norwegian University of Science and Technology  
Faculty of Engineering  
Department of Energy and Process Engineering





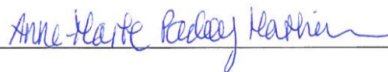
---

# Preface

This master thesis, titled "Towards the incorporation of surface acoustic waves for improving the detection of nanoplasmonic biosensors" concludes the work assigned during the fall of 2020. The work, worth 30 ECTS, has been conducted as part of the Master of Science program "Mechanical Engineering" at the Norwegian University of Science and Technology (NTNU).

I want to direct appreciation and gratitude to my supervisor Carlos Alberto Dorao for his support and guidance throughout the master thesis. I would also like to thank my co-supervisor Diego Sánchez Saldaña, and Gonzalo Almanza Álvarez and Ricardo Matías Trujillo for discussions and advice.

Trondheim, March 8, 2021



---

Anne-Marte Padøy Mathiesen

Please note that neither the institution nor the examiners are responsible - through the approval of this thesis - for the theories and methods used or the conclusions drawn in this work.

---

---

# Abstract

Cancer is one of the leading causes of death worldwide. With the World Health Organization predicting an increase in the number of new cancer cases, early cancer detection and diagnosis will be key factors to decrease mortality and increase the survival rate. Therefore, numerous reliable measurement techniques and methods for biomarker detection have been developed. A promising approach is localized surface plasmon resonance-based biosensors that yield high sensitivity and specificity from the optical properties of the employed metallic nanostructures. By incorporating microfluidics and acoustofluidics, the detection and sensitivity performance of the biosensor can be enhanced. This is accomplished by increasing the contact between the sensor and the nanoparticles of interest through the utilization of surface acoustic waves inducing microfluidic mixing.

Three active surface-acoustic-wave-driven micromixers with frequencies of 40, 80, and 120 MHz have been experimentally tested at the NTNU acoustofluidics test facility. The mixing efficiency through internal streaming has been investigated for different flow rates and power applications. The experimental results revealed a reduction in the induced mixing speed for higher flow rates and a decrease in the mixing efficiency for lower power inputs. The 40 MHz interdigital transducer (IDT) design was not found to be more efficient than the 80 MHz IDT design, which differs from the findings in the literature. However, it was observed that the 120 MHz IDT design displayed a reduction in the mixing efficiency compared to the 40 MHz and 80 MHz IDT designs. The dual IDT showed an enhanced mixing performance compared to the single IDT for certain power inputs. However, considering the total energy input into the system, the mixing efficiency for the single and dual IDT did not display any considerable mixing performance differences. The highest mixing efficiency obtained was 97.93% for the dual IDT of the 80 MHz IDT design at a flow rate of  $500 \mu\text{L}/\text{h}$  and power input of 1500 mW.

The experimental results for the nanoplasmonic sensors documented that hexagonal nanohole arrays generally obtained higher sensitivity than square nanohole alignments. A thicker gold layer on the sensor resulted in higher sensitivity values and sharper spectrum curves. A significant effect on the sensor sensitivity was observed for various polynomial curve fitting orders. The maximum sensitivity of 285.8275 nm/RIU was achieved for the nanoplasmonic sensor with a hexagonal nanohole array, nanohole diameters of 400 nm, a 250 nm gold layer thickness, and a periodicity of 1000 nm.

---

# Sammendrag

Kreft er en av de ledende dødsårsakene i verden. Med Verdens helseorganisasjon sin forventede økning i antall nye krefttilfeller, vil tidlig kreftpåvisning og -diagnose være nøkkelfaktorer for å redusere dødeligheten og øke overlevelsesraten. Derfor er det utviklet mange pålitelige måleteknikker og metoder for påvisning av biomarkører. En lovende tilnærming er lokale overflateplasmonresonansbaserte biosensorer som gir høy sensitivitet og spesifisitet fra de optiske egenskapene til de anvendte metalliske nanostrukturene. Ved å inkorporere mikrofluidikk og akustofluidikk kan deteksjons- og sensitivitetsytelsen til biosensoren forbedres. Dette oppnås ved å øke kontakten mellom sensoren og nanopartiklene av interesse ved bruk av akustiske overflatebølger som forårsaker mikrofluidisk miksing.

Tre aktive overflate-akustisk-bølgedrevne mikromiksere med frekvenser på 40, 80 og 120 MHz er eksperimentelt testet ved testanlegget for akustofluidikk på NTNU. Blandingseffektiviteten gjennom intern strømming har blitt undersøkt for forskjellige strømningsrater og energitilførsler. De eksperimentelle resultatene ga en reduksjon i den induerte blandingshastigheten for høyere strømningsrater og en reduksjon i blandingseffektiviteten for lavere energitilførsler. Det 40 MHz interdigitale transduserdesignet (IDT designet) ble ikke funnet til å være mer effektiv enn det 80 MHz IDT designet, noe som avviker fra funnene i litteraturen. Det ble imidlertid observert at det 120 MHz IDT designet viste en reduksjon i blandingseffektiviteten sammenlignet med de 40 MHz og 80 MHz IDT designene. En dobbel IDT viste en forbedret blandingsytelse sammenlignet med en enslig IDT for bestemte energitilførsler. Det ble derimot observert at blandingseffektiviteten for en enslig IDT og en dobbel IDT ikke ga betydelige forskjeller når den totale energitilførselen til systemet ble betraktet. Den høyeste oppnådde blandingseffektiviteten var på 97.93% for en dobbel IDT for det 80 MHz IDT designet med en strømningsrate på  $500 \mu\text{L}/\text{h}$  og energitilførsel på 1500 mW.

De eksperimentelle resultatene for de nanoplasmoniske sensorene dokumenterte at sekskantede nanohullarrangement generelt oppnådde høyere sensitivitet enn firkantede nanohullarrangement. Et tykkere gullag på sensoren resulterte i høyere sensitivetsverdier og skarpere spektrumkurver. En betydelig effekt på sensitiviteten til sensoren ble observert for forskjellige ordre av polynomtilpasningskurvene. Den maksimale sensorsensitiviteten på 285.8275 nm/RIU ble oppnådd for en nanoplasmonisk sensor med et sekskantet nanohullarrangement, nanohulldiameterer på 400 nm, en 250 nm gullykkelse og en periodisitet på 1000 nm.

# Table of Contents

<b>Preface</b>	<b>I</b>
<b>Abstract</b>	<b>I</b>
<b>Sammendrag</b>	<b>II</b>
<b>Table of Contents</b>	<b>VI</b>
<b>List of Tables</b>	<b>VIII</b>
<b>List of Figures</b>	<b>XV</b>
<b>Nomenclature</b>	<b>XVI</b>
<b>1 Introduction</b>	<b>1</b>
1.1 Background . . . . .	1
1.2 Scope of Thesis . . . . .	2
1.3 Limitations of Scope . . . . .	3
1.4 Information Retrieval . . . . .	3
1.5 Report Structure . . . . .	3

---

<b>2</b>	<b>Fundamentals of Nanoparticle Detection and Manipulation</b>	<b>5</b>
2.1	Exosomes . . . . .	5
2.2	Surface Plasmon Resonance . . . . .	8
2.2.1	The Evanescent Wave . . . . .	8
2.2.2	Dispersion Equations and Resonance . . . . .	11
2.3	Localized Surface Plasmon Resonance . . . . .	13
2.4	Nanoplasmonics . . . . .	14
2.4.1	Light Scattering and Absorption . . . . .	15
2.4.2	Spectral Shift in Plasmon Spectroscopy . . . . .	18
2.5	Factors Affecting the Sensitivity of a Localized Surface Plasmon Resonance Biosensor . . . . .	19
2.6	Microfluidics . . . . .	23
2.7	Acoustofluidics . . . . .	25
2.7.1	Surface Acoustic Waves . . . . .	27
2.7.2	Interdigital Transducer . . . . .	28
2.7.3	Microfluidic Mixing . . . . .	29
2.8	Summary . . . . .	30
<b>3</b>	<b>Micro- and Nanofabrication for Microfluidic Mixing Systems and Nanoplasmonic Sensors</b>	<b>31</b>
3.1	Fabrication Concepts . . . . .	31
3.1.1	Lithography . . . . .	32
3.1.2	Metal Patterning . . . . .	36
3.1.3	Surface Activation of PDMS . . . . .	37
3.2	Fabrication Recipes . . . . .	37
3.2.1	Fabrication Process of a Nanoplasmonic Sensor . . . . .	38

---

3.2.2	Fabrication Process of a Microchannel . . . . .	42
3.2.3	Fabrication Process of an Interdigital Transducer . . . . .	45
3.2.4	Assembly of the Microchannel and the Interdigital Transducers . . . . .	48
3.3	Summary . . . . .	48
<b>4</b>	<b>Experimental Campaign</b>	<b>49</b>
4.1	The NTNU Acoustofluidics Test Facility . . . . .	49
4.2	Objectives . . . . .	50
4.3	Test Campaign . . . . .	51
4.3.1	Microfluidic Mixing Test Procedure . . . . .	51
4.3.2	Nanoplasmonic Sensor Test Procedure . . . . .	53
4.3.3	Data Processing . . . . .	53
4.3.4	Experimental Uncertainties . . . . .	55
4.4	Summary . . . . .	58
<b>5</b>	<b>Results and Discussion</b>	<b>59</b>
5.1	Microfluidic Mixing Performance . . . . .	59
5.1.1	40 MHz IDT Performance . . . . .	61
5.1.2	80 MHz IDT Performance . . . . .	65
5.1.3	120 MHz IDT Performance . . . . .	67
5.1.4	Comparison of the Mixing Performance for the IDT Designs . . . . .	68
5.2	Nanoplasmonic Sensor Performance . . . . .	72
5.2.1	Effect of the Polynomial Order on the Sensitivity Performance . . . . .	72
5.2.2	Relation Between Wavelength Peak and Refractive Index . . . . .	75
5.2.3	Square Nanohole Array . . . . .	75
5.2.4	Hexagonal Nanohole Array . . . . .	77



---

5.2.5	Comparison of Square and Hexagonal Nanohole Array . . . . .	77
5.2.6	Relation Between Gold Layer Thickness and Sensor Sensitivity . . . . .	79
5.2.7	Obtained Sensitivity Compared to Values From the Literature . . . . .	81
<b>6</b>	<b>Conclusion and Further Work</b>	<b>83</b>
6.1	Conclusion . . . . .	83
6.2	Further Work . . . . .	85
	<b>Bibliography</b>	<b>87</b>
<b>A</b>	<b>Fabrication Recipe For a Nanoplasmonic Sensor</b>	<b>107</b>
<b>B</b>	<b>Fabrication Recipe For a Microfluidic Channel</b>	<b>109</b>
<b>C</b>	<b>Fabrication Recipe For an Interdigital Transducer</b>	<b>111</b>
<b>D</b>	<b>Fabrication Materials, Chemicals, and Instruments</b>	<b>113</b>
D.1	Substrates . . . . .	113
D.2	Chemicals . . . . .	113
D.3	Instruments . . . . .	115
<b>E</b>	<b>Calibration Equipment</b>	<b>119</b>
E.1	Additional Equipment for Microfluidic Mixing Experiments . . . . .	119
E.2	Additional Equipment for Nanoplasmonic Experiments . . . . .	120
<b>F</b>	<b>Mixing Performance</b>	<b>121</b>

# List of Tables

2.1	Sensitivity and wavelength peak for different nanohole arrays found in the literature. . . . .	22
4.1	Test matrix for the microfluidic mixing experiments. . . . .	52
4.2	The refractive index value for deionized water and different glycerol concentrations utilized in the conducted nanoplasmonic sensor experiments. Refractive index values are obtained from Hoyt. . . . .	53
4.3	Distance between the microchannel and the interdigital transducers for the different IDT designs. . . . .	58
5.1	Effect of the polynomial curve fitting order on the sensitivity and resonance wavelength peak for a hexagonal nanohole array with nanohole diameters of 400 nm, 250 nm gold layer thickness, and 1000 nm periodicity.	73
5.2	Dimensions and experimental results for the different nanoplasmonic sensors. . . . .	75
5.3	Difference in the resonant wavelength peak value for sensors with square and hexagonal nanohole arrays, a constant nanohole diameter of 400 nm, 250 nm gold layer thickness, and periodicities ranging from 700 to 1100 nm.	79
5.4	Difference in the resonant wavelength peak value for sensors with 200 and 250 nm gold layer thicknesses, a constant nanohole diameter of 400 nm, periodicities ranging from 700 to 1100 nm, and square nanohole arrays. .	80

---

5.5	Comparison of the maximum obtained sensitivity and wavelength peak to values found in the literature. . . . .	81
F.1	Numerical values of the mixing efficiency for IDT-1 of the 40 MHz IDT design. . . . .	121
F.2	Numerical values of the mixing efficiency for IDT-2 of the 40 MHz IDT design. . . . .	121
F.3	Numerical values of the mixing efficiency for the dual IDT of the 40 MHz IDT design. . . . .	122
F.4	Numerical values of the mixing efficiency for IDT-1 of the 80 MHz IDT design. . . . .	122
F.5	Numerical values of the mixing efficiency for IDT-2 of the 80 MHz IDT design. . . . .	122
F.6	Numerical values of the mixing efficiency for the dual IDT of the 80 MHz IDT design. . . . .	122
F.7	Numerical values of the mixing efficiency for IDT-2 of the 120 MHz IDT design. . . . .	123

# List of Figures

2.1	Visualization of exosome biogenesis. Exosomes contain protein markers and nucleic acids, which play vital roles in intercellular communication. . .	6
2.2	A timeline highlighting important observations of exosomes over the last 40 years. . . . .	7
2.3	A historical timeline of surface plasmon resonance presenting relevant innovations and observations. . . . .	9
2.4	Representation of the behavior of a two-dimensional (2D) plane wave when the resonance condition is (a) not fulfilled and (b) fulfilled. An evanescent wave occurs and propagates along the x-axis instead of reflecting at angle $\beta$ when the resonance condition is satisfied. . . . .	10
2.5	The localized surface plasmon resonance generates plasmon oscillations through the interaction between the incident light and the metallic nanostructures. . . . .	13
2.6	Illustration of the enhanced electromagnetic field around a metallic nanoparticle. . . . .	15
2.7	Visualization of attenuation of light in the propagation direction (z-direction). . . . .	16
2.8	A visual representation of scattering of an electromagnetic wave by a small dielectric particle. . . . .	16
2.9	Representation of lattice absorption of an electromagnetic wave, where the energy from the wave is converted into lattice vibrational energy. . . . .	17

---

2.10	Shift in the LSPR peak from an initial state (pink curve) to higher wavelengths when the refractive index changes at the metal interface (red curve).	19
2.11	Illustration of the absorption and scattering cross-sections and their magnitude based on nanoparticle size. Images modified from Li et al. . . . .	21
2.12	Ultraviolet-visible (UV-VIS) extinction spectra for silver PPA on mica substrate obtained by Haes et al. . . . .	21
2.13	Comparison of microchannel sizes utilized in the literature and this work.	25
2.14	A historical timeline of surface acoustic waves and interdigital transducers featuring important findings and inventions. . . . .	26
2.15	Schematic representation of the energy transfer from the generated surface acoustic waves by interdigital transducers to the fluid on a piezoelectric substrate. . . . .	28
2.16	Visualization of IDT parameters. . . . .	29
3.1	Fabrication techniques for micro- and nanoscale devices. . . . .	32
3.2	A standard photolithography process. . . . .	33
3.3	The effect on the photolithography result by using a negative or positive photoresist. . . . .	34
3.4	The effect on the pattern by reducing the pitch and increasing the beam diameter. . . . .	36
3.5	Schematic representation of the difference between an overcut and undercut resist profile for metal patterning. . . . .	37
3.6	Difference between square and hexagonal nanohole array. Images extracted from Saldaña. . . . .	38
3.7	Fabrication process flow for the nanoplasmonic sensor using electron beam lithography for transferring the desired pattern. . . . .	41
3.8	Fabrication process flow for the microchannel created by photolithography using a maskless aligner (MLA-150) and soft lithography. . . . .	44
3.9	Fabrication process flow for an interdigital transducer by utilizing a maskless aligner (MLA-150) and a mask aligner (MA-6). . . . .	47

---

3.10	The microfluidic device bonded to the platform enabling the energy transfer from the SAW generator to the IDTs by gold wires with a diameter of 25 $\mu\text{m}$ . . . . .	48
4.1	NTNU acoustofluidics test facility displaying relevant components. . . . .	50
4.2	Microfluidic mixing setup showing the two inlets and the one outlet of the microchannel, the two interdigital transducers, and the SAW platform connected to the platform area of the microscope. . . . .	52
4.3	Experimental setup of the nanoplasmonic sensor displaying the microscope, objective, and a sample with 10 nanoplasmonic sensors. . . . .	54
4.4	Bubble occurrence inside the microchannel. . . . .	57
5.1	The Y-shaped microchannel inlet showing a 50/50 fluid flow with DI water and a mixture of DI water and 0.25% sulforhodamine B under white and green light. . . . .	60
5.2	Part of the microchannel for the non-mixed state under white and green light. . . . .	60
5.3	Visualization of the 40 MHz, 80 MHz, and 120 MHz IDT designs and the microchannel without any power inputs under white light. . . . .	61
5.4	Comparison of the mixing efficiencies for IDT-1, IDT-2, and dual IDT of the 40 MHz, 80 MHz, and 120 MHz IDT designs with no power input (0 mW). . . . .	62
5.5	Mixing efficiency for IDT-1 of the 40 MHz IDT design at fixed flow rates and power applications. . . . .	62
5.6	Mixing efficiency for IDT-2 of the 40 MHz IDT design at fixed flow rates and power applications. . . . .	63
5.7	Mixing efficiency for the dual IDT of the 40 MHz IDT design at fixed flow rates and power applications. . . . .	64
5.8	Comparison of the mixing efficiencies for IDT-1, IDT-2, and dual IDT of the 40 MHz IDT design at a fixed flow rate of 1500 $\mu\text{L}/\text{h}$ and fixed power of 1500 mW. . . . .	64
5.9	Mixing efficiency for IDT-1 of the 80 MHz IDT design at fixed flow rates and power applications. . . . .	65
5.10	Mixing efficiency for IDT-2 of the 80 MHz IDT design at fixed flow rates and power applications. . . . .	66

---

---

5.11	Mixing efficiency for the dual IDT of the 80 MHz IDT design at fixed flow rates and power applications. . . . .	66
5.12	Comparison of the mixing efficiencies for IDT-1, IDT-2, and dual IDT of the 80 MHz IDT design at a fixed flow rate of $1500 \mu\text{L}/\text{h}$ and fixed power of 1500 mW. . . . .	67
5.13	Mixing efficiency for IDT-2 of the 120 MHz IDT design at fixed flow rates and power applications. . . . .	68
5.14	Comparison of the mixing efficiencies for IDT-2 of the 40 MHz, 80 MHz, and 120 MHz IDT designs at a fixed flow rate of $1500 \mu\text{L}/\text{h}$ and fixed power of 1500 mW. . . . .	69
5.15	Comparison of the mixing efficiencies for IDT-1 and IDT-2 of the 40 MHz and 80 MHz IDT designs at a fixed flow rate of $2500 \mu\text{L}/\text{h}$ and fixed power of 2500 mW. . . . .	69
5.16	Comparison of the mixing efficiencies for the dual IDT for the 40 MHz and 80 MHz IDT designs at a fixed flow rate of $1500 \mu\text{L}/\text{h}$ and fixed power of 1500 mW. . . . .	70
5.17	Comparison of the mixing efficiencies for IDT-1, IDT-2, and dual IDT of the 40 MHz IDT design at a fixed flow rate of $2500 \mu\text{L}/\text{h}$ and fixed power of 2000 mW for the single IDTs and 1000 mW for the dual IDT. . . . .	71
5.18	Comparison of the mixing efficiencies for IDT-1, IDT-2, and dual IDT of the 80 MHz IDT design at a fixed flow rate of $500 \mu\text{L}/\text{h}$ and fixed power of 2000 mW for the single IDTs and 1000 mW for the dual IDT. . . . .	71
5.19	Comparison of the mixing efficiencies for IDT-1, IDT-2, and dual IDT of the 40 MHz and 80 MHz IDT designs at a fixed flow rate of $2500 \mu\text{L}/\text{h}$ and fixed power of 2000 mW for the single IDTs and 1000 mW for the dual IDT. . . . .	72
5.20	Representation of the equivalence between the obtained experimental spectra for a hexagonal nanohole array with a nanohole diameter of 400 nm, 250 nm gold layer thickness, and 1000 nm periodicity and the polynomial curve fitting for polynomial orders of 15, 25, and 50. The green curves indicate the fitted curves. . . . .	73
5.21	Refractive index plotted against the resonance wavelength peak from the polynomial curve fitting for polynomial orders of 15, 25, and 50 for a sensor with a hexagonal nanohole array, a nanohole diameter of 400 nm, 250 nm gold layer thickness, and 1000 nm periodicity. . . . .	74

---

---

5.22	Relation between the wavelength peak and the refractive index for square and hexagonal nanohole arrays with constant nanohole diameters of 400 nm, constant gold layer thicknesses of 250 nm, and periodicities ranging from 700 to 1100 nm. . . . .	76
5.23	Relation between the resonance wavelength peak shifts and the refractive indices for square nanohole arrays with constant nanohole diameters of 400 nm, constant gold layer thickness of 250 nm, and periodicities ranging from 700 to 1100 nm. The linear regression function and corresponding $R^2$ values are indicated. . . . .	76
5.24	Relation between the resonance wavelength peak shifts and the refractive indices for hexagonal nanohole arrays with constant nanohole diameters of 400 nm, constant gold layer thickness of 250 nm, and periodicities ranging from 700 to 1100 nm. The linear regression function and corresponding $R^2$ values are indicated. . . . .	77
5.25	Comparison of the resonance wavelength peak shift against the refractive indices for the two best sensor designs with square and hexagonal nanohole arrays with constant nanohole diameters of 400 nm, constant gold layer thicknesses of 250 nm, and periodicities ranging from 700 to 1100 nm. The linear regression function and corresponding $R^2$ values are indicated. . . . .	78
5.26	Comparison of the obtained sensitivity plotted against the pitch for square and hexagonal nanohole arrays. The sensor parameters are periodicities ranging between 700 and 1100 nm, a constant gold layer thickness of 250 nm, and a nanohole diameter of 400 nm. . . . .	78
5.27	Relation between the gold layer thickness and refractive index sensitivity for square nanohole arrays with constant nanohole diameter of 400 nm and periodicities between 700 and 1100 nm. . . . .	80
5.28	Experimental spectra of nanoplasmonic sensors with square nanohole arrays, a constant nanohole diameter of 400 nm, periodicities ranging from 700 to 1100 nm, and different gold layer thicknesses of 200 and 250 nm. A higher gold layer thickness results in a sharper peak. . . . .	81
5.29	Maximum obtained sensitivity and resonance wavelength peak position compared to results found in the literature. . . . .	82
F.1	Comparison of the mixing efficiencies for IDT-1, IDT-2, and dual IDT for the 40 MHz IDT design at a fixed flow rate of $500 \mu\text{L}/\text{h}$ and fixed power of 500 mW. . . . .	123

---



---

F.2	Comparison of the mixing efficiencies for IDT-1, IDT-2, and dual IDT for the 40 MHz IDT design at a fixed flow rate of 2500 $\mu\text{L}/\text{h}$ and fixed power of 2500 mW. . . . .	123
F.3	Comparison of the mixing efficiencies for IDT-1 and IDT-2 for the 40 MHz IDT design at fixed power of 1000 and 2000 mW. . . . .	124
F.4	Comparison of the mixing efficiencies for IDT-1 and IDT-2 for the 40 MHz IDT design at a fixed flow rate of 1000 and 2000 $\mu\text{L}/\text{h}$ . . . . .	124
F.5	Comparison of the mixing efficiencies for IDT-1, IDT-2, and dual IDT of the 80 MHz IDT design at a fixed flow rate of 500 $\mu\text{L}/\text{h}$ and fixed power of 500 mW. . . . .	125
F.6	Comparison of the mixing efficiencies for IDT-1, IDT-2, and dual IDT of the 80 MHz IDT design at a fixed flow rate of 1000 $\mu\text{L}/\text{h}$ and fixed power of 1000 mW. . . . .	125
F.7	Comparison of the mixing efficiencies for IDT-1, IDT-2, and dual IDT of the 80 MHz IDT design at a fixed flow rate of 2000 $\mu\text{L}/\text{h}$ and IDT-1 and IDT-2 at fixed power of 2000 mW. . . . .	126
F.8	Comparison of the mixing efficiencies for IDT-1, IDT-2, and dual IDT of the 80 MHz IDT design at a fixed flow rate of 2500 $\mu\text{L}/\text{h}$ and IDT-1 and IDT-2 at fixed power of 2500 mW. . . . .	126
F.9	Comparison of the mixing efficiencies for IDT-2 of the 40 MHz, 80 MHz, and 120 MHz IDT designs at a fixed flow rate of 500 $\mu\text{L}/\text{h}$ and fixed power of 500 mW. . . . .	127
F.10	Comparison of the mixing efficiencies for IDT-2 of the 40 MHz, 80 MHz, and 120 MHz IDT designs at a fixed flow rate of 1000 $\mu\text{L}/\text{h}$ and fixed power of 1000 mW. . . . .	127
F.11	Comparison of the mixing efficiencies for IDT-2 of the 40 MHz, 80 MHz, and 120 MHz IDT designs at fixed power of 2000 mW. . . . .	127
F.12	Comparison of the mixing efficiencies for IDT-1 and IDT-2 of the 40 MHz and 80 MHz IDT designs at a fixed flow rate of 500 $\mu\text{L}/\text{h}$ and fixed power of 500 mW. . . . .	128
F.13	Comparison of the mixing efficiencies for single IDT of the 40 MHz and 80 MHz IDT designs at a fixed flow rate of 1000 $\mu\text{L}/\text{h}$ and fixed power of 1000 mW. . . . .	128

---

---

F.14	Comparison of the mixing efficiencies for single IDT of the 40 MHz and 80 MHz IDT designs at a fixed flow rate of 1500 $\mu\text{L}/\text{h}$ and fixed power of 1500 mW. . . . .	129
F.15	Comparison of the mixing efficiencies for single IDT of the 40 MHz and 80 MHz IDT designs at a fixed flow rate of 2000 $\mu\text{L}/\text{h}$ and fixed power of 2000 mW. . . . .	129
F.16	Comparison of the mixing efficiencies for the dual IDT of the 40 MHz and 80 MHz IDT designs at a fixed flow rate of 500 $\mu\text{L}/\text{h}$ and fixed power of 500 mW. . . . .	130
F.17	Comparison of the mixing efficiencies for the dual IDT of the 40 MHz and 80 MHz IDT designs at a fixed flow rate of 2500 $\mu\text{L}/\text{h}$ . . . . .	130
F.18	Comparison of the mixing efficiencies for the dual IDT of the 40 MHz and 80 MHz IDT designs at fixed power of 1000 mW. . . . .	130
F.19	Comparison of the mixing efficiencies for IDT-1, IDT-2, and dual IDT of the 40 MHz IDT design at a fixed flow rate of 500 $\mu\text{L}/\text{h}$ and fixed power of 1000 mW for the single IDTs and 500 mW for the dual IDT. . . . .	131
F.20	Comparison of the mixing efficiencies for IDT-1, IDT-2, and dual IDT of the 40 MHz IDT design at a fixed flow rate of 1500 $\mu\text{L}/\text{h}$ for equal energy inputs into the system for the single and dual IDTs. . . . .	131
F.21	Comparison of the mixing efficiencies for IDT-1, IDT-2, and dual IDT of the 80 MHz IDT design at a fixed flow rate of 1000 $\mu\text{L}/\text{h}$ and fixed power of 1000 mW for the single IDTs and 500 mW for the dual IDT. . . . .	132
F.22	Comparison of the mixing efficiencies for IDT-1, IDT-2, and dual IDT of the 80 MHz IDT design at fixed flow rates of 1000 $\mu\text{L}/\text{h}$ and 2000 $\mu\text{L}/\text{h}$ for equal energy inputs into the system for the single and dual IDTs. . . . .	132
F.23	Comparison of the mixing efficiencies for IDT-1, IDT-2, and dual IDT of the 80 MHz IDT design at a fixed flow rate of 2500 $\mu\text{L}/\text{h}$ for equal energy inputs into the system for the single and dual IDTs. . . . .	133
F.24	Comparison of the mixing efficiencies for IDT-1, IDT2, and dual IDT of the 40 MHz and 80 MHz IDT designs at a fixed flow rate of 500 $\mu\text{L}/\text{h}$ and fixed power of 1000 mW for the single IDTs and 500 mW for the dual IDT. . . . .	133
F.25	Comparison of the mixing efficiencies for IDT-1, IDT-2, and dual IDT of the 40 MHz and 80 MHz designs at a fixed flow rate of 1500 $\mu\text{L}/\text{h}$ for equal energy inputs into the system for the single and dual IDTs. . . . .	134

---

# Nomenclature

## Symbols and Units

<b>Symbol</b>	<b>Description</b>	<b>Unit</b>
$A$	Cross-sectional area	$m^2$
$a$	Aperture	$m$
$C_{SAW}$	Substrate acoustic velocity	$m/s$
$c$	Propagation velocity in vacuum	$3 \cdot 10^8 m/s$
$D$	Diffusion constant	[-]
$D_h$	Hydraulic diameter	$m$
$d$	Diameter	$m$
$d_{al}$	Effective adsorbate layer thickness	$m$
$d_f$	Finger spacing	$m$
<b>E</b>	Electric field	$(kg \cdot m)/s^3$
$E_{amp}$	Amplitude of the electric field	$(kg \cdot m)/s^3$
$E_{ew}$	Evanescent wave	$(kg \cdot m)/s^3$
$E_{inc}$	Incident electric field	$(kg \cdot m)/s^3$
$E_r$	Reflected electric field	$(kg \cdot m)/s^3$
$e$	Electron charge	$C$
$f$	Frequency	$Hz$
$h$	Height	$m$
$I_i$	Average intensity of each line along the width of the region of interest	$a.u.$
$\bar{I}_i$	Normalized average intensity value of line i	$a.u.$
$I_{max}$	Maximum intensity value of the unmixed state	$a.u.$
$I_{min}$	Minimum intensity value of the unmixed state	$a.u.$
$\bar{I}_\infty$	Normalized intensity value of each line in the complete mixed state	$a.u.$
$j$	Imaginary number	[-]

continued on next page

---

## Symbols and Units

<b>Symbol</b>	<b>Description</b>	<b>Unit</b>
<b><math>\mathbf{k}</math></b>	Wave vector	$rad/m$
$k_x$	x-component of wave vector $\mathbf{k}$	$rad/m$
$k_y$	y-component of wave vector $\mathbf{k}$	$rad/m$
$k_z$	z-component of wave vector $\mathbf{k}$	$rad/m$
$L$	Characteristic length scale	$m$
$L_{SAW}$	Attenuation length of the surface acoustic wave into a liquid	$m$
$l$	Electromagnetic field decay length	$m$
$m$	Bulk refractive index response	[-]
$m_e$	Electron mass	$9.109 \cdot 10^{-31} kg$
$N$	Number of lines along the region of interest (ROI)	[-]
$n$	Refractive index	[-]
$n_e$	Free electron density	$m^{-3}$
$P$	Wetted perimeter of cross-section	$m$
$Pe$	Péclet number	[-]
$R$	Radius	$m$
$Re$	Reynolds number	[-]
$R_p$	Reflectance	[-]
$\mathbf{r}$	Position vector	$m$
$r_p$	Complex reflection coefficient	[-]
$S$	Sensitivity	$nm/RIU$
$T$	Period	$m$
$t$	Time	$s$
$U$	Velocity	$m/s$
$v_{lw}$	Velocity of the longitudinal wave in the fluid	$m/s$
$v_{SAW}$	Surface acoustic wave velocity in the substrate	$m/s$
$w$	Width	$m$
$w_f$	Finger width	$m$

---

### Greek Symbols and Units

<b>Symbol</b>	<b>Description</b>	<b>Unit</b>
$\alpha$	Incident angle	$^{\circ}$
$\alpha_L$	Attenuation coefficient per unit length of the Rayleigh wave	$1/L$
$\beta$	Reflected angle	$^{\circ}$
$\Delta n$	Change in refractive index	[-]
$\Delta\lambda_{max}$	Shift in maximum wavelength	$m$
$\epsilon$	Dielectric constant	[-]
$\epsilon_{abs}$	Absolute permittivity	$8.8542 \cdot 10^{-12} F/m$
$\epsilon_{rel}$	Relative permittivity	$F/m$
$\eta$	Mixing efficiency	[-]
$\theta$	Rayleigh angle. Angle given by the ratio of the sound velocities in two mediums	$^{\circ}$
$\lambda$	Wavelength	$m$
$\lambda_{max}$	Maximum wavelength	$m$
$\lambda_{SAW}$	Surface acoustic wave wavelength	$m$
$\mu$	Dynamic viscosity	$kg/(s \cdot m)$
$\mu_{abs}$	Absolute permeability	$4\pi \cdot 10^{-7} H/m$
$\nu$	Kinematic viscosity	$m^2/s$
$\nu_m$	Speed of light in a medium	$m/s$
$\rho$	Density	$kg/m^3$
$\rho_l$	Density of liquid	$kg/m^3$
$\rho_s$	Density of substrate material	$kg/m^3$
$\varphi$	Phase change	$^{\circ}$
$\omega$	Angular frequency	$rad/s$
$\omega_{pf}$	Plasma frequency	$rad/s$
$\Omega$	Electrical resistance	$(kg \cdot m^2)/(s^3 \cdot A^2)$

---

## Subscripts

<b>Index</b>	<b>Description</b>
1	Medium 1
2	Medium 2
<i>abs</i>	Absolute
<i>al</i>	Adsorbate layer
<i>amp</i>	Amplitude
<i>e</i>	Electron
<i>ew</i>	Evanescent wave
<i>f</i>	Finger
<i>h</i>	Hydraulic
<i>i</i>	Line
<i>inc</i>	Incident
<i>L</i>	Length scale
<i>l</i>	Liquid
<i>lw</i>	Longitudinal wave
<i>m</i>	Medium
<i>max</i>	Maximum
<i>min</i>	Minimum
<i>p</i>	Plane-polarized light
<i>pf</i>	Plasmon frequency
<i>r</i>	Reflected
<i>rel</i>	Relative
<i>SAW</i>	Surface acoustic wave
<i>s</i>	Substrate
<i>x</i>	x-component
<i>y</i>	y-component
<i>z</i>	z-component
$\infty$	Infinity

---

## Abbreviations

<b>Abbreviation</b>	<b>Description</b>
1D	One-Dimensional
2D	Two-Dimensional
3D	Three-Dimensional
3D-dSAW	Three Dimensional dual Surface Acoustic Wave
AFM	Atomic Force Microscope
BSE	Back-Scattered Electron
BWA	Biological Warfare Agent
DANS	Deterministic Aperiodic Nanostructures
DI	Deionized
DIC	Differential Interference Contrast
DNA	Deoxyribonucleic Acid
dsDNA	Double-Stranded Deoxyribonucleic Acid
EBL	Electron Beam Lithography
EM	Electromagnetic
FOM	Figure Of Merit
F-IDT	Focused Interdigital Transducer
HMDS	Hexamethyldisilazane
IDT	Interdigital Transducer
IPA	Isopropanol
IR	Infrared
LOC	Lab-On-Chip
LSPR	Localized Surface Plasmon Resonance
MA	Masked Aligner
MIBK	Methyl Isobutyl Ketone
miRNA	Micro Ribonucleic Acid
MLA	Maskless Aligner
mRNA	Messenger Ribonucleic Acid
mtDNA	Mitochondrial Deoxyribonucleic Acid
NIR	Near-Infrared
NSL	Nanosphere Lithography
NTNU	Norwegian University of Science and Technology

continued on next page

---

## Abbreviations

<b>Abbreviation</b>	<b>Description</b>
PDMS	Poly(dimethylsiloxane)
PEB	Post-Exposure Bake
PMMA	Poly(methylmethacrylate)
POC	Point-Of-Care
PPA	Periodic Particle Array
RI	Refractive Index
RIU	Refractive Index Unit
RNA	Ribonucleic Acid
ROI	Region Of Interest
SAW	Surface Acoustic Wave
SE	Second Electron
SEM	Scanning Electron Microscope
SP	Surface Plasmon
SPR	Surface Plasmon Resonance
ssDNA	Single-Stranded Deoxyribonucleic Acid
SSAW	Standing Surface Acoustic Wave
TMAH	Tetramethylammonium Hydroxide
TSAW	Traveling Surface Acoustic Wave
UV	Ultraviolet light
VIS	Visible light
WHO	World Health Organization

## Technical terms

<b>Technical term</b>	<b>Description</b>
Acoustofluidics	The fusion of acoustics and fluid mechanics.
Adsorbate	Adsorbed substance on a surface.
Analyte	A substance or sample that is being analyzed.
Biomarker	Substance that indicates a certain biological process or condition.

---

continued on next page



---

## Technical terms

<b>Technical term</b>	<b>Description</b>
Bulk effect	An effect that arises within the entire bulk or quantity in a semiconductor material instead of within a junction or localized region.
Dielectric	Very poor conductor of electric current or insulating material (a non-conducting substance or an insulator).
Diffraction limit	Half the width of the wavelength of light used to see the specimen of interest.
Electron beam lithography	Method to create mask patterns directly on a substrate (chip) by using electron beams.
Electron beam evaporator	One mode for deposition of metal layers on a substrate.
Electron-electron scattering (Møller-scattering)	Scattering of electrons by electrons.
Exosome	Small membrane-bound compounds with a size range from 30 to 120 nm.
Hydrophilic	Strong affinity for water.
Hydrophobic	Absence of affinity for water.
Inverse piezoelectric	Generation of mechanical strain from the application of an electric field.
In vitro	Study of a biological process outside its natural environment or setting.
In vivo	Study of a biological process in its natural environment or setting.
Lipid	A variety of organic compounds that mostly do not interact with water (e.g. fat, hormones, oil).
Lipid bilayer	Impermeable barrier to protect essential water-soluble substances in the cell. Also provides the basis for separating different biological membranes.
Lithography	General denotation given to processes producing a pattern on a substrate.
Metabolite	A substance produced by metabolism.

continued on next page

---

## Technical terms

Technical term	Description
Microfluidics	The science and technology of systems that process or manipulate small fluid quantities using channels with dimensions of tens to hundreds of micrometers.
Nanosphere lithography	Fabrication technique using a mask of self-assembled close-packed arrays of nanospheres for pattern transfer onto a substrate.
Nucleic acid	Any complex organic acid composed of nucleotide chains.
Permeability	A measure of the material response when a magnetic field is applied.
Permittivity	Measurement of the electric polarizability of a dielectric.
Petri dish	A small, round, clear dish with a cover.
Photolithography	A process producing patterns on a substrate by exposing a light-sensitive polymer with ultraviolet light.
Piezoelectric	The generation of electric charge upon the application of mechanical stress in certain materials.
Plasmonics	A discipline for the interaction between free electrons and an electromagnetic wave at the interface between a metal and a dielectric material under certain conditions (i.e. resonance condition).
Polarizability	A measure of how easy an electron cloud can be distorted from its original shape by an external electric field.
Polarization	Property of certain electromagnetic radiations that are restricted to specific directions of vibration.
P-polarized light	Plane polarized light. The electric field of the light is along the plane of incidence.
Refraction law	The ratio of the speed of sound in a fluid and a solid.
Refractive index	The ratio between the propagation speed in vacuum and the speed of light in a medium.

continued on next page

---

## Technical terms

Technical term	Description
Resonance	The tendency of a system to vibrate due to an increase in the amplitude of oscillation when subjected to an external periodic force at its natural frequency (or at certain frequencies of excitation).
Snell's law	The relationship between the direction of light when crossing the boundary or interface between two contacting substances and their refractive indices.
Soft lithography	A patterning technique where an elastomeric stamp is utilized to transfer patterns through molding, printing, or embossing.
Spectrometry	A method for measuring the interactions between light and matter as well as reactions and measurement of the wavelength and intensity of radiation.
Spectroscopy	A technique where a spectrometer is utilized to produce and investigate spectra. These spectra can be determined through frequency or intensity changes of the radiative energy involved in the interaction between light and matter.

# Introduction

## 1.1 Background

For centuries cancer has been one of the leading causes of death globally. In 2020, the World Health Organization (WHO) reported 10.0 million cancer deaths worldwide. They have registered 19.3 million new cases of cancer, and expect the number to increase by 47%, resulting in 28.4 million new cases in 2040 [1]. In Norway, 11,049 cancer deaths were reported in 2018, representing 27% of all deaths that year [2, 3].

The advance in research has allowed an increase in the survival rate and cancer treatments. However, the necessity for early detection of cancer biomarkers through rapid, informative, and accurate identification and non-invasive physical interventions is essential for a good degree of medical success. As we are moving towards more advanced detection techniques, the separation and recognition of the specific cancer biomarkers gain high relevance in areas related to early detection, medical diagnostics, and prognosis.

In recent years, exosomes have been identified as potential cancer biomarkers through their unique content of proteins, deoxyribonucleic acid (DNA), and ribonucleic acid (RNA). A great quantity of exosomes is secreted from cells and they are found in abundance in body fluids. In many biological processes, exosomes play a major role in medical diagnostics as a result of their cell-to-cell communication and multifunctional attributes.

The idea to detect cancer biomarkers *in vivo* has provided the development and growth of biological sensors. Biosensors have shown great versatility and potential for protein and nucleic acid identification as well as for the detection of more complex entities such as exosomes. By using an optical biosensor, the detection of biointerfacial reactions and monitoring of the biomolecular kinetic binding response can be measured as a result of

the non-physical connection between the biosensing area and the light source. Incorporating metallic nanostructures at the sensor surface can possibly enhance the binding signals. This provides nanoplasmonic properties and enables a resonance peak shift at the maximum extinction wavelength for each modification when introducing the substances of interest. Thus, these shifts can be utilized for exosome detection.

Despite the great potential of using exosomes as cancer biomarkers and promising biosensor technologies, there are still related challenges. The exosomes need to be isolated from macromolecules such as proteins and other compounds, where the most used technique has been ultracentrifugation. Ultracentrifugation is time-consuming, expensive, and recovers a small number of exosome quantities. Therefore, this limits the use of exosomes for nanomedicines and detection standard applications as a consequence of their requirement for a large amount of exosomes in order to execute *in vivo* testing. However, the recent improvements in microfluidic technology have enabled the manipulation of cells and sub-micron biological entities with high yields from complex fluids including blood. Hence, this technology can be used for improving the exosome interaction with the nanoplasmonic biosensor surface for higher detection performance. By incorporating acoustofluidics, *in vivo* detection for early cancer diagnosis can be available in the near future.

## 1.2 Scope of Thesis

Exosomes are natural cell-derived extracellular compounds secreted by cells that play an essential role in cell-to-cell communication by carrying contents, including proteins, metabolites, RNAs (mRNA, miRNA, long non-coding RNA), DNAs (mtDNA, ssDNA, dsDNA), and lipids. The unprecedented and growing interest in the small-sized (30-120 nm) extracellular biostructures is owing to its role in intercellular communication and participation in the regulation of normal physiological processes, but also in the pathological processes of many diseases such as cancer. However, the difficulty in the clinical utilization of exosomes has been the lack of consistent and dependable methods for manipulation and characterization of exosomes. Recently, acoustofluidics, the fusion of acoustics and fluid mechanics, has provided a paradigm for achieving fast and effective fluid actuation and contact-free, non-invasive particle manipulation. By considering acoustofluidics with the promising detection approach of a localized surface plasmon resonance (LSPR) biosensor, a possible prototype for *in vivo* detection of exosomes can be developed.

The main tasks are:

1. Establish relevant acoustofluidic and biosensor fundamentals.
2. Test and document how the IDT design and power application affect the microfluidic mixing performance.
3. Perform spectrometry analysis of the nanoplasmonic biosensor for different geometrical features to determine the sensor sensitivity performance.

## 1.3 Limitations of Scope

*Scope 1:* Only relevant concepts, techniques, and phenomena have been investigated in order to give an understanding of the conducted tests in the experimental campaign.

*Scope 2:* Three IDT designs with frequencies of 40, 80, and 120 MHz have been tested and compared for single and dual IDT. The fluid flow rates and power applications have been restricted to values between 500 and 4000  $\mu\text{L}/\text{h}$  and 0 to 2500 mW, respectively.

*Scope 3:* The geometrical features have been limited to nanoholes with a constant nanohole diameter and variations in periodicity, gold layer thickness, and nanohole array. Deionized water and four glycerol mixtures obtaining specific refractive indices have been applied in the spectrometry analysis.

## 1.4 Information Retrieval

This master thesis aims to provide a solid foundation and enhanced understanding of the incorporation of surface acoustic waves for improving the detection of nanoplasmonic biosensors. The literature review aims to reveal existing knowledge on the area and assist in predictions and planning in accordance with the experimental campaign.

Focus has been directed towards finding relevant and reliable information throughout the literature review. Information retrieval from peer-reviewed journals, relevant books, conference presentations, and previous thesis' has been extracted from multiple databases. The primary databases used for information retrieval have been "Google Scholar" and "Oria". To obtain an unbiased and complete literature review, effort has been put into conducting a rigorous search pattern applying particular keywords, concepts, and respective synonyms.

Parts of the theory in the chapters regarding plasmonic fundamentals and concepts, in addition to certain experimental uncertainties, are based on the project thesis of the author [4].

## 1.5 Report Structure

The remainder of this master thesis has the following structure:

- Chapter 2 - Presentation of fundamental elements and concepts for nanoparticle detection including surface plasmon resonance, localized surface plasmon resonance, nanoplasmonics, microfluidics, and acoustofluidics.

- Chapter 3 - Introduction to micro- and nanofabrication methods utilized to fabricate the nanoplasmonic sensors and the microfluidic elements for experimental testing. Detailed descriptions of the fabrication processes for the nanoplasmonic sensors, the microchannels, and the interdigital transducers are presented.
- Chapter 4 - Presentation of the experimental test campaign, the NTNU acoustofluidics test facility, test procedure, data processing, and experimental uncertainties.
- Chapter 5 - Presentation, analysis, and discussion of the obtained results from the experimental test campaign.
- Chapter 6 - Concluding remarks and recommendations for further work.

# Fundamentals of Nanoparticle Detection and Manipulation

The following chapter introduces fundamental concepts for this master thesis. At first, elements concerning nanoparticle detection including exosome, surface plasmon resonance, localized surface plasmon resonance, nanoplasmonics, and factors affecting the sensor sensitivity will be explained. Further, microfluidics and acoustofluidics will be described owing to their possibility to enhance the sensor detection performance through nanoparticle manipulation.

## 2.1 Exosomes

Exosomes are small membrane-bound compounds secreted from cells and released in the extracellular space. The biomolecular nanostructures are in the size range of 30-120 nm in diameter [5, 6, 7, 8, 9, 10]. The exosomes contain nucleic acids and cell-type-specific protein cargo and transport the cargo between different locations within an organism. Moreover, they are unique to the cell of origin and possess a unique protein and lipid composition, which contributes to their identification with significant quantities in saliva, blood, and urine [5, 6, 11, 12]. The exosomes have also detection potential *in vitro* – by identifying full-length proteins generated using a translation system, and *in vivo* – by immune-stimulating effects. A visual representation of an exosome and its characteristics can be seen in Figure 2.1.



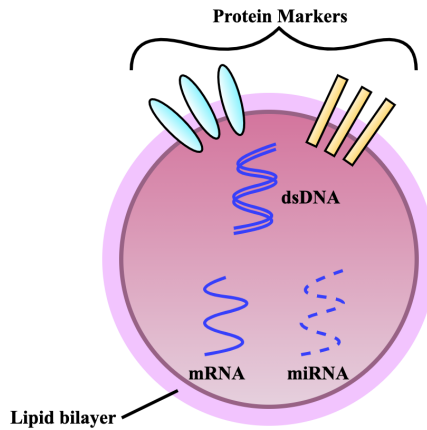


**Figure 2.1:** Visualization of exosome biogenesis. Exosomes contain protein markers and nucleic acids, which play vital roles in intercellular communication.

Exosomes were considered as redundant protein waste from the cells until 2007. At this time, Valadi et al. [13] presented a study that concluded the exosomes' RNA content. As a result, the exosomes became deliberated as specifically secreted compounds enabling intercellular communication [6], and the number of exosome studies increased significantly. Several studies have indicated advantages by using exosomes for early diagnosis of a variety of diseases owing to their valuable characteristics. This includes their specific protein and lipid composition, DNA and RNA content, and intercellular communication [6, 7, 9, 10, 14, 15, 16]. Other publications presented an increase in the exosome concentration released from cancer cells compared to healthy cells [6, 17, 18, 19, 20]. These findings have been used for the detection of multiple cancer tumors from exosomes, including ovarian, prostate, breast, and hematologic malignancies [10, 21, 22, 23, 24, 25]. Hence, the exosomes present in body fluids have the potential as sensitive, non-invasive biomarkers for therapeutics and diagnostics.

However, the isolation of exosomes from other extracellular compounds is a limitation. For *in vivo* testing, nanomedicines and detection applications require a large amount of exosomes. As of now, the method used for exosome separation is ultracentrifugation, which is time-consuming, expensive, and with a low exosome extraction percentage. Thus, other separation methods or detection applications with lower exosome concentration requirements are necessary to establish for further utilization of the promising exosome characteristics.

Figure 2.2 displays a timeline presenting important exosome observations the last 40 years.

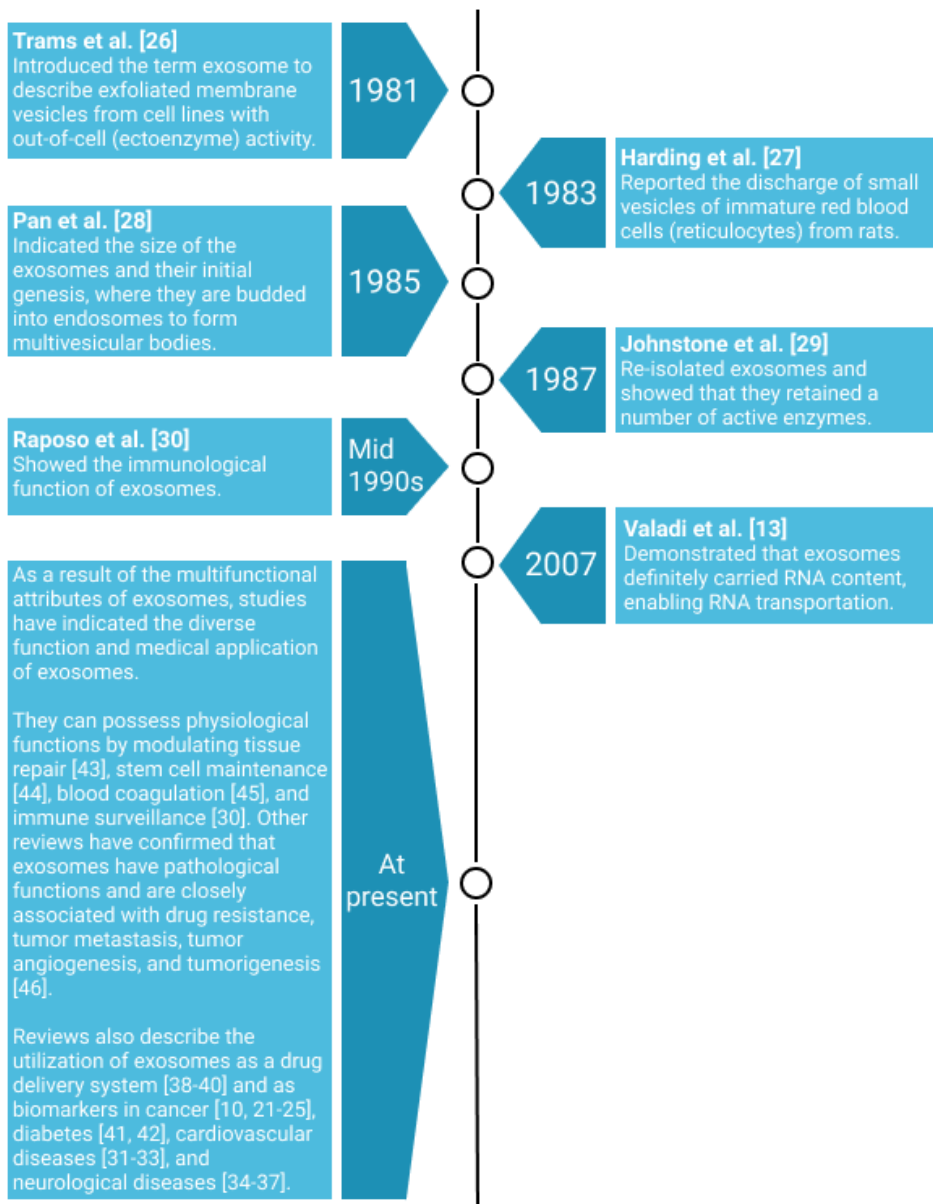


**Figure 2.2:** A timeline highlighting important observations of exosomes over the last 40 years.

## 2.2 Surface Plasmon Resonance

Surface plasmon resonance (SPR) refers to the collective oscillation of conduction band electrons (i.e. surface plasmons) at the interface between a metal and a dielectric upon the interaction with plane-polarized light [16]. This leads to the generation of a surface plasmon wave propagating in the  $x$ - and  $y$ -directions along with the metal-dielectric interface. They can propagate for distances on the order of tens to hundreds of microns, and decay evanescently in the  $z$ -direction with  $1/e$  decay lengths on the order of 200 nm [47].

Currently, SPR spectroscopy dominates the commercial instrumentation and can detect macromolecules in analytical fields including environmental monitoring, food safety, drug discovery, biological studies, clinical diagnosis, and health science research. The frequent use of the SPR technology is associated with its label-free, real-time monitoring, minimal sample treatment, good sensitivity and reproducibility, and the ability of miniaturization [48]. These qualities make the SPR biosensor suitable for point-of-care (POC) devices.

The evanescent wave, the dispersion relation, and resonance are central concepts to understand the surface plasmon resonance (SPR) phenomenon. The physical principles of SPR will be presented and described in the following sections.

### 2.2.1 The Evanescent Wave

A mathematical expression of an electromagnetic plane wave propagating in a medium with refractive index  $n$  by an electric field  $\mathbf{E}$  can be described as [50]:

$$\mathbf{E} = E_{amp} \cdot e^{(j\omega t - j\mathbf{k} \cdot \mathbf{r})} = E_{amp} \cdot e^{(j\omega t - jk_x x - jk_y y - jk_z z)} \quad (2.1)$$

where  $E_{amp}$  is the amplitude of the electric field,  $\omega$  is the angular frequency,  $\mathbf{k} = (k_x, k_y, k_z)$  is the wave vector,  $\mathbf{r} = (x, y, z)$  is the position vector,  $t$  is the time, and  $j = \sqrt{-1}$ . A complex component is a requirement for the wave to propagate.

The refractive index (RI) can be explained as the ratio between the propagation speed in vacuum,  $c$ , and the speed of light in the medium  $\nu_m$  [82], and is given as:

$$n = \frac{c}{\nu_m} = \frac{c}{\sqrt{\epsilon_{rel} \epsilon_{abs} \mu_{abs}}} = \sqrt{\epsilon_{rel}} \quad (2.2)$$

where  $\epsilon_{rel}$  is the relative permittivity, and  $\mu_{abs}$  and  $\epsilon_{abs}$  are the absolute permeability and permittivity, respectively.

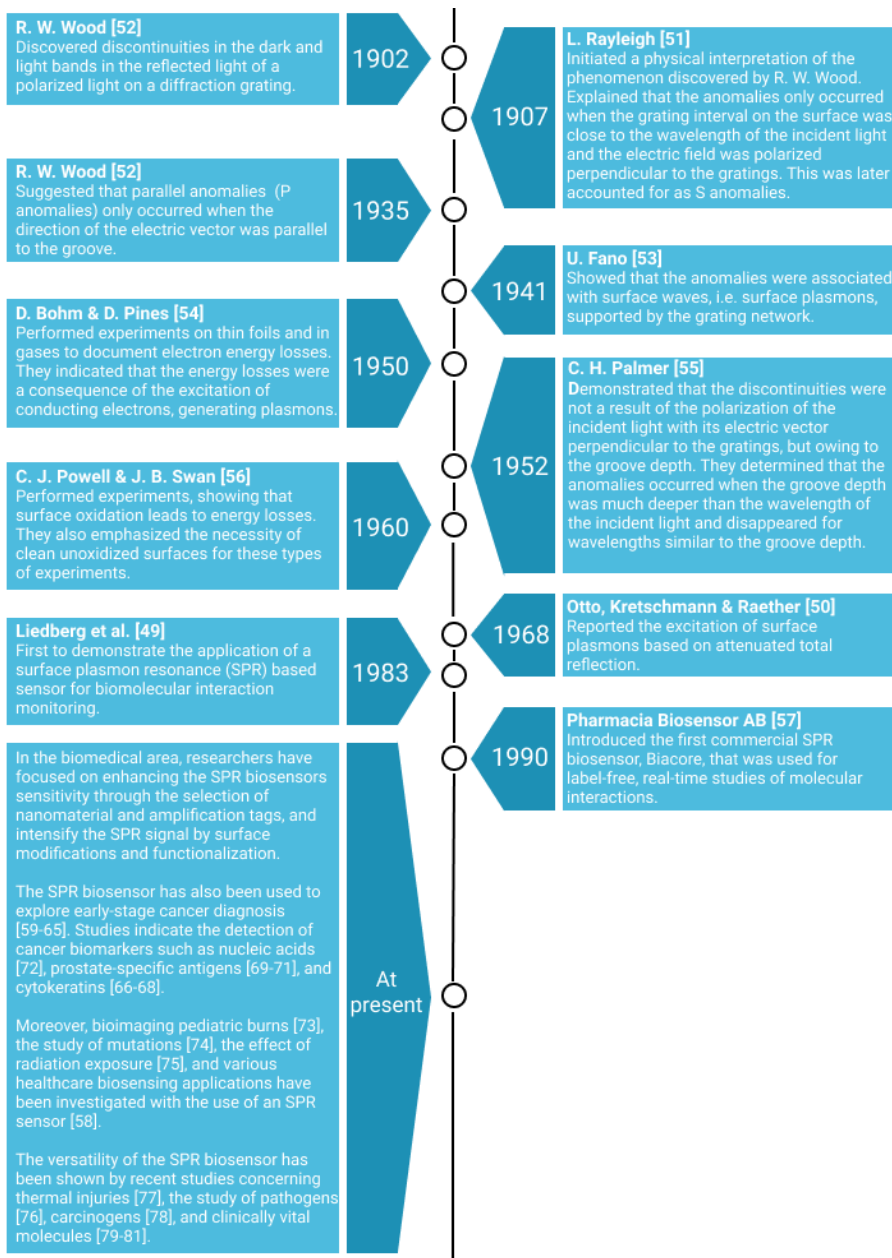


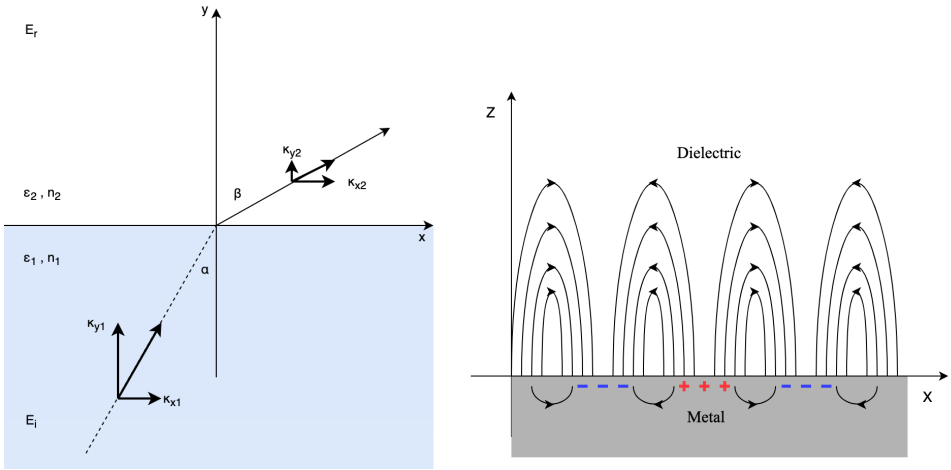
**Figure 2.3:** A historical timeline of surface plasmon resonance presenting relevant innovations and observations.

The direction of the wave vector  $\mathbf{k}$  is parallel to the wave propagation. Its magnitude is given as:

$$\mathbf{k} = \sqrt{k_x^2 + k_y^2 + k_z^2} = n \frac{2\pi}{\lambda} = n \frac{\omega}{c} \quad (2.3)$$

where  $\lambda$  is the wavelength,  $\omega$  and  $c$  have the same definitions as in Equation 2.1 and 2.2, and  $n$  is the refractive index of the medium. The RI can also be defined as the squared root of the dielectric constant of the material ( $n = \sqrt{\epsilon}$ ).

Figure 2.4a presents a visualization of a two-dimensional (2D) plane wave ( $k_z = 0$ ) propagating from medium 1 to medium 2 with refractive indices  $n_1$  and  $n_2$ , respectively. Using Snell's law, defined as the relationship between the direction of light when crossing the boundary or interface between two contacting substances and their refractive indices [83], the angles of incidence  $\alpha$  and refraction  $\beta$  are related to the refractive indices of the media. This gives:



(a) Illustration of an electric field incident at angle  $\alpha$  from medium  $\epsilon_1$  to medium  $\epsilon_2$ . (b) An evanescent wave propagating along the x-axis.

**Figure 2.4:** Representation of the behavior of a 2D plane wave when the resonance condition is (a) not fulfilled and (b) fulfilled. An evanescent wave occurs and propagates along the x-axis instead of reflecting at angle  $\beta$  when the resonance condition is satisfied.

$$n_1 \sin(\alpha) = n_2 \sin(\beta) \quad (2.4)$$

Equation 2.4 corresponds to the following equation:

$$k_{x1} = k_{x2} = k_x \quad (2.5)$$

An expression for  $k_y$ , the y-component perpendicular to the interface can be found by combining Equation 2.3 and Equation 2.5:

$$k_{y2}^2 = n_1^2 \left( \frac{2\pi}{\lambda} \right)^2 \left( \frac{n_2^2}{n_1^2} - \sin^2(\alpha) \right) \quad (2.6)$$

As mentioned, for a wave to propagate the exponent in Equation 2.1 must be complex. For  $n_1 > n_2$ , the ray of light is given a bent away from the normal when entering a substance of lower RI. As a consequence, the right hand side of Equation 2.6 becomes negative as a result of  $\sin(\alpha) > \frac{n_2}{n_1}$ . This gives a purely imaginary  $k_y$ . Thus, it can be concluded from Equation 2.1 that there is only a traveling wave parallel to the interface of medium 2. This is mathematically given as:

$$E_{ew} = E_{amp} e^{(-k_{y2}y)} \cdot e^{(j\omega t - jk_x x)} \quad (2.7)$$

where  $E_{ew}$  is denoted as the evanescent wave, and the terms  $E_{amp}$ ,  $k_x$ ,  $k_y$ ,  $\omega$ ,  $t$ , and  $j$  have the same definitions as in Equation 2.1. Figure 2.4b illustrates the evanescent wave propagating along the x-axis.

Since the amplitude of the electric field  $E_{amp}$  exponentially decays along the y-direction with a characteristic distance  $1/jk_{y2}$ , the evanescent wave  $E_{ew}$  only extends a few hundred nanometers into medium 2 [50, 84]. Then, by considering Equation 2.6 the penetration depth of the evanescent field can be calculated – typically in the order of half a wavelength [50]. Hence, the evanescent field is only present close to the interface. Therefore, only a change in the dielectric property (e.g. a change in the refractive index) in the vicinity of the interface will influence the field [50].

## 2.2.2 Dispersion Equations and Resonance

The dispersion relation can be described as the relation between the angular frequency  $\omega$  and the wave vector  $\mathbf{k}$  [50]. A plane-polarized (p-polarized) light is utilized to express the complex reflection coefficient  $r_p$  due to its perpendicular electric field component. This is a requirement to induce surface charge density, also known as surface plasmons. By Fresnel's equations,  $r_p$  for any interface between two mediums for the p-polarized incident light electric field can be given as:

$$r_p = \frac{E_{inc}}{E_r} = |r_p| e^{i\varphi} = \left| \frac{\tan(\alpha - \beta)}{\tan(\alpha + \beta)} \right| e^{i\varphi} \quad (2.8)$$

where  $E_{inc}$  is the incident electric field,  $E_r$  is the reflected electric field, and the angles  $\alpha$  and  $\beta$  are defined as in Equation 2.4. For the interested reader, a derivation of Fresnel's

equations from Maxwell's equations can be found in "Foundations of Electromagnetic Theory" by Reitz et al. [85]. The phase change  $\varphi$  appearing in Equation 2.8 is determined by the refractive indices  $n_1$  and  $n_2$  of the materials involved and can be given as the relation between the incident and the reflected electric field. The reflectance, defined as the ratio of the reflected intensities [50], can be related as:

$$R_p = |r_p|^2 \quad (2.9)$$

Moreover, Cardona [86] described the occurrence of two extremes for Equation 2.8, that will affect Equation 2.9.

1. If  $\alpha + \beta = \frac{\pi}{2}$ : The very large value of the denominator of Equation 2.8 causes zero reflection of the p-polarized light. Thus,  $R_p$  becomes zero.
2. If  $\alpha - \beta = \frac{\pi}{2}$ : From Equation 2.8 and 2.9, the incident electric field  $E_{inc}$  becomes very small, while the reflected electric field  $E_r$  becomes infinite. Hence,  $R_p$  becomes infinite, correspondent to the *resonance* condition of  $R_p$ . By utilizing the relations between  $\alpha$  and  $\beta$ ,  $\cos(\alpha) = -\sin(\beta)$  and  $\tan \alpha = \frac{k_{x1}}{k_{y1}} = \frac{-n_2}{n_1}$ , the dispersion relation for an interface between two half-infinite media can be deduced [50]:

$$k_x^2 = k_1^2 - k_{y1}^2 = k_1^2 - k_x^2 \frac{\epsilon_1}{\epsilon_2} \quad (2.10)$$

$$k_x = \frac{\omega}{c} \sqrt{\frac{\epsilon_1 \epsilon_2}{\epsilon_1 + \epsilon_2}} \quad \text{and} \quad k_{y_i} = \frac{\omega}{c} \sqrt{\frac{\epsilon_1^2}{\epsilon_1 + \epsilon_2}} \quad (2.11)$$

where  $\epsilon_1$  and  $\epsilon_2$  are the dielectric constants of material 1 and 2, respectively, and  $i=1$  or 2.  $\omega$  is the angular frequency and  $c$  represents the propagation velocity in vacuum.

Thus, the physical effect on the material initiates oscillations of the free surface electrons in the material, resulting in an electromagnetic (EM) field near the interface.

If one of the mediums is a metal, the dielectric constant  $\epsilon_2$  becomes negative as a result of the free electrons in the metal and that the angular frequency  $\omega$  becomes smaller than the plasma frequency  $\omega_{pf}$  ( $\omega < \omega_{pf}$ ). This gives:

$$\epsilon_2(\omega) = 1 - \frac{\omega_{pf}^2}{\omega^2} \quad (2.12)$$

$$\omega_{pf} = \sqrt{\frac{4\pi n_e e^2}{m_e}} \quad (2.13)$$

The plasma frequency is determined by the free electron density  $n_e$ , electron charge  $e$ , and electron mass  $m_e$ .

Generally, this implies that for  $\omega < \omega_{pf}$ , no electromagnetic field can propagate in a metal, which can be determined by Equation 2.1 and 2.2 [50]. However, electromagnetic waves can propagate strictly along with the interface with evanescent tails extending into both sides of the interface if  $\epsilon_2 > -\epsilon_1$  is satisfied [50]. The reason is that the  $k_x$  remains real, while  $k_{y,z}$  becomes imaginary. Only certain materials can fulfill this resonance condition.

## 2.3 Localized Surface Plasmon Resonance

Localized surface plasmon resonance (LSPR) occurs when discrete metallic nanoparticles smaller than the wavelength of the incident light interact with the photons of the incident light. The interaction leads to a non-propagating collective oscillation of free electrons in the conduction band of the metal [16], as illustrated in Figure 2.5. The electron oscillations create a significant enhancement of the electromagnetic field close to the metallic nanoparticles, also denoted as the local EM field. This makes the LSPR method more sensitive to changes in the local refractive index surrounding the nanoparticles. This can be substantiated by the short decay length of  $\sim 10\text{-}30$  nm of the electromagnetic field [87, 88]. The short EM field also enables the identification of biomolecules that are only bound to the sensor surface. Thus, the contributions from the bulk effect or false positive signals by biomolecules distant from the sensor surface as well as uncontrollable signal fluctuations can be reduced.

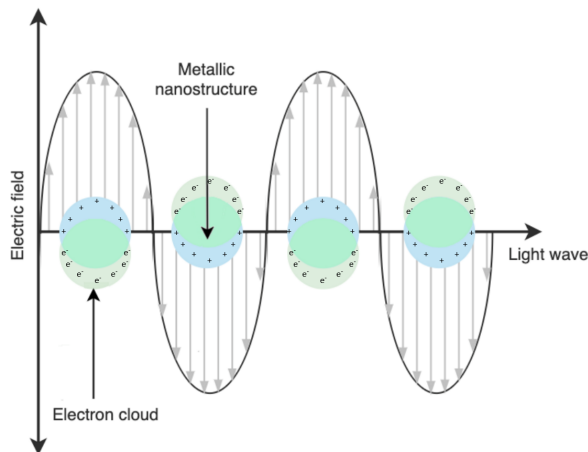


**Figure 2.5:** The localized surface plasmon resonance generates plasmon oscillations through the interaction between the incident light and the metallic nanostructures.



The LSPR-based sensor is instrumentally simple, where all the complexity lies in the surface of a chip. As a result of the large temperature independence of the LSPR signal, the instrumentation for output read-outs requires neither adaptive optics nor thermal controls. In addition to the short EM field, precise signals can be measured for specific target quantification of different types of assay enhancements by performing amplification steps in saliva, urine, plasma, or serum, e.g. surface functionalization.

The first use of LSPR wavelength shift measurements for sensing the change in local refractive index was reported by Englebienne [89] in 1998. Some years later, in 2003, Raschke et al. [90] published the first report using single gold nanoparticles in single-nanoparticle LSPR sensing. In 2005, Haes et al. [91] reported the first description of a clinical diagnostic procedure using LSPR wavelength-shift sensing [47]. Later on, the LSPR spectroscopy of metallic nanoparticles has shown to be a powerful technique for biological and chemical sensing experiments. An explanation of the LSPR wavelength shift measurements is explained in the following section.

## 2.4 Nanoplasmonics

Nanoplasmonics is the study of the optical phenomenon in the nanoscale vicinity of metal surfaces. In other words, nanoplasmonics is the use of nanostructures to enhance the interaction between light and matter. Every conductive metal has free electrons, which means that they are not bound to a specific atom. They can move across the solid material. On noble metal nanostructures, the free electrons convert into localized charge-density oscillations, also known as surface plasmons (SPs), by focusing nanoscale light below the diffraction limit. The diffraction limit is often referred to as half the width of the wavelength of the light used to see the specimen. This effect only arises if the particles are nanosized, hence, the phenomenon will only occur if the wavelength is smaller than the incident light.

The metallic nanostructures can be suspended in a fluid, be part of a rough surface, or be affixed to a surface. Illumination of the metallic nanosized particles will initiate three important characteristics.

### 1. Electromagnetic enhancement around the nanoparticle.

Plasmon excitation at the interface appears when incident light impinges the metallic nanoparticle. The nanoparticle absorbs the energy of the electromagnetic field of the light to create its own field, which dramatically enhances the EM field surrounding the particle. This field is much stronger than that of the incident light and is referred to as electromagnetic enhancement. A visualization of the EM field around the nanoparticle can be seen in Figure 2.6. The increased field strength is shown by the two red dotted areas.

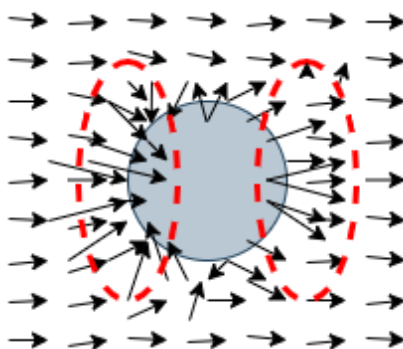


**Figure 2.6:** Illustration of the enhanced electromagnetic field around a metallic nanoparticle.

### **2. The enhancement has a resonance frequency.**

For a certain resonance frequency, the enhancement is especially powerful. The frequency can be tuned as a result of its dependency on the environment surrounding the particle and the nanoparticle characteristics.

### **3. Resonance shifts based on environment, material, size, and shape.**

The resonance frequency shift depends on the environment and the particle structure, including shape, size, and material. When the medium experiences a change in its surroundings, a resonance frequency shift occurs.

Since the resonance frequency shift is dependent on the environment surrounding the metallic nanoparticle, nanoplasmonics can be utilized for a variety of applications, including medical diagnostics, food safety, and drug discovery. In this master thesis, nanoplasmonics will be used in an LSPR-based sensor to determine the optimal sensor parameters for exosome detection. The introduction of a small substance containing a low concentration of exosomes can provide bindings between the exosomes and the metallic nanostructures. This connection will change the surroundings of the nanoparticle, provoking a change in the resonance frequency. The shift in the resonance frequency can be utilized in the study of molecular binding interactions.

## **2.4.1 Light Scattering and Absorption**

Consider a light beam traversing through a medium. The propagating wave of the light beam becomes attenuated in the propagation direction as a result of the intensity losses substantiated by scattering and absorption. This can be seen in Figure 2.7. The net loss of the energy intensity of the light beam is called extinction, i.e. absorption plus elastic light-scattering spectrum [47]. Absorption, scattering, and extinction can be utilized to measure the optical properties of the metallic nanostructures in biomolecular science.

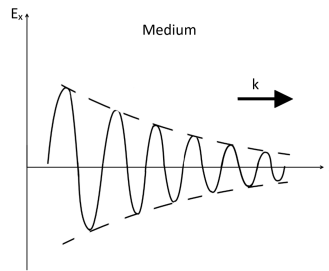


**Figure 2.7:** Visualization of attenuation of light in the propagation direction ( $z$ -direction).

## Scattering

As explained by Kasap [82], scattering of an electromagnetic wave implies that a portion of the energy in a light beam is directed away from the original direction of propagation for a small dielectric particle.

One scattering process is obtained when a propagating EM wave strikes a dielectric particle or molecule smaller than the wavelength of the incident EM light. The interaction between them results in a coupling of electrons due to the polarization of the particle. These couplings start to oscillate with the electric field of the wave, i.e. electronic oscillation [82]. The oscillation generates radiation of EM waves in all directions around the molecule, as illustrated in Figure 2.8. The scattered waves depend on the polarization and shape of the particle. This produces an intensity loss of the incident light in the original propagation direction as a result of the partially re-radiated wave light in different directions.

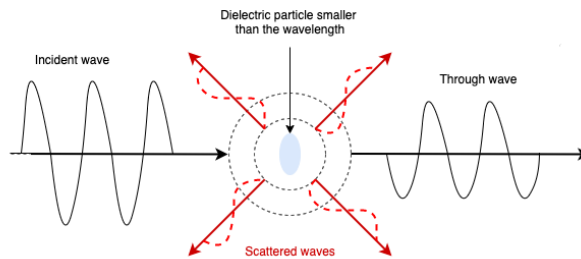


**Figure 2.8:** A visual representation of scattering of an electromagnetic wave by a small dielectric particle.

When the nanoparticles are considerably smaller in size (diameter  $d$ ) than the wavelength  $\lambda$  of the incident light ( $d \ll \lambda$ ), the scattering provided is defined as Rayleigh scattering [82, 92, 93]. In this case, the particle size is typically smaller than one-tenth of the wavelength [82]. The Rayleigh scattering occurs when there is a disparate region in the medium containing a different refractive index. This inhomogeneous region induces a change in the medium permittivity and polarizability, making it similar to a dielectric particle scattering

electromagnetic (EM) waves in all directions.

The energy of the photons does not change in Rayleigh scattering and can be defined as elastic scattering. The maximum of the dielectric loss caused by electronic polarization occurs at ultraviolet frequencies, where most of the energy is coupled. Therefore, for increasing wavelengths, the scattering decreases.

### Absorption

Absorption is the phenomenon where some of the energy from the EM wave is converted into another form of energy (generally heat). All particles with an electric charge can absorb light, where the absorbed energy and momentum increase the vibrational and rotational energy or the internal energy of the particle. This leads to effects such as heating, atom transitions, and ionization.

Figure 2.9 illustrates an absorption process, denoted lattice absorption that dissipates energy from the EM wave. As a result of relative displacement between positive and negative ions in a solid, the propagating wave forces these ions to vibrate at the frequency of the wave. This is called ionic polarization. In frequencies in the infrared (IR) region, the lattice vibrations have their natural frequency, which results in an energy peak. At these frequencies, the vibrations from the ions cause the ion lattice to vibrate. Most of the energy from the EM wave is absorbed by the ion lattice vibrations and is converted into lattice vibrational energy, i.e. heat. This absorption can be associated with the resonance peak [82].

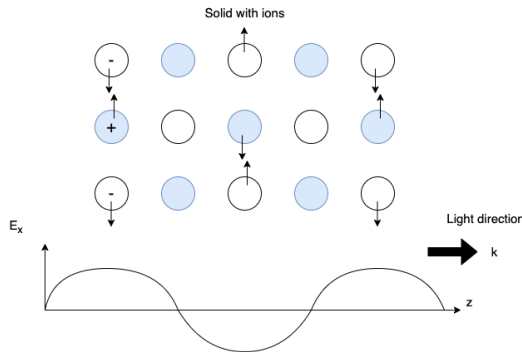


**Figure 2.9:** Representation of lattice absorption of an electromagnetic wave, where the energy from the wave is converted into lattice vibrational energy.

Energy absorption from the EM wave can also occur when there are ionic impurities in a medium. The particles charged by the EM wave couple with the electric field and start oscillating. Mechanical oscillations appear owing to the bonding of the oscillating ions and their neighboring atoms. This results in the generation of lattice waves and energy absorption from the EM wave.

## 2.4.2 Spectral Shift in Plasmon Spectroscopy

Plasmon spectroscopy has proven to be an ultrasensitive method for chemical and biological molecule detection. The ability to study light-matter interactions has made the plasmon phenomenon a key component in enabling surface-enhanced spectroscopic methods, including surface-enhanced Raman scattering, surface-enhanced infrared spectroscopy, and second harmonic generation [47].

Each nanostructure has a spectral signature of its plasmon resonance and can be modified by changing the material, size, shape, or environment [47, 94, 95, 96, 97]. When the surface-confined electromagnetic wave and the metal surface interact, a shift in the plasmon resonance condition occurs. The interaction can be observed in three modes; *wavelength shift mode* (measuring the reflection of light with a constant incident angle), *angle-resolved mode* (measuring the reflection of light with a constant wavelength), and *imaging mode* (2D analysis with a constant wavelength and incident angle, where a specific region on the sample is examined, mapping the reflectivity of the surface as a function of position) [47]. For measuring local refractive index changes with LSPR, the wavelength shift mode has shown to be the most common method among researchers.

In general, the excitation of LSPR only requires the right photon energy and polarization without a specific magnitude or direction of the incident light momentum [98]. At the plasmon resonance frequency (when the resonance condition is fulfilled), the absorption and scattering of light by the nanoparticles (i.e. light extinction) occurs with maximum intensity [16]. As a result of the highly sensitive electromagnetic enhancement close to the nanoparticle surface, the polarizability of the nanoparticle will be affected by any changes in the local dielectric environment. This change leads to a variation in the resonance frequency, which in turn will vary the optical extinction spectrum. In particular, there will be a noticeable shift in the wavelength where the maximum light extinction occurs, also referred to as the LSPR peak wavelength [16]. An illustration of the wavelength shift is presented in Figure 2.10.

For example, the shift in the LSPR peak wavelength  $\lambda_{max}$  can occur through the presence of an adsorbed species, which causes a change in the local environment (in the dielectric constant  $\epsilon$  or refractive index  $n$  ( $\epsilon = n^2$ )) surrounding the metallic nanoparticles. This change can be determined by the following relationship, which is the basis of LSPR wavelength-shift sensing experiments [47]:

$$\Delta\lambda_{max} = m\Delta n \left[ 1 - e^{\left(\frac{-2d_{al}}{l}\right)} \right] \quad (2.14)$$

where  $\Delta\lambda_{max}$  is the change in the maximum wavelength,  $m$  is defined as the bulk refractive index response from the nanoparticles,  $\Delta n$  is the change in the refractive index induced by the adsorbate,  $d_{al}$  is the effective adsorbate layer thickness, and  $l$  is the decay length of the electromagnetic field. It should be mentioned that Equation 2.14 does not consider the effect of the nanostructure and its characteristics on the EM field. This can

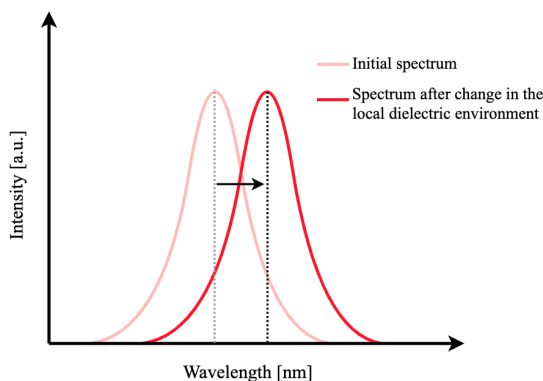


**Figure 2.10:** Shift in the LSPR peak from an initial state (pink curve) to higher wavelengths when the refractive index changes at the metal interface (red curve).

provide small errors in the measurement outputs.

As mentioned, for plasmonic spectroscopy, each nanoparticle has its own read-out spectrum with a peak wavelength. Considering LSPR-based sensing, the LSPR peak wavelength position can be tuned throughout the visible, near-infrared, and infrared light spectrum by changing the material, size, shape, and interparticle spacing of the nanoparticles. This allows the LSPR sensor to adapt to the specific bioapplication and enables enhanced sensor specificity.

## 2.5 Factors Affecting the Sensitivity of a Localized Surface Plasmon Resonance Biosensor

To determine the optimal plasmonic-based platform for chemical and biological analysis, several reviews have investigated and attempted to optimize a variety of figure of merits (FOMs). The FOMs are traditional biosensor characteristics and can be defined as a quantity used to characterize the performance and utility of a device, system, or method. The FOMs, also described as measurement capabilities, consist of elements including sensitivity, selectivity, response time, linearity, stability, limit of detection, and dynamic range. In this work, only the sensitivity and factors affecting the sensitivity performance will be discussed. For a more detailed technical description of the other biosensor characteristics, the reader is referred to the books by J. S. Wilson [99] and Homola & Piliarik [100].

The sensitivity of nanoplasmonic sensors is primarily associated with the refractive index sensitivity of the metal. The refractive index sensitivity impacts the sensitivity towards macromolecular adsorption as well as the possible probing volume. Sensitivity can also be referred to as the ability of the sensor to distinguish between small differences in the

concentration of the target analyte [101]. The sensitivity  $S$  can be defined as the ratio of the maximum wavelength shift,  $\Delta \lambda_{max}$ , and the change in refractive index,  $\Delta n$ , given in nanometers per refractive index unit (nm/RIU):

$$S = \frac{\Delta \lambda_{max}}{\Delta n} \quad (2.15)$$

Localized surface plasmon resonance (LSPR) is selected as the sensing method for the nanoplasmonic experiments in this work. The LSPR wavelength has the potential of being modified by changing the size, shape, interparticle spacing, environment, and composition of the sensor. This allows the LSPR sensor to adapt to the specific bioapplication and obtain the highest possible refractive index sensitivity. By considering these aspects and its ability for real-time sensing, the LSPR sensing method has shown to be an ideal platform for the detection of multiplexed exosomes.

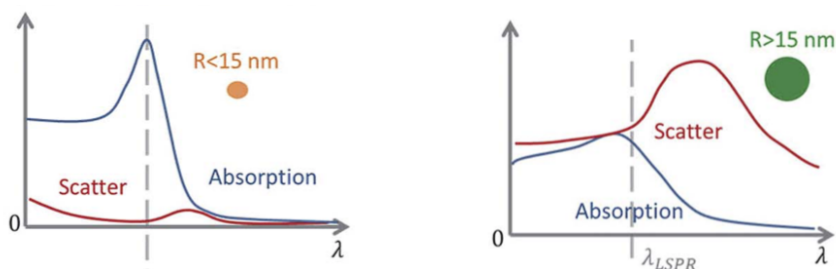
### Composition

The electric field intensity and the scattering and absorption cross-sections are greatly enhanced at the LSPR frequency, which for gold, silver, and copper lie in the visible region [102]. Silver and gold are the most attractive metals for optical applications because copper easily oxidizes. Silver nanoparticles exhibit higher bulk refractive index sensitivity and a lower damping constant than gold; however, the plasmon bands are located at shorter wavelengths (blue shift) compared to gold nanoparticles. Considering that the near-infrared (NIR) region of the light spectrum is preferred for most *in vivo* studies in biological applications due to the high transmission of tissue, blood, and water in this region [103], the practical use of silver in exosome detection is limited. Another significant limitation is that silver nanoparticles suffer from chemical instability both in air and aqueous environments [104]. Hence, gold is used in the nanoplasmonic sensor designs in this work owing to its stability and chemical inertness.

### Size

The practical sensing resolution, also known as the minimum detection limit depends on the absolute magnitude of the plasmon intensity [105]. Thus, nanoplasmonic structures that obtain intense scattering or absorption cross-sections are desirable and important for sensitive biological and chemical detection. The size of the nanoparticles affects the plasmon intensity, where the size determines if the absorption or scattering cross-section dominates. Li et al. [87] found that for small metal nanoparticles (radius  $R < 15$  nm), the electron-electron scattering (Møller-scattering) rapidly converted the energy of the LSPR into heat, resulting in a strong absorption. For the larger particles ( $R > 15$ ), a strong scattering cross-section was obtained as a result of a reduced Møller-scattering and the re-radiated plasmon energy into the scattering field. Their results can be seen in Figure 2.11.

Haes et al. [94] demonstrated the tunability of LSPR in the visible region by using silver periodic particle arrays (PPAs) fabricated by nanosphere lithography (NSL), which can be seen in Figure 2.12. They showed that by increasing the in-plane width, a shift towards lower-energy wavelength occurred, while a shift towards higher-energy wavelength was a



(a) The absorption cross-section is large and the absorption dominates for small particles with a radius less than 15 nm. (b) The scattering cross-section dominates for big particles with a radius greater than 15 nm.

**Figure 2.11:** Illustration of the absorption and scattering cross-sections and their magnitude based on nanoparticle size. Images modified from Li et al. [87].

result of an increasing out-of-plane height of the nanoparticles. Therefore, changing the nanoparticle size can optimally scale systems for the specific bioapplication and produce a distribution of LSPR maxima. Hence, for this work, the LSPR spectrum can be tuned towards the near-infrared region for the detection of exosomes.

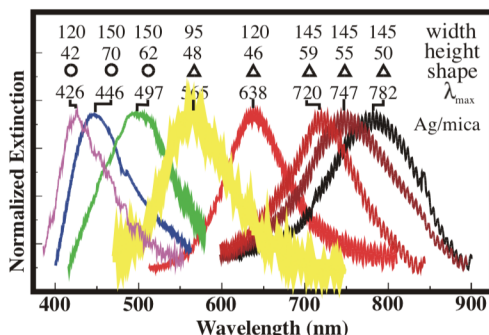


**Figure 2.12:** Ultraviolet-visible (UV-VIS) extinction spectra for silver PPA on mica substrate obtained by Haes et al. [94].

According to Raghu et al. [12], the nanostructures should be size-matched with the approximate diameter of a single exosome to detect their binding at the sensor surface and obtain a signal response. By utilizing smaller geometries, the exosome will be distinguished from larger extracellular compounds present in the sample. Additionally, utilizing a size similar to that of an exosome can increase the possibility of a digital response resulting from the accommodation of one or zero exosomes.

### Shape

Without changing the probing volume, the variation in geometry of the nanoparticles can tune the LSPR resonance spectrum shift in a biosensor. Jain & El-Sayed [106] observed that the nanostructures offering plasmon resonance tunability and strong field enhance-



ments also offer high plasmon sensitivity such as junctions (e.g. metal nanoshells [106, 107] and particle dimers [108]), and sharp curvatures and tips (e.g. nanorods [97, 109] and nanoprisms [110]). Other nanoparticle shapes that have been investigated include nanospheres [109, 111], nanotriangles [109], nanocubes [112], nanostars [111, 113] and nanoholes [114]. Previous reviews have also shown larger electromagnetic enhancements at the corners of the nanoparticles and in the spacing between them [95, 111, 115].

For this work, nanoholes have been selected as the nanoparticle geometry for the nanoplasmonic sensors. The optical properties of a nanohole-based sensor can be optimized for the specific bioapplication by changing parameters such as the metal thickness, the periodicity of the array, and the nanohole diameter [116, 117]. Nanohole arrays also yield simple fabrication, high extinction and scattering cross-sections, and are suitable for the integration in microfluidics enabling multiplexed detection. Additionally, LSPR can occur in an individual nanohole, leading to a highly concentrated EM field near the nanohole edge [10, 87, 118, 119]. This produces high sensitivity in the local refractive index surrounding the nanoholes. Table 2.1 presents the sensitivity performance and wavelength peak of nanohole arrays found in the literature. Sensor parameters including nanohole array, diameter, pitch (i.e. periodicity), and metal layer thickness are indicated.

**Table 2.1:** Sensitivity and wavelength peak for different nanohole arrays found in the literature.

Sensor parameters				Sensitivity [nm/RIU]	Wavelength peak [nm]	Reference
Lattice	nm Au	nm diameter	nm pitch			
Square	100 (Ag)	210	500	450	660	[119]
Square	100	200	510-618	400	633	[120]
Square	200	200	1400	1022	1550	[121]
Square (Double hole)	100	200 190 center spacing	600-800	600	850	[122]
Square	100	150	350-850	333	680	[123]
Square	150-200	300	1500	1520	1540	[124]
Square	220	130-180	11000	323	600	[125]
Square	40	70-200	500-600	393	1000	[126]
Square	80	200	550	271	750	[127]
Square	100	200	600	615	900	[128]
Square	100	200	600	522	750	[129]
Square	100	200	400	302	650	[130]
Square	125	200	600	600	850	[131]
Square	100	110-1000	450-1800	271	755	[132]
Square	50	100	450	286	800	[133]

### Alignment and Periodicity

Ekşioğlu et al. [118] and Cetin et al. [134] investigated and compared the performance of hexagonal and square lattice arrays for nanoholes. Their observations concluded that for a hexagonal alignment, the spectrum shift for various refractive indices resulted in higher sensitivity and larger spectrum shifts. Chung et al. [111] also explored different types of nanoparticle arrays. They observed that for a higher number of nanoparticles in the arrays, the LSPR shift did not change significantly. However, the resonance peak got sharper

owing to the increased particle interaction.

Further, several studies indicate that the periodicity of the array influences the sensitivity [7, 10, 135, 136]. The reviews by Negro [137] and Forestiere et al. [138] demonstrated that for plasmonic deterministic aperiodic nanostructures (DANS) larger values of field enhancement and stronger field localization occurred over larger surface areas than for reference periodic structures. Moreover, when two plasmonic nanoparticles come within close proximity to one another, the electromagnetic fields derived from the surface plasmon of the individual nanoparticles may be affected by the dipolar interaction of neighboring particles. This results in significant changes in both the plasmon resonance extinction and scattering spectra [105]. As the near-field-coupling-induced peak shift is dependent on the interparticle spacing, a larger coupling will be achieved by reducing the interparticle distances, while for an increasing interparticle distance, the coupling will decay exponentially [139, 140, 141, 142]. Additionally, Huang et al. [143] and Ferhan et al. [16] demonstrated that closely spaced metallic nanoarrays are the attractive lattice structure with lattice coupling of multipole plasmon modes for plasmonic applications.

## 2.6 Microfluidics

Microfluidics is the science and technology of systems that process or manipulate small ( $10^{-9}$  to  $10^{-18}$  liters) quantities of fluids, using channels with dimensions of tens to hundreds of micrometers [144]. The development of lab-on-chip (LOC) devices for the miniaturization of biological and chemical laboratories in a single chip has made microfluidics an emerging research field. Microfluidics has been used for controlled manipulation of micro- and nano-objects through its integration in different stimulation systems, including optics, acoustics, electrics, hydrodynamics, and magnetism [145, 146].

Many microfluidic applications such as drug delivery, DNA sequencing, and biochemical analysis require efficient and rapid mixing. However, mixing at the microscale only occurs through diffusion across the interface between the fluids in a microchannel. This is an effect of the low Reynolds number flow regime in microfluidics, where the laminar flow is dominant. Considering that the diffusion-dominated mixing is inherently slow and insufficient in most microfluidic devices, various approaches towards efficient mixing have been developed. The developed micromixers can be categorized into active and passive mixers. The active mixers apply an external force, generating disturbances or chaotic advection of the flow fields, such as ultrasound, electrokinetic instabilities, and integrated microvalves or pumps [147]. On the other hand, passive mixers do not use external forces but utilize the microchannel geometry to generate chaotic advection or increase the time and contact area between the fluids to enhance molecular diffusion. Methods for passive mixing may include interdigital multi-lamellae arrangements, collision of jets, or chaotic mixing by eddy formation and folding [147]. More information concerning microfluidic mixers can be found in the reviews by Hessel et al. [147], Lee et al. [148], Nguyen & Wu [149], and references therein.

The work in this master thesis considers an acoustic-based active mixing technique, where surface acoustic waves and two interdigital transducers are used to generate chaotic advection. The flow conditions for this micromixer can be decided by two of the characteristic dimensionless numbers when studying fluids – the Reynolds number ( $Re$ ) and the Péclet number ( $Pe$ ). The Reynolds number characterizes the ratio of inertial forces to viscous forces:

$$Re = \frac{\rho U D_h}{\mu} = \frac{U D_h}{\nu} \quad (2.16)$$

where  $\rho$  is the fluid density,  $U$  is the fluid velocity,  $D_h$  is the hydraulic diameter, and  $\mu$  and  $\nu$  are the dynamic and kinematic viscosity of the fluid, respectively. The hydraulic diameter  $D_h$  is used for non-circular channels and tubes and is expressed by the cross-sectional area  $A$  and the wetted perimeter  $P$  of the cross-section:

$$D_h = \frac{4A}{P} = \frac{4wh}{2w + 2h} = \frac{2wh}{w + h} \quad (2.17)$$

Here,  $w$  and  $h$  represent the width and the height of the tube or channel.

The Reynolds number allows the identification of the laminar or turbulent flow regime. For  $Re < 2000$ , the flow is defined as laminar, where the viscous forces dominate the inertial forces. When  $Re$  lies between 2000 and 4000, the viscous forces are comparable to the inertial forces. This region is determined as critical flow, and eddies will begin to occur. For  $Re > 4000$ , the flow is turbulent and the inertial forces dominate. For most microfluidic cases, laminar flow and low Reynolds numbers can be expected. This can be substantiated by an example, where water flows through a rectangular microchannel with width  $w = 200\mu m$  and height  $h = 100\mu m$  at a flow rate of  $U = 100\mu m/s$ . Then, the Reynolds number becomes:

$$Re = \frac{998kg/m^3 \cdot 10^{-4}m/s \cdot 1.33 \times 10^{-4}m}{1.003 \times 10^{-3}kg/ms} \approx 0.01 \quad (2.18)$$

The Péclet number characterizes the mixing at the microscale and can be defined as the ratio of mass transport by convection and that of diffusion [149]:

$$Pe = \frac{UL}{D} \quad (2.19)$$

where  $U$  is the fluid velocity,  $L$  is the characteristic length scale, and  $D$  is the diffusion constant. For  $Pe < 1000$ , the mixing is diffusion-dominant, whereas, convection dominates for higher Péclet numbers.

Figure 2.13 presents a comparison of the microchannel sizes found in the literature and the microchannels used in this work. The microchannels have a height of  $56 \mu\text{m}$  and a width of  $100 \mu\text{m}$ . To the author's knowledge, the microchannel size used in this work is the smallest reported in the literature.

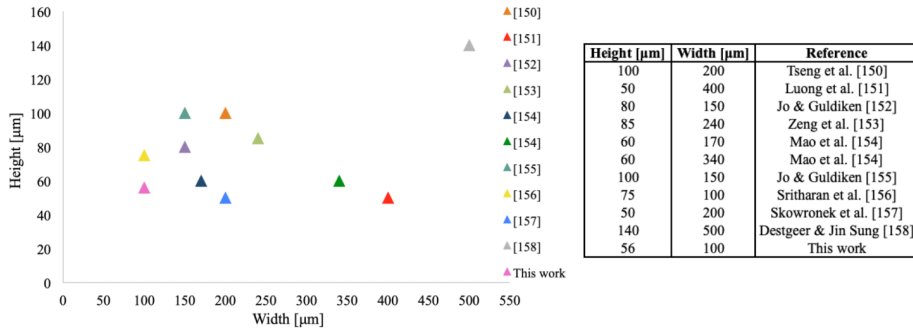


**Figure 2.13:** Comparison of microchannel sizes utilized in the literature and this work.

## 2.7 Acoustofluidics

Acoustofluidics can be defined as the integration of acoustic fields with microfluidics [159], the integration of ultrasound-based external forcing of microparticles in microfluidics [160], or as the fusion of acoustics and fluid mechanics. Acoustofluidics has become a growing research field in physics, engineering, biology, medicine, and chemistry.

Acoustofluidics has enabled processes such as biochemical analysis, disease diagnosis, DNA sequencing and drug delivery, isolation and manipulation of extracellular compounds [161] through fast and effective fluid actuation and particle manipulation. Moreover, sample preparations such as cell sorting and separation, cell lysis, and heating [145, 158] have been achieved by only applying acoustic waves [162, 163, 164, 165]. This reduces the operational cost and increasing the simplicity of the system.

This section gives an introduction to surface acoustic waves (SAWs), interdigital transducers (IDTs), and microfluidic mixing. A historical review of SAWs and IDTs is presented in Figure 2.14. These concepts will be combined to achieve active acoustic mixing in a microchannel.

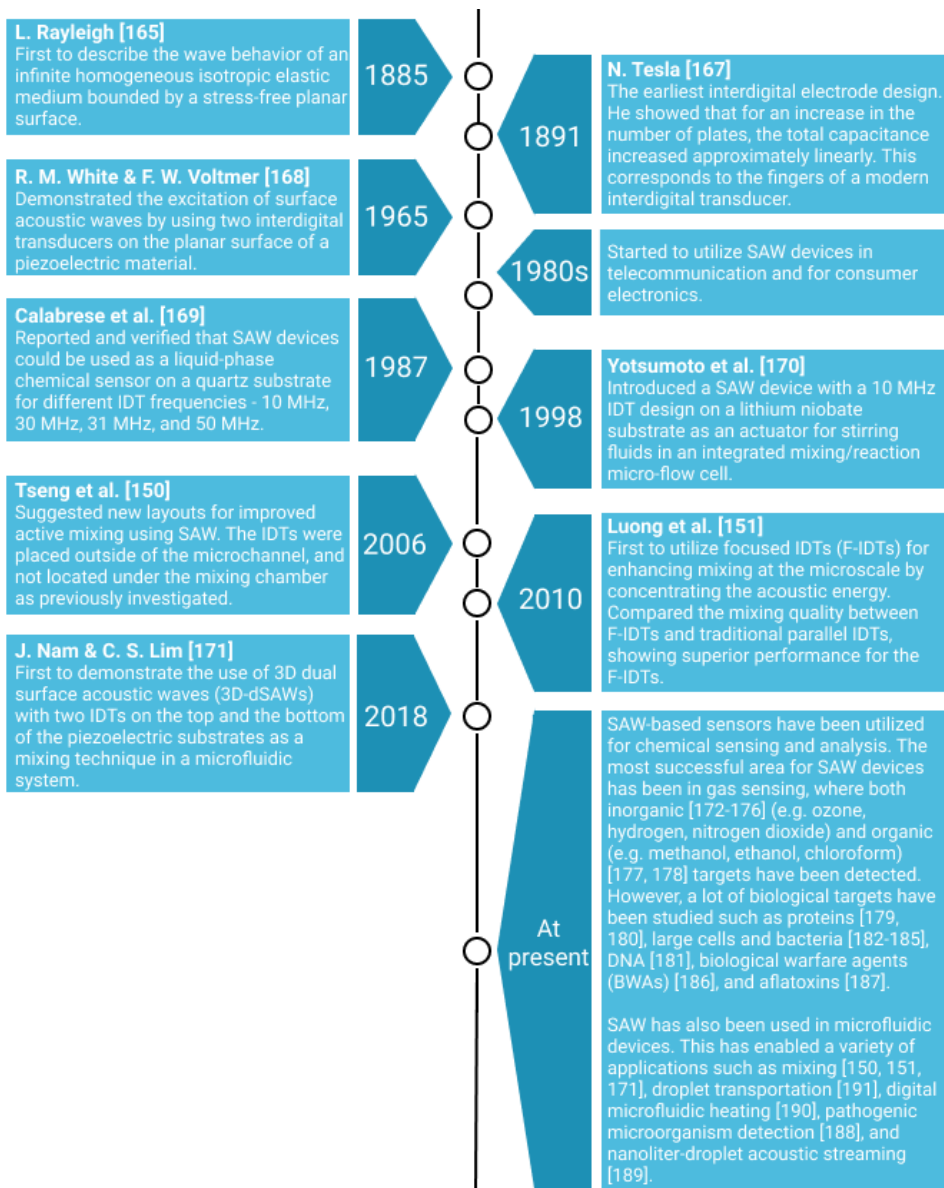


**Figure 2.14:** A historical timeline of surface acoustic waves and interdigital transducers featuring important findings and inventions.

### 2.7.1 Surface Acoustic Waves

Surface acoustic waves can be described as modes of elastic energy propagating at the surface of a solid [192] or as waves propagating along the surface of an elastic material [193]. By utilizing a piezoelectric material, SAWs are easily generated and detected.

In recent years, surface acoustic waves have shown great potential to control fluids and particles in lab-on-chip devices in an efficient way. They have shown the ability for fluid actuation, including mixing, pumping, jetting, atomizing, and manipulation of micro-objects such as droplets, particles, and cells through sorting, separation, focusing, and trapping. Additionally, a SAW-based microfluidic device offers a combination of advantageous features; simple fabrication, versatility, non-invasive properties, contact-free particle manipulation, high biocompatibility, low costs, and convenient integration with other microfluidic components [158, 193, 194]. Thus, the SAW-based microfluidic device has the capability of becoming considerably beneficial in clinical applications, biological research, and LOC applications.

Surface acoustic waves used in microfluidics can be divided into two categories – traveling surface acoustic waves (TSAW) and standing surface acoustic waves (SSAW). A TSAW is a wave propagating through the system, while an SSAW results from the interference of two generated SAWs traveling towards each other, creating a one-dimensional (1D) SSAW electric field. The work in this master thesis builds upon the TSAW principle to enable mixing through chaotic advection.

#### Traveling Surface Acoustic Waves

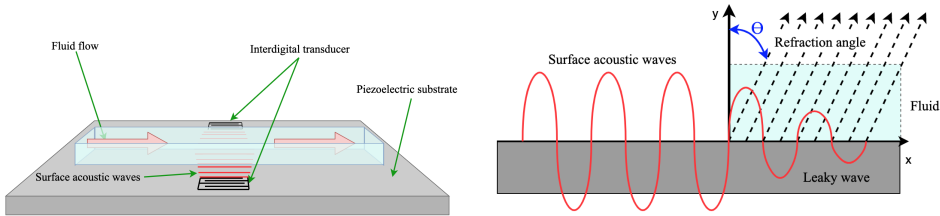
The traveling surface acoustic waves have become an important component in LOC devices. Many of the LOC applications require mixing of fluids, and as a consequence of the low Reynolds number regime in microfluidics, the laminar flow is dominant. Thus, mixing only occurs by diffusion, which is too slow for most LOC devices. For that reason, fast mixing of fluids by generating chaotic advection through SAW-induced streaming has been explored. It has resulted in reviews demonstrating microfluidic technologies enabled by TSAWs such as fluid mixing, fluid translation, jetting and atomization, particle/cell concentration, droplet and cell sorting, and re-orientation of nano-objects [193].

When a SAW is generated, its acoustic energy is transferred from the piezoelectric substrate to the solid-liquid boundary. This is shown schematically in Figure 2.15a. Consequently, the SAW changes mode to "leaky SAW" due to the mismatch between the acoustic velocities of the solid and the liquid medium [195]. The acoustic energy leakage excites longitudinal waves into the liquid at a specific angle ( $\theta = \sin^{-1}(v_{lw}/v_{SAW})$ ), illustrated in Figure 2.15b. This comes as a consequence of the phase-matching at the interphase between the two mediums, given by the refraction law (the ratio of the speed of sound in the fluid and the solid [150]). The longitudinal waves damp exponentially with an attenuation length of  $L_{SAW}$ , which can be determined by Equation 2.20 [195]:

$$L_{SAW} = \frac{1}{\alpha_L} = \frac{\rho_s v_{SAW} \lambda_{SAW}}{\rho_l v_{lw}} = \frac{\rho_s v_{SAW}^2}{\rho_l v_{lw} f} \quad (2.20)$$

Here,  $\alpha_L$  is the attenuation coefficient per unit length scale of the Rayleigh wave,  $\rho_l$  is the density of the liquid,  $\rho_s$  is the density of the substrate material,  $v_{lw}$  and  $v_{SAW}$  are the velocity of the longitudinal wave in the fluid and the SAW velocity in the substrate respectively,  $\lambda_{SAW}$  is the SAW wavelength, and  $f$  is the resonant frequency. From Equation 2.20, it can be seen that  $L_{SAW}$  is inversely proportional to the resonant frequency, indicating that the attenuation increases with the SAW frequency [195].

The emission of the longitudinal waves from the SAW into the liquid generates a force in the propagation direction of the longitudinal waves and induces flow within the liquid in the microchannel [193]. The activated motion in the liquid is then reflected by the microchannel walls, producing internal streaming. Thus, the internal streaming can enable and enhance the mixing of fluids in an efficient way.



(a) Visualization of the excited surface acoustic waves by interdigital transducers radiating energy into the fluid perpendicular to the fluid direction. (b) Energy transfer between the surface acoustic wave and the fluid.

**Figure 2.15:** Schematic representation of the energy transfer from the generated surface acoustic waves by interdigital transducers to the fluid on a piezoelectric substrate.

## 2.7.2 Interdigital Transducer

An interdigital transducer (IDT) is a comb-shaped metallic structure directly deposited on the substrate surface. IDTs are typically used for the excitation of surface acoustic waves. The SAWs are generated by applying an oscillating electrical signal matching the frequency of the IDT [196]. The generation of SAWs by IDTs relies on the piezoelectric effect of the piezoelectric material. The piezoelectric effect can be described as the generation of electric charge upon the application of mechanical stress in certain materials, while the generation of mechanical strain from the application of an electric field is the inverse piezoelectric effect [196].

Figure 2.16 presents different IDT parameters, determining the resonance frequency  $f$  of the surface acoustic wave.  $f$  is defined as [192]:

$$f = \frac{C_{SAW}}{2d_f} \quad (2.21)$$

where  $C_{SAW}$  is the substrate acoustic velocity and  $d_f$  is the finger spacing.  $C_{SAW}$  depends on the material properties of the substrate, the propagation direction, and the thickness of the IDT [196]. The frequency influences the SAW attenuation length described in Equation 2.20, where a higher frequency will result in a more rapid decay with shorter decay lengths of the SAW dissipated into the liquid.

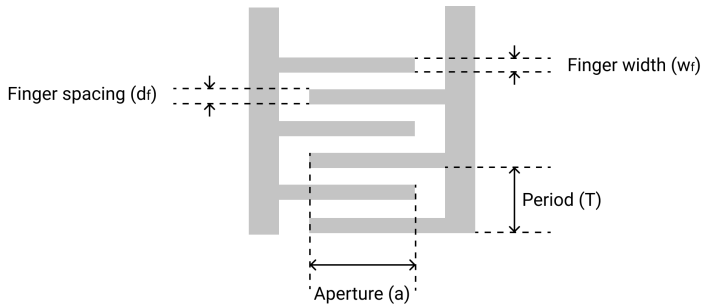


**Figure 2.16:** Visualization of IDT parameters.

Between the finger pairs in the IDT structure, an array of an electric field with alternating oscillations will occur. As a result of the inverse piezoelectric effect, the electric fields create alternating regions of compressive and tensile strain in the substrate [196]. Hence, the displacement in the material for each finger pair will oscillate with the electric field, which will excite a SAW. The wavelength of the generated SAW is also determined by the periodicity of the finger pairs.

In this master thesis, three different IDT designs will be utilized. The IDTs are made by an 80 nm thick gold layer and fabricated on a  $128^\circ$  Y-rotated X-propagating lithium niobate ( $LiNbO_3$ ) substrate with 25 finger pairs. The finger spacing and finger width of the electrodes are equal to  $25 \mu m$ ,  $12.5 \mu m$ , and  $8.6 \mu m$ , resulting in a resonance frequency  $f$  of 40 MHz, 80 MHz, and 120 MHz, respectively.

For a deeper description of IDT designs, the reader is referred to the review "Micro/nano acoustofluidics: materials, phenomena, design, devices, and applications" by Connacher et al. [196].

### 2.7.3 Microfluidic Mixing

Microfluidic mixing can be achieved by various methods categorized into passive or active mixing, as mentioned in Section 2.6. In this master thesis, three active SAW-driven mi-



cromixers are experimentally tested for both single and dual IDT designs at different flow rates and power inputs.

Microfluidic mixing in a microchannel or microchamber using a single IDT has been investigated for surface acoustic waves, and to some extent, for bulk acoustic waves [197, 198]. Many of the articles found during the literature review regarding SAW-based mixing have been related to mixing in droplets [189, 192, 199, 200]. To the author's knowledge, little focus has been invested in SAW-based microfluidic mixing using dual IDTs as well as for the difference in the mixing efficiency for single and dual IDTs apart from a few studies [152, 171, 201]. Nam & Lim [171] concluded that the mixing efficiency more than doubled when using a three-dimensional dual SAW (3D-dSAW) mixer compared to a single focused SAW mixer at the same voltage and flow rate. Similar results were found by Jo & Guldiken [152], where the mixing efficiency for the dual IDT design increased to 96.7% from 69.8% achieved with the single IDT design under identical operating conditions. The effect of increased mixing performance for the dual IDTs compared to single IDTs was also observed by Álvarez [201].

## 2.8 Summary

This chapter has provided information about fundamental concepts and phenomena in nanoplasmonic sensing, microfluidics, and acoustofluidics. Exosomes have been described as small biomolecular nanostructures in the size range of 30-120 diameters. They are found to be diagnostic biomarkers, containing beneficial characteristics including their specific lipid and protein composition, DNA and RNA content, and intercellular communication. The phenomena of surface plasmon resonance and localized surface plasmon resonance are explained; two powerful spectroscopy methods for biomolecular detection.

Three important characteristics of nanoplasmonics have been covered, explaining the electromagnetic enhancement around the nanoparticle, its resonance frequency, and the resonance shift through changes in the shape, size, material, and surrounding environment. As a result of the unique spectral curve for the specific nanostructure, a resonance shift can be measured by plasmon spectroscopy. The most common measurement method is the localized surface plasmon resonance-based sensor and has proved to be suitable for biological sensing experiments. Factors affecting the sensitivity performance of the LSPR-based sensor have been described, which include the composition, size, shape, alignment, and periodicity of the sensor.

Microfluidics has been presented, introducing the challenges and possibilities for lab-on-chip devices by manipulating small fluid quantities in microscale channels. Its challenges may be overcome by incorporating acoustofluidics. Acoustofluidics has been explained as well as two important elements for fluid actuation; surface acoustic waves and interdigital transducers. Microfluidic mixing utilizing active SAW-driven mixers with a single interdigital transducer has been found to be effective, although mixing with a dual IDT yields higher mixing performance.

# Chapter 3

## Micro- and Nanofabrication for Microfluidic Mixing Systems and Nanoplasmonic Sensors

Micro- and nanofabrication have been developed and utilized for applications in the semiconductor industry for several decades. However, this technology has contributed to the emergence of microfluidics and acoustofluidics, enabling the manipulation of micro- and nano-objects for chemical, biological, and physical studies. This chapter covers the central fabrication concepts for the production of the nanoplasmonic sensors, the microchannels, and the interdigital transducers used in the conducted experiments in this work. In addition, their fabrication processes, as well as the assembly of the microchannel and interdigital transducers, are presented.

### 3.1 Fabrication Concepts

A variety of techniques are used for the fabrication of micro- and nanoscale devices. Figure 3.1 illustrates different methods for both micro- and nanofabrication. The highlighted boxes are the relevant techniques for this master thesis, which include photolithography, soft lithography, electron beam lithography, and etching and substrate removal. These methods will be described in the following sections.

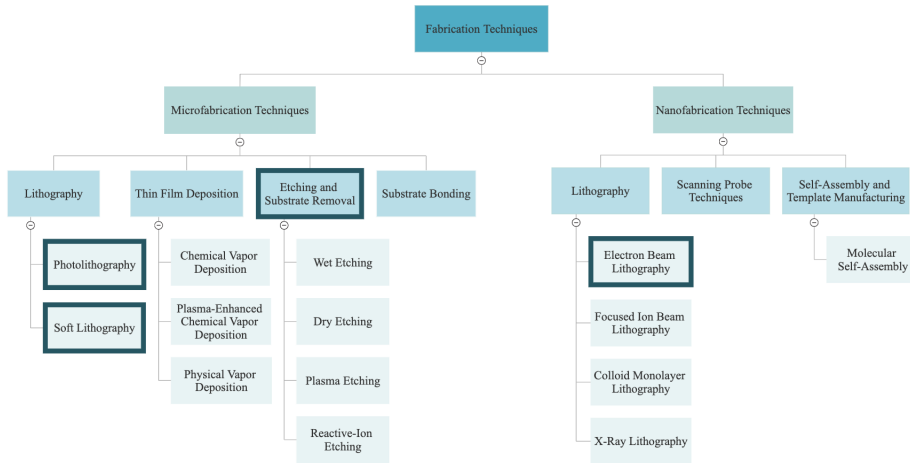


Figure 3.1: Fabrication techniques for micro- and nanoscale devices.

### 3.1.1 Lithography

Lithography is a general denotation given to processes producing a pattern on a substrate. There are a number of different lithography techniques separated by the method used for creating the desired pattern. Some of the techniques are:

- **Optical lithography or photolithography:** Uses ultraviolet (UV) light to generate the pattern [202].
- **Electron beam lithography:** Electron beams are used to create the pattern [202].
- **Ion beam lithography:** Energetic ions bombard the surface to generate the pattern.
- **Imprint lithography:** A mold is pressed or imprinted into a material to generate the pattern or the pattern is created by mechanical deformation of the resist.
- **Scanning probe lithography:** Utilizes a sharp probe in an atomic force microscope (AFM) to heat, scratch, oxidize or transfer substances to the surface of a substrate for patterning nanoscale features [203].

Lithography can be divided into masked and maskless lithography. Masked lithography utilizes a mold or mask to fabricate the pattern, and enables a high-throughput fabrication up to several tens of wafers/hr [203]. Photolithography, nanoimprint lithography, and soft lithography are types of masked lithography. Contrarily, maskless lithography creates arbitrary patterns without the use of masks. The serial manner to fabricate the pattern allows an ultrahigh-resolution patterning of arbitrary shapes with minimum feature size as small as a few nanometers [203]. Some of the lithography techniques in this category are electron beam lithography, ion beam lithography, and scanning probe lithography.

Photolithography, soft lithography, and electron beam lithography have been the selected techniques to fabricate the nanoplasmonic sensors, the microchannels, and the interdigital transducers used for the experimental campaign in this work.

### Photolithography

The most common lithography methods are optical lithography or photolithography. The photolithography technique utilizes an exposure of a light-sensitive polymer (photoresist) to UV light to define a desired pattern [203]. A general photolithography process is shown in Figure 3.2.

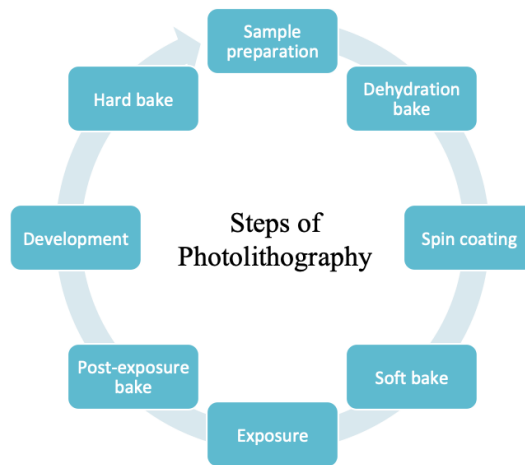


**Figure 3.2:** A standard photolithography process.

Initially, the substrate is cleaned to eliminate organic compounds or remove contaminants. This removal will increase the adhesion to the photoresist and reduce the possible comets produced during spin coating. For further increase in adhesion, a dehydration bake is performed to eliminate any absorbed water molecule on the surface with a high temperature, typically  $> 200^\circ$  [159]. Photoresist, a photosensitive organic polymer is spin-coated onto the substrate and creates a uniform thin film. The physical property of the resist and the rotation parameters will determine the final thickness of the thin film. Soft bake is performed to evaporate the solvent contained in the resist. This step will prevent the resist from sticking to the mask during exposure, increase the mechanical stability of the resist, and enhance the adhesion between the resist and the substrate. During exposure, UV light is illuminated through a photomask that consists of opaque features on a transparent substrate, e.g. quartz or glass [203]. When the UV light exposes certain areas, the photoresist will undergo a chemical change, modifying its solubility – either by becoming cross-linked, hardened and less soluble in a developer, i.e. a negative photoresist, or by breaking the polymer chains, making the resist more soluble in contact with its respective developer, i.e. a positive photoresist. The effect of using a negative or positive photoresist in a photolithography process is illustrated in Figure 3.3.

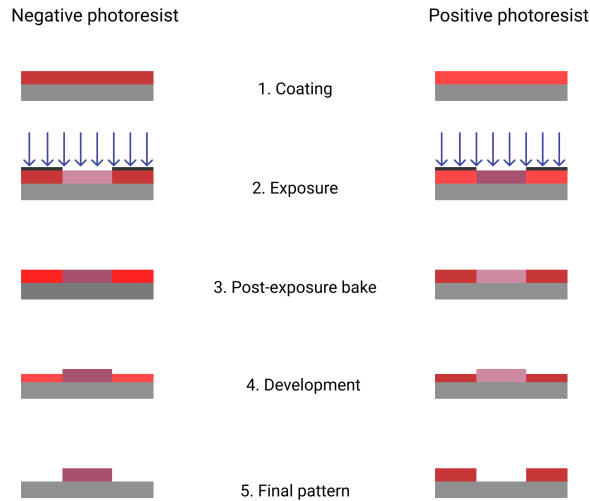


**Figure 3.3:** The effect on the photolithography result by using a negative or positive photoresist.

For chemical-amplified resists, the substrate goes through a post-exposure bake to further induce chemical change in the exposed regions [202]. To finalize the desired pattern transfer, a developer is applied to the substrate for removal of the non-cross-linked photoresist. To hard bake the substrate after development is optional, however, this step can improve the chemical and thermal stability of the resist.

### Soft Lithography

Soft lithography is a variant of nanoimprint lithography and is a non-photolithographic method for generating micro- and nanostructures and patterns. Soft lithography is used to generate patterns and structures with feature sizes ranging from 30 nm to 100  $\mu\text{m}$  [204]. An elastomeric stamp forms a large number of patterning techniques through molding, printing, and embossing. Some of these techniques are microtransfer molding, micro-contact printing, replica molding, micromolding in capillaries, injection molding, and cast molding [204]. An advantage of soft lithography compared to photolithography is its ability to transfer patterns on uneven, patterned, or nonplanar surfaces on a broader range of materials. Soft lithography can be divided into two main steps; fabrication of an elastomeric stamp or mold and the utilization of a predefined relief structure to deposit monolayers on the surface. Poly(dimethylsiloxane) (PDMS) is the most common material utilized for soft lithography. PDMS is a silicon-based organic elastomer that is isotropic and homogeneous with optical transparency down to  $\sim 300$  nm [204]. The elastomer is typically supplied in a two-component kit with a base (vinyl-terminated PDMS) and a curing agent (copolymers of methylhydrosiloxane and dimethylsiloxane mixed with a platinum complex) [159]. The low glass transition temperature keeps the base and curing agent as liquids at room temperature. When the liquid components are thoroughly mixed, the mixture cures to a flexible elastomer, either at room temperature in  $> 48\text{hr}$  or heat

cured in 10 minutes at 150° [205].

A standard approach for soft lithography to fabricate microfluidic devices is the utilization of cast molding to produce a mold by photolithography. Further, by using replica molding that duplicates an inverse version of the mold, the original mold can be reproduced. According to Xia & Whitesides [204], the mold can be used over fifty times without significant performance reduction.

### **Electron Beam Lithography**

Electron beam lithography (EBL) is a maskless lithography technique for pattern fabrication at the nanoscale. Highly focused electrons are utilized to make an exposure on an electron-sensitive resist. The instrument loads and reads an AutoCAD-design file with the desired pattern. With an electron-beam spot with a diameter as small as a couple of nanometers, the surface of the resist is scanned in a dot-by-dot fashion to generate the pattern in sequence [203]. The sequential writing of the electron beam can make the pattern transfer process time-consuming and is therefore not a preferred method for large-scale manufacturing. EBL can be used for sub-10 nm features, but the resolution is highly dependent on the instrument and the resist [159, 206].

The pattern transfer by electron beam lithography is a complicated process, containing a variety of interdependent variables to be determined for an optimal result. A visualization of the effect of size reduction and increment of the pitch and beam diameter can be seen in Figure 3.4.

- **Pitch:** The minimum distance between two adjacent dots or pixels that can be exposed is called pitch. A smaller pitch results in a higher resolution pattern. However, a smaller feature requires a longer exposure time. Hence, the pitch affects the exposure grip or beam stepping pitch of the EBL instrument. A general rule is that the pitch should be 80% of the beam diameter [207] in order to create intricate patterns.
- **Beam current:** The beam current defines how many electrons are impinging on the sample each second, which affects the maximum obtainable resolution [208]. A higher beam current will increase the writing speed of the instrument.
- **Exposure dose:** The exposure dose is the amount of energy deposited per unit area [208]. The spin-coated photoresist on the substrate, as well as the density and dimension of the pattern, determines the necessary dose. The exposure dose is typically measured in micro-Coulombs per square centimeters  $[\frac{\mu C}{cm^2}]$ .
- **Beam diameter:** The beam diameter can be controlled by changing the dose time. An increased dose time of the electron beam will reduce the minimum feature that can be produced during exposure. Further, a large beam diameter enables a shorter writing speed. If the beam diameter is smaller than the pitch, the pattern will not be smooth. This contributes to a lower resolution due to a large overlap in the shape [207].

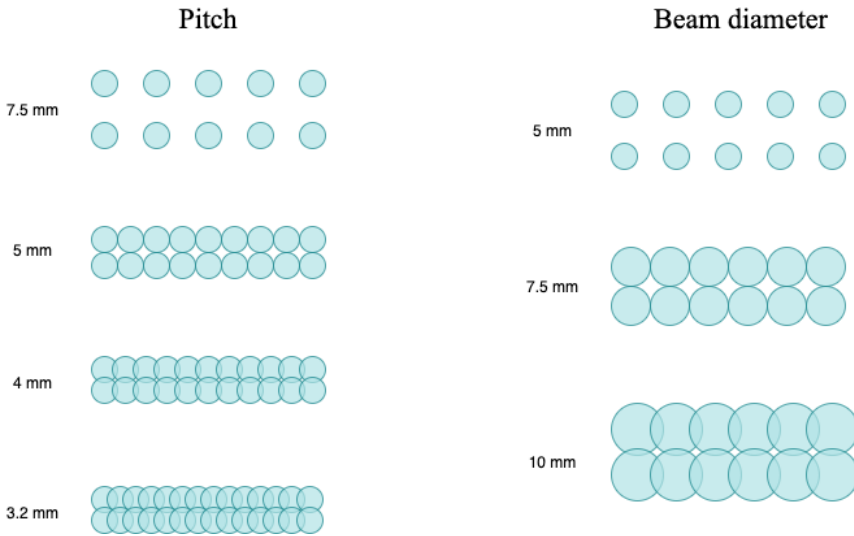


**Figure 3.4:** The effect on the pattern by reducing the pitch and increasing the beam diameter.

A more in-depth explanation of electron beam lithography can be found in the review by Ribe [159]. Moreover, Beckwith [209] and NTNU NorFab [207] provide additional information about improvements of EBL performance and the relation between pitch and beam current, respectively.

### 3.1.2 Metal Patterning

Multiple techniques exist for obtaining the imprint pattern on the substrate, such as etching, molding, and metallization and lift-off. Lithography used to pattern metal thin films is typically performed by utilizing an etch-back or lift-off procedure. The lift-off process is an additive pattern transfer, where the resist is first patterned and then deposited with a metal layer. The resist layer is then dissolved in a solvent, leaving metal in the areas without patterned resist. To perform the lift-off, the solvent needs to react with the resist layer. Hence, the lift-off is dependent on a non-continuous metal layer. The etch-back procedure is the reverse of the lift-off process. Thus, the metal layer is deposited with the resist pattern on top. Etching is a subtractive pattern transfer, where a wet or dry etching method specific to the metal layer is applied to etch the metal layer. When the metal in the open areas of the resist is removed, the etching is stopped and the remaining resist is dissolved [159].

The suitable method depends on the resist profile, which is determined based on the resist chemistry and exposure method. A representation of the different resist profiles can be seen in Figure 3.5. An undercut profile is achieved by using a positive electron resist or a negative photoresist. The undercut profile will simplify the lift-off process because the

resist profile will create a non-continuous metal layer when the metal layer is applied. This method can be considered as the image reversal mode. However, the mechanical stability of the resist is decreased. On the other hand, the overcut profile will give a homogeneous metal layer, which is not suitable for lift-off.



**Figure 3.5:** Schematic representation of the difference between an overcut and undercut resist profile for metal patterning.

In this master thesis, the image-reversal lift-off process is utilized to fabricate the interdigital transducers for enabling the excitation of SAWs in the microfluidic device. The fabrication procedure can be found in Section 3.2.3.

### 3.1.3 Surface Activation of PDMS

PDMS is a widely used silicone type within biological applications and microfluidics, and is applied for the fabrication of the microchannels utilized in this master thesis. However, the PDMS has a hydrophobic surface, which means a surface with an absence of affinity for water. Thus, the wetting of the microchannel with aqueous solutions is complicated, the microchannel is prone to adsorption of other hydrophobic species, and can easily nucleate bubbles [210]. Nevertheless, by surface activating the PDMS surface through plasma oxidation, the presence of silanol groups in the PDMS renders the surface hydrophilic. This produces a surface with a strong affinity for water. This will promote the aqueous solution filling in the microchannel and also facilitating the PDMS microchip bonding [211]. Additionally, it will irreversibly seal the oxidized PDMS to other materials used in microfluidic systems, such as glass, silicon, silicon oxide, and oxidized polystyrene [212].

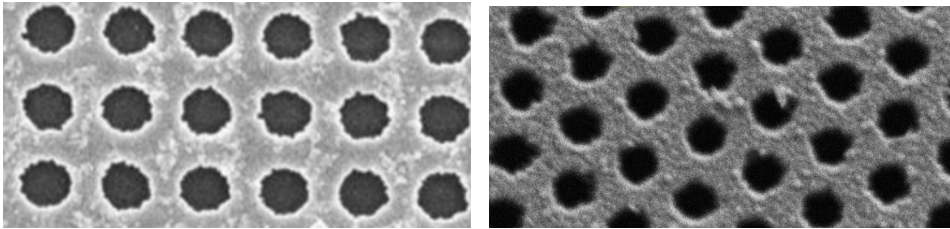
## 3.2 Fabrication Recipes

The fabrication of the nanoplasmonic sensors, the microchannels, and the interdigital transducers contain several different fabrication processes and techniques as described in the previous sections. This section presents the fabrication recipes for the three different components that are produced by Ribe [159]. The nanoplasmonic sensor and microchannel recipes have been validated by Saldaña [213]. A more thorough and detailed description of the fabrication steps, including fabrication parameters, utilized materials, chemicals, instruments, and additional equipment, can be found in Appendix A-E.



### 3.2.1 Fabrication Process of a Nanoplasmonic Sensor

The fabrication process presented in this subsection is utilized to fabricate nanoplasmonic sensors with a nanohole diameter of 400 nm, gold layer thicknesses varying from 200 to 250 nm, periodicities between 700 and 1100 nm, and square or hexagonal nanohole arrays. The difference between the square and hexagonal nanohole alignment is displayed in Figure 3.6.



(a) Square nanohole array. Image extracted from Saldaña [213]. (b) Hexagonal nanohole array. Image extracted from Saldaña [213].

**Figure 3.6:** Difference between square and hexagonal nanohole array. Images extracted from Saldaña [213].

The complete fabrication process is illustrated in Figure 3.7. A glass substrate is utilized for the fabrication of the nanoplasmonic sensors due to its transparency, which allows light to pass through the substrate. This enables spectroscopy analysis. Glass is an insulating surface, and as a consequence, the glass substrate must go through two additional steps compared to the substrates utilized in the fabrication processes in Subsection 3.2.2 and 3.2.3. The hexamethyldisilazane (HMDS) increases the liquid contact angle, which produces a more hydrophobic surface and improved photoresist adhesion. The conductive layer serves as a protective layer and is applied to ensure the dissipation of charges during electron exposure.

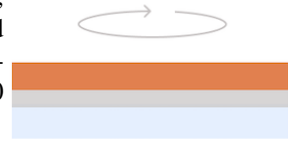
1. **Clean:** The sample is pre-treated through a cleaning step to enhance the final result of the nanoplasmonic sensor. The sample is cleaned with acetone, rinsed with isopropanol (IPA), and dried with nitrogen ( $N_2$ )(g) to remove contaminants on the substrate surface. Additionally, the substrate is placed in a plasma cleaner for physical and chemical ozone cleaning.
2. **Dehydration bake:** The substrate is dehydrated to remove any excess fluids on the surface.



3. **HMDS deposition:** Priming of the glass substrate is performed with HMDS through vapor deposition to enhance the adhesion of the resist. The substrate is placed in a desiccator with HMDS, where the chamber is vacuumed to increase the vapor pressure before air is introduced in the chamber again. The substrate is kept in the desiccator overnight to create a thin homogeneous HMDS layer.



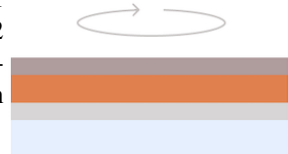
4. **Spin coating of photoresist:** The substrate is coated with a thin layer of the positive photoresist CSAR 6200.13, where a set of parameters are determined for the desired thin film thickness, including time, speed, and acceleration. The substrate is spun at a high speed (1000-6000 rpm) to form an even layer.



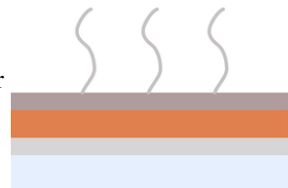
5. **Soft bake:** At this stage, the substrate contains up to 15% solvent, which may include build-in stresses [214]. Thus, the substrate is soft-baked to dehydrate the resist, which makes the photoresist more dense and resistant.



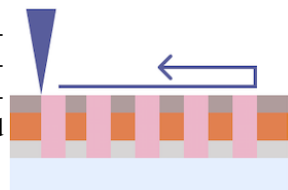
6. **Spin coating of conductive layer:** A conductive layer of the type Poly(methylmethacrylate) (PMMA) Electra 92 (AR-PC 5090.02) is spin-coated on the substrate for creating a path for the electrons to escape during the electron exposure. This enhances the exposure performance.



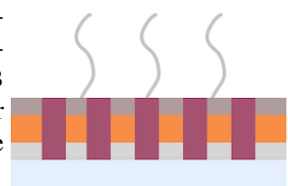
7. **Soft bake:** An additional soft baking step is completed for the same reasons as for the photoresist.



8. **EBL exposure:** The glass substrate is exposed to an electron beam by the instrument Elionix ELS-G100. This generates the desired pattern on the photoresist layer by determining EBL conditions, such as beam diameter, pitch, and exposure dose.



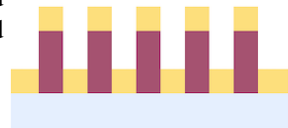
9. **Post-exposure bake:** Some of the reactions initiated during the electron exposure cannot be fully completed; therefore, a post-exposure bake (PEB) is performed. The PEB will improve the adhesion, reduce the excess resist after development, and increase the contrast and resist profile [214].



10. **Development:** To acquire the desired pattern, development is utilized to dissolve the soluble areas of the photoresist changed during the EBL exposure. The substrate is first submerged in water to disperse the thin conductive layer, and then in the AR 600-546 developer to remove the resisting layers. To stop the development process on the substrate, a 1:3 ratio of methyl isobutyl ketone (MIBK) and IPA (MIBK/IPA) is applied.



11. **Metallization:** The sample is cleaned with IPA and dried with  $N_2(g)$  before deposition of a 200-250 nm thick gold layer by the electron beam evaporator.



12. **Lift-off:** Remover AR 600-71 is applied to remove excess photoresist on the substrate, as well as the deposited gold on the photoresist areas. For enhanced lift-off of the gold layer, the substrate goes through an ultrasonic bath, where mechanical stresses improve the dissolution of the photoresist layer. Ultimately, the substrate is cleaned with acetone, rinsed with IPA, and dried with  $N_2(g)$ .



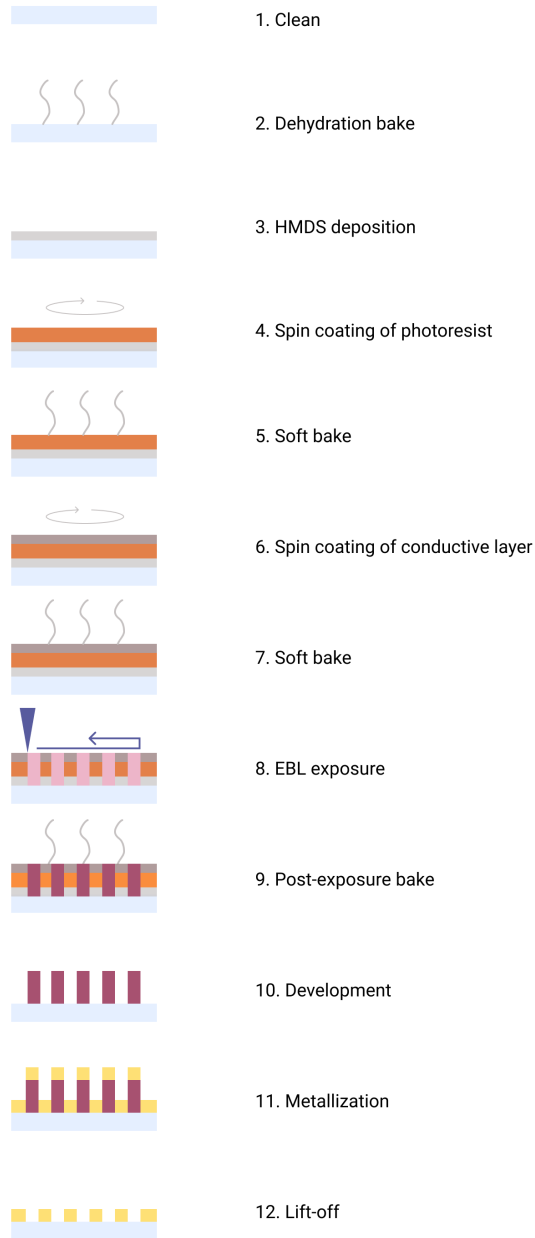


**Figure 3.7:** Fabrication process flow for the nanoplasmonic sensor using electron beam lithography for transferring the desired pattern.

### 3.2.2 Fabrication Process of a Microchannel

The microchannels used for the experiments in this work have a height of  $56\ \mu\text{m}$  and a width of  $100\ \mu\text{m}$ . A master or cast mold is manufactured by photolithography to fabricate the microchannel of PDMS on a silicon substrate. The fabrication process is shown in Figure 3.8. The two initial steps, cleaning and dehydration bake are equal to the glass substrate. The HMDS evaporation and the spin coating of the conductive layer are not necessary for this fabrication process due to the properties of silicon (e.g. semiconductor).

The PDMS microchannel walls absorb some of the acoustic energy transported by the SAWs from the piezoelectric substrate to the solid-liquid boundary. This affects the capability and efficiency of the device. Thus, the PDMS microchannel is cut in the last fabrication step to minimize the area covered by PDMS on the piezoelectric substrate carrying the SAW.

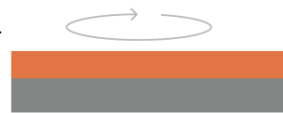
1. **Clean:** The silicon substrate is cleaned with acetone, rinsed with IPA, and dried with  $N_2(\text{g})$ . The substrate is further cleaned in a plasma cleaner for physical and chemical ozone cleaning.



2. **Dehydration bake:** The substrate undergoes a dehydration bake to remove excess fluid on the substrate surface.



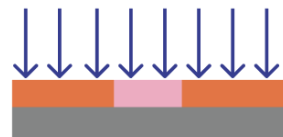
3. **Spin coating of photoresist:** The negative photoresist SU-8 3050 is spin-coated on the substrate. The thickness of the photoresist layer determines the height of the final microchannel.



4. **Soft bake:** As described in Subsection 3.2.1, a soft bake is necessary to dehydrate solvent left on the substrate surface. This will also make the photoresist more resistant and dense.



5. **MLA exposure:** The exposure is performed using the maskless aligner 150 (MLA-150) with a 375 nm wavelength laser. The MLA-150 uses UV light to fabricate the desired pattern.



6. **Post-exposure bake:** A PEB is necessary to complete the initiated reactions during exposure, and enhance the resist profile, the adhesion, and reduce excess resist after development.



7. **Development:** To dissolve the photoresist SU-8 3050, the substrate is submerged into the solvent-based developer mr-Dev 600, where the last seconds of exposure is under agitation. Then, the substrate is rinsed with IPA and dried with  $N_2(g)$  before silanization.



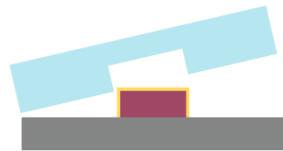
8. **Trichloro(1H,1H,2H,2H-perfluorooctyl)silane deposition:** The fabricated mold is silanized with trichloro(1H,1H,2H,2H-perfluorooctyl)silane, a fluorine-based silane. The silane is deposited by chemical vapor deposition, in the same manner as the HMDS deposition in Subsection 3.2.1. The silane reacts with surface hydroxyl groups in the substrate (e.g. silicon or PDMS), which together form covalent Si-O-Si bonds [159]. The silanization will ease the peeling of the PDMS from the mold, and enhance its durability.



9. **PDMS application:** The base and curing agent (Sylgard 184, Dow Corning) are mixed with a weight ratio of 10:1 to prepare the PDMS elastomer. The PDMS mixture is degassed under vacuum to remove any bubbles that occurred during mixing and then poured over the mold inside a petri dish.



10. **Curing and peeling:** The PDMS elastomer is cured in an oven to accelerate the polymer cross-linking, resulting in a hardened PDMS. Subsequently, the PDMS is peeled. To reduce the excess PDMS around the microchannel, the PDMS is cut using a scalpel.



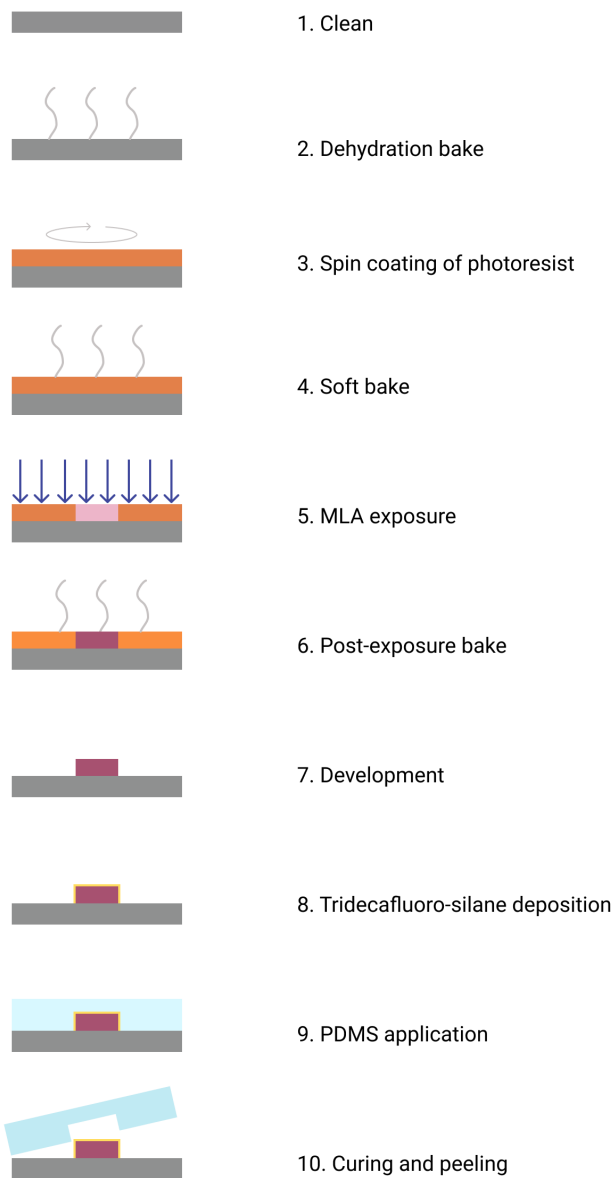


**Figure 3.8:** Fabrication process flow for the microchannel created by photolithography using a maskless aligner (MLA-150) and soft lithography.

### 3.2.3 Fabrication Process of an Interdigital Transducer

The fabrication process for the interdigital transducers is presented. The IDTs have equal finger width and spacing of  $25\ \mu\text{m}$  for the 40 MHz IDT design,  $12.5\ \mu\text{m}$  for the 80 MHz IDT design, and  $8.6\ \mu\text{m}$  for the 120 MHz IDT design. The IDT electrodes are created by an 80 nm thick gold layer and fabricated on a  $128^\circ$  Y-rotated X-propagating lithium niobate ( $\text{LiNbO}_3$ ) substrate, which possesses the piezoelectric effect.

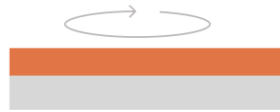
1. **Clean:** The  $\text{LiNbO}_3$  substrate is cleaned with acetone, rinsed in IPA, and dried with  $\text{N}_2(\text{g})$  before the substrate is placed in a plasma cleaner for physical and chemical ozone cleaning.



2. **Dehydration bake:** The excess fluids on the substrate surface are removed by a dehydration bake.



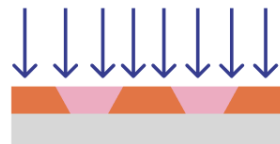
3. **Spin coating of photoresist:** The  $\text{LiNbO}_3$  substrate is spin-coated with the positive photoresist AZ 5214E. AZ 5214E is selected owing to its image reversal properties.



4. **Soft bake:** The excess solvent on the substrate surface and the photoresist are dehydrated with a soft bake process. The baking process gives a more resistant and dense photoresist.



5. **MLA exposure:** The MLA-150 is used for the pattern transfer by using a 405 nm wavelength laser. UV light is used to expose the desired areas of the photoresist to make the pattern.

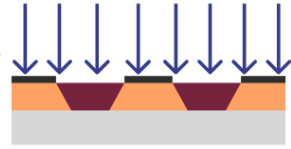


6. **Image reversal bake:** The substrate is baked above a specific temperature to activate the cross-linking agent in the photoresist and thermally cross-link the MLA-150 exposed regions [159].





7. **MA-6 flood exposure:** The mask aligner (MA-6) flood exposures to cut the polymer chains in the previously unexposed regions [159] to execute the image reversal.



8. **Development:** The resist is developed in the AZ726 MIF developer, where the non-cross-linked photoresist is dissolved. The sample is rinsed in deionized water (DI) and dried with  $N_2(g)$  before metallization.



9. **Metallization:** A thin gold metal layer is deposited on the patterned photoresist by the electron beam evaporator.



10. **Lift-off:** The substrate is submerged in acetone to lift off the metal layer on top of the photoresist by dissolving the underlying photoresist. Thus, a gold metal layer will be in the regions without photoresist.



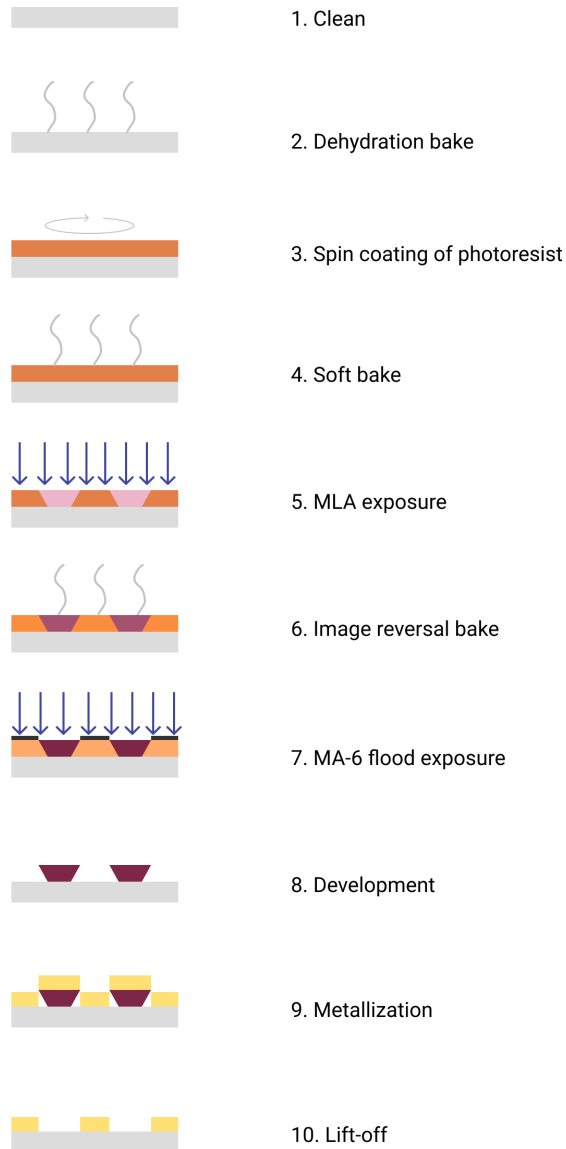


**Figure 3.9:** Fabrication process flow for an interdigital transducer by utilizing a maskless aligner (MLA-150) and a mask aligner (MA-6).

### 3.2.4 Assembly of the Microchannel and the Interdigital Transducers

The assembly of the microchannel and the interdigital transducers is a delicate process. The two elements need to be cross-linked with strong bonds and perfectly aligned to avoid leakages from the microchannel during the experiments.

The PDMS microchannel is treated in the plasma cleaner with short oxygen plasma to create a reactive surface. A few droplets of ethanol are placed on the IDTs on the  $LiNbO_3$  substrate to prevent bonding before the PDMS microchannel is in the desired position. Thus, the ethanol prevents direct contact and bonding retardation between the two elements. The ethanol also helps to reduce friction during alignment. To finalize the cross-linking of the IDTs and the PDMS microchannel and to enhance solvent evaporation, the combined elements are cured in an oven. The device is located on a platform, which allows the connection with the surface acoustic wave (SAW) generator. Moreover, the IDT electrodes are coupled with the platform through gold wires to enable the energy transfer from the SAW generator to the IDTs, and thus, generating the SAWs. This is performed with a wire bonder and gold wires with a diameter of  $25\ \mu m$ .

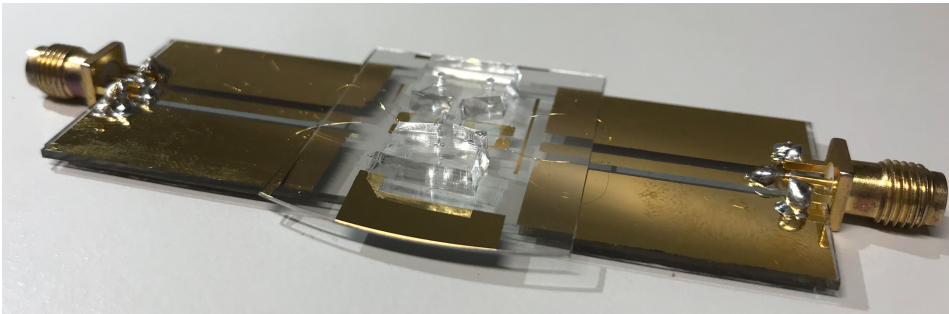


**Figure 3.10:** The microfluidic device bonded to the platform enabling the energy transfer from the SAW generator to the IDTs by gold wires with a diameter of  $25\ \mu m$ .

## 3.3 Summary

In this chapter, different fabrication methods including lithography techniques, metal patterning, and surface activation have been presented. Features affecting the final fabrication result such as the utilization of a positive or negative photoresist, an overcut or undercut resist profile, and the selection of pitch, beam current, exposure dose, and beam diameter for pattern fabrication have been described. The chapter also provides the fabrication processes utilized to manufacture the nanoplasmonic sensors, the interdigital transducers, and the microchannels as well as the assembly of the microfluidic device in this master thesis.

# Chapter 4

## Experimental Campaign

This chapter presents the NTNU acoustofluidics test facility, objectives of the experimental campaign, test procedure, data processing, and experimental uncertainties. The experimental campaign concentrates on finding the optimal nanoplasmonic sensor design with the highest sensitivity and determine the IDT design achieving the best mixing efficiency in a microchannel using surface acoustic waves.

### 4.1 The NTNU Acoustofluidics Test Facility

The NTNU acoustofluidics test facility aims to develop lab-on-chip devices for biomedicine and energy applications. The main focus is to apply nanoplasmonic biosensing of exosomes in combination with acoustophoresis-based fluid manipulation. This may enable the development of an integrated system for liquid biopsies capable of real-time monitoring and early cancer diagnosis. Acoustophoresis-based fluid manipulation is particle and cell manipulation due to its induced motion when subjected to an acoustic field [215].

The test facility seen in Figure 4.1 consists of a microscope, stage controller, light source, syringe pump, SAW generator, and a computer. The microscope used is Nikon Eclipse Ti2, which is an inverted microscope enabling spectrometry and microfluidic mixing analysis. The light source is located at the top of the microscope and is controlled by Ocean Optics HL-2000-FHSA, a fiber optic tungsten halogen light source, for spectroscopy or by a LED light source for microfluidic mixing experiments. The different objectives are placed underneath the platform area for sample holding. The platform area is regulated by Thorlabs – a stage controller consisting of a joystick for movement and a button for velocity control. For nanoplasmonic experiments, the light source and spectrometer Ocean Optics HL-2000-FHSA are connected to the computer. The data acquisition system utilized

for spectrum read-outs is Ocean Optics SpectraSuite, and MATLAB is used for further analysis and data processing. For the microfluidic mixing experiments, software programs are utilized to control the syringe pump (Omix Element) and the SAW generator (PSG Control 2), while Jai Control Tools are used for image recording. The SAW generator is connected to the substrate by a platform and transfer the energy to the IDTs by gold wires, as explained in Subsection 3.2.4. Microtubes are positioned in the two inlets and the outlet, where the flow rate is determined by the syringe pump system. For data processing, MATLAB is utilized.

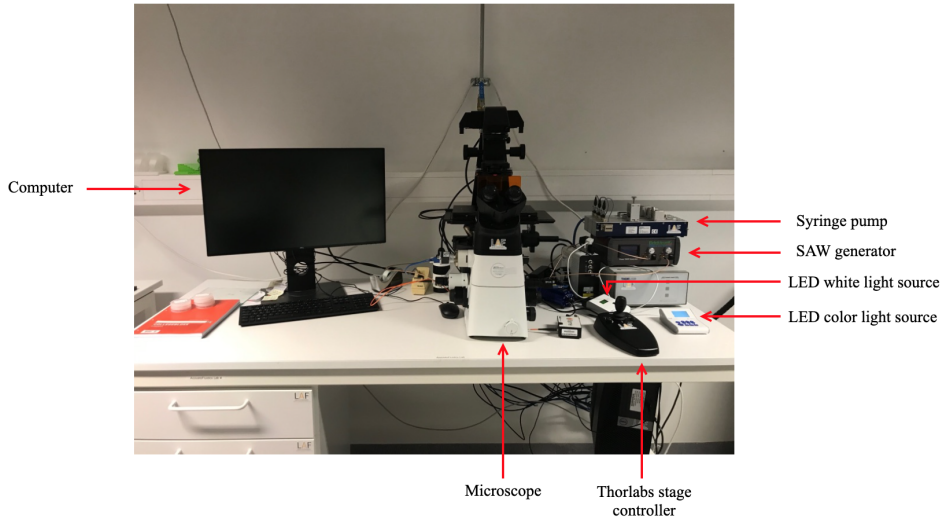


**Figure 4.1:** NTNU acoustofluidics test facility displaying relevant components.

## 4.2 Objectives

In accordance with the scope of the thesis, the experimental campaign will be conducted to complete the following objectives:

- Test and document how the different IDT designs, flow rates, and power applications affect the microfluidic mixing performance.
- Perform spectrometry analysis of the nanoplasmonic biosensor to determine the sensor sensitivity performance and investigate how different geometrical features affect the sensitivity.

## 4.3 Test Campaign

As a consequence of COVID-19, the lockdown of the NTNU Nanolab, and unavailable fabrication instruments due to maintenance, all experiments concerning a combined device were not possible to execute in the available time frame. However, the test campaign provides experiments of the nanoplasmonic sensors and the microfluidic mixing using SAWs. This has enabled the investigation towards finding the optimal parameters for the different elements to be incorporated in a label-free integrated system.

The microfluidic mixing performance using SAWs has been tested for three different IDT designs – 40 MHz, 80 MHz, and 120 MHz. The single IDT design performance was investigated for each design, while the dual IDT was tested for the 40 MHz and 80 MHz IDT designs. The mixing efficiency was investigated under green light ( $\sim 495\text{-}570\text{ nm}$ ) for flow rates between 500 and 4000  $\mu\text{L}/\text{h}$  and power applications from 0 mW to 2500 mW for each IDT design for a single and dual IDT.

The nanoplasmonic sensor experiments consider nanoholes with constant diameters of 400 nm, 200-250 nm gold layer thicknesses, different periodicities (the distance between each nanohole) ranging from 700 to 1100 nm, and square or hexagonal nanohole arrays for five different fluid mixtures (DI water and four glycerol concentrations – 10%, 30%, 50%, and 70%) with various refractive indices.

### 4.3.1 Microfluidic Mixing Test Procedure

The  $\text{LiNbO}_3$  substrate was placed on the platform area and connected to the SAW generator on each side of the platform. The SAW generator applied power to the IDTs, generating SAWs on the substrate surface. The generated SAWs were perpendicular to the flow direction in the microchannel. The forces acting on the fluids by the SAWs helped to produce vortices inside the microfluidic channel. This created chaotic flow, which could enhance mixing and particle motion. Thus, for a combined device with a nanoplasmonic sensor and a microchannel with active mixing using SAWs, the number of nanoparticles in contact with the surface could be increased, and enhance the overall detection performance of the nanoplasmonic sensor.

Underneath the substrate, an additional  $\text{LiNbO}_3$  wafer was placed to avoid light deviations and to enhance the image focus during the experiments. Further, a syringe pump holding two syringes was connected to the microchannel inlets by two tubes. One tube contained DI water and the other a 0.25% sulforhodamine B + DI water solution to quantify the mixing performance. The mixed fluids were collected at the outlet by an additional tube. The fluorescent dye sulforhodamine B was used to easily demonstrate the mixing effect during the experiments under green light. The sulforhodamine B concentration was selected based on a calibration curve, where 0.25% showed to be the most efficient and suitable concentration in terms of light intensity. The microfluidic mixing setup can be seen in Figure 4.2.

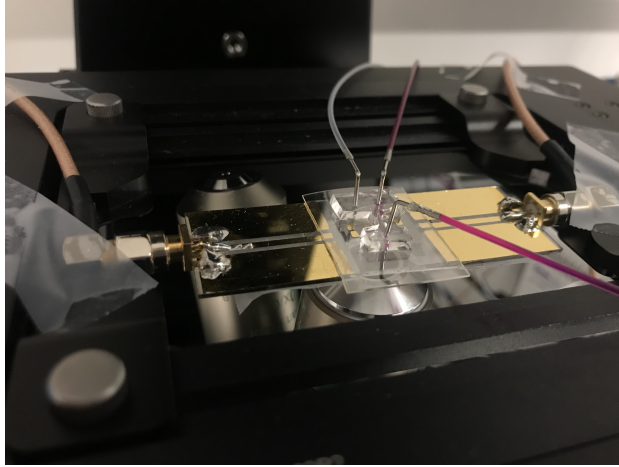


**Figure 4.2:** Microfluidic mixing setup showing the two inlets and the one outlet of the microchannel, the two interdigital transducers, and the SAW platform connected to the platform area of the microscope.

The logging of the microfluidic mixing was initiated when the fluids from the syringe pumps had stabilized at equal fluid streams in the microchannel. Experiments were performed to investigate the mixing performance for the different IDT designs and to determine the optimal parameters for the flow rate and power application for the IDT design yielding the highest mixing efficiency. The different IDT designs tested were a 40 MHz, 80 MHz, and 120 MHz IDT mixer, with a flow rate range of 500–4000  $\mu\text{L}/\text{h}$  and a power input ranging from 0 mW to 2500 mW. For every flow rate and power application of each IDT design, an image was taken to document the mixing effect. The exposure time was held constant at 14000  $\mu\text{s}$  for all the IDT experiments and the resistance in the SAW generator was 50  $\Omega$ . The test matrix for the microfluidic mixing experiments can be seen in Table 4.1.

**Table 4.1:** Test matrix for the microfluidic mixing experiments.

IDT design			Exposure time [ $\mu\text{s}$ ]	Flow rate [ $\mu\text{L}/\text{h}$ ]	Power [mW]
MHz	Finger width [ $\mu\text{m}$ ]	Finger spacing [ $\mu\text{m}$ ]			
40 80 120	25 12.5 8.6	25 12.5 8.6	14 000	500	0
				1000	500
				1500	1000
				2000	1500
				2500	2000
				3000	2500
				4000	

### 4.3.2 Nanoplasmonic Sensor Test Procedure

The experiments were conducted for different geometrical features and sensing mediums to analyze the sensitivity performance of the nanoplasmonic sensor devices. To carry out the spectrometry analysis, additional equipment was required. These can be found in Appendix E.

The glycerol mixtures utilized for the calibration of the different sensors were obtained by diluting glycerol in water. A scale was utilized to weigh the solute, the final solution, and the mass concentration of the mixture to obtain the desired glycerol concentrations. The refractive index for the different mixtures was analyzed and compared to the values obtained by Hoyt [216].

**Table 4.2:** The refractive index value for deionized water and different glycerol concentrations utilized in the conducted nanoplasmonic sensor experiments. Refractive index values are obtained from Hoyt [216].

Substance	Refractive index [-]
Deionized water	1.33303
10% glycerol	1.34481
30% glycerol	1.37070
50% glycerol	1.39809
70% glycerol	1.42789

The sample with the nanoplasmonic sensors was carefully placed on the platform area of the microscope with a tweezer. The first spectrum read-out for each sample functioned as a reference spectrum with air as the sensing medium. This spectrum was used to obtain the same initial position of the sensor for each fluid mixture on the sample to minimize the experimental uncertainties. For the other spectrum read-outs, a droplet of 12  $\mu\text{L}$  of the DI water or glycerol concentrations was dispensed on top of the nanoplasmonic sensor. A coverslip was positioned over the droplet to create a homogeneous distribution of the fluid and to avoid light deviation as a result of droplet curvature. Between each substance, the substrate was rinsed, cleaned, and dried according to the fluid used – only dried for the DI water and rinsed with IPA and dried for the glycerol concentrations. After cleaning, the sample was placed at the initial location on the platform area to test the same pattern on the nanoplasmonic sensor each time. The location was validated by comparing the air read-out spectrum with the initial reference spectrum curve for air. Figure 4.3 displays the nanoplasmonic sensor test setup.

### 4.3.3 Data Processing

#### Microfluidic Mixing

Prior to analyzing the obtained mixing efficiency results from the different IDTs, fluorescent images of the microchannel were taken before and after the generation of SAWs





**Figure 4.3:** Experimental setup of the nanoplasmonic sensor displaying the microscope, objective, and a sample with 10 nanoplasmonic sensors.

on the substrate surface. The images were utilized to define the region of interest (ROI) and visually demonstrate the mixing performance by the intensity of the DI water and sulforhodamine B solution.

MATLAB has been used to investigate the intensity change over the microchannel length for different flow rates and power applications. MATLAB has also been utilized to determine the mixing efficiency based on the method defined by Luong et al. [151]. The method was selected among others due to the possibility to compare the obtained results with those found in the literature [150, 151, 152, 171, 217]. The mixing efficiency was determined as the ratio between the mixing index of mixed streams and unmixed streams over a region of interest obtained from the fluorescent images [152]:

$$\eta(t) = 1 - \frac{\sqrt{\frac{1}{N} \sum_{i=1}^N \bar{I}_i(t) - \bar{I}_\infty^2}}{\sqrt{\frac{1}{N} \sum_{i=1}^N \bar{I}_i(0) - \bar{I}_\infty^2}} \quad (4.1)$$

where

$$\bar{I}_i(t) = \frac{I_i(t) - I_{min}}{I_{max} - I_{min}} \quad (4.2)$$

At first, the intensity value for each pixel was extracted. The average intensity obtained from each pixel of each line  $i$  at time  $t$  along the width of ROI was determined as  $I_i$ .  $\bar{I}_i(0)$  and  $\bar{I}_i(t)$  indicate the normalized average intensities of each line  $i$  over ROI at the initial unmixed state (before SAWs were generated) and mixed state, respectively.  $\bar{I}_i(t)$  was

normalized based on the maximum and minimum intensity value of the unmixed states.  $N$  was the number of lines along the width of ROI, while  $\overline{I_\infty}$  was the expected normalized intensity at the completely mixed state. For this master's thesis,  $\overline{I_\infty} = 0.5$  due to the identical flow rate for each fluid stream in the microchannel.

For example, when there is no excitation of SAWs, the distribution of the fluorescent mixture (0.25% sulforhodamine B and DI water) and the DI water remained at the lower and upper part of the microchannel, giving  $\eta = 0$ . Thus,  $\eta = 1$  when the fluorescent particles fill the microfluidic channel width, resulting in complete mixing.

### **Nanoplasmonic Sensor**

Measurements were carried out using Ocean Optics SpectraSuite. The obtained spectra had small fluctuations due to noise contributions. The noise contributions were reduced by taking an average of 10 measurement readings. This enhanced the polynomial fitting of the spectra when processing the results in MATLAB.

The spectra of the DI water and glycerol concentrations utilized for each sample were analyzed in MATLAB. The script located the wavelength intensity peak from the imported data and created a polynomial curve that matched the respective spectrum. Both the width of the spectrum and the polynomial order could be selected, where a higher polynomial order would result in improved accuracy of the wavelength tracking. The wavelength intensity peak of the polynomial curves was matched with the ones obtained from the spectrum data extracted from Ocean Optics SpectraSuite. MATLAB has also been used to calculate the sensitivity obtained by the nanoplasmonic sensors and create a calibration curve showing the shift in both the refractive index and wavelength peak for the spectra.

### **4.3.4 Experimental Uncertainties**

**Noise:** Various contributions from different sources caused noise, especially in the nanoplasmonic sensor measurements. The contributions of the unwanted data reduce the measurement quality. The noise could come from environmental fluctuations, various energy quantities such as photons in light, and the instruments utilized to perform the experiments. As explained in Subsection 4.3.3, the noise contributions are reduced by taking an average of the data points for the nanoplasmonic sensor spectra.

It is worth mentioning that cells are especially sensitive to changes in environmental conditions. They will cause noise in the measurements due to their cellular responses [218]. Hence, for further experiments with biological samples, the environmental fluctuations should be highly considered and controlled to obtain the best detection capability possible.

**Nanoparticle geometry, alignment, and composition:** The fabrication process of the nanoplasmonic sensors described in Subsection 3.2.1 utilizes a variety of instruments, time intervals, and temperature-dependent processes. As a consequence, the different elements

impose uncertainties, including the uncertainty factor of human error. Thus, the desired parameters such as structure, alignment, and composition will not be constructed perfectly, and may not produce identical sensor characteristics.

**Nanoplasmonic sensor readings and polynomial regression curve fitting:** As mentioned in Section 2.5, the sensitivity is defined as the ratio between the maximum wavelength shift and the change in the refractive index. For the sensitivity measurements of the nanoplasmonic sensors, the change in the refractive index is kept constant. Thus, the wavelength shift determines the sensitivity. Owing to oscillating nanoplasmonic measurements around the critical peak of the curve, a precise curve fitting is challenging, where the polynomial order will affect the sensitivity value. For a nanoplasmonic sensor with hexagonal nanohole arrays, a constant nanohole diameter of 400 nm, a 250 nm gold layer thickness, and periodicity of 1000 nm, a polynomial with order 15 ( $P=15$ ) gave a sensitivity of 297.4163 nm/RIU, while  $P=25$  and  $P=50$  gave sensitivities of 283.6045 nm/RIU and 276.4618 nm/RIU, respectively. Thus, an important verification criterion became a visual confirmation of the curve fittings matching the data points near the peak.

As a consequence of the sensor sensitivity dependency of the polynomial order, the utilized sensitivity values for the presented cases in Section 5.2, are means of the following polynomial orders;  $P=15$ ,  $P=25$ , and  $P=50$ . A mean is utilized to minimize the uncertainty of the exact sensitivity value. The largest difference in sensitivity was found for the nanoplasmonic sensor with the characteristics of 250 nm gold layer thickness, 700 nm periodicity, nanohole diameter of 400 nm, and hexagonal nanohole arrays. The lowest and highest sensitivity obtained was 101.3902 nm/RIU and 185.7299 nm/RIU, respectively, corresponding to a variety of 58.75%. This percentage is not satisfactory and the effect of the polynomial order on the sensor sensitivity should be further investigated.

**Reference image for determining complete mixing in Equation 4.1:** The power applied in the microfluidic mixing experiments produces particle motion, which will affect the light intensity. Higher power inputs result in lower light intensity. Since the lower flow rates require lower power applications, which will be discussed in Chapter 5, the intensity of the mixed state will not be representative for higher flow rates. As a consequence, the most suitable reference for the mixed state is selected based on the different IDTs and flow rates. This could influence the obtained mixing results and create uncertainties when comparing the mixing efficiencies between the different flow rates and the IDT designs.

**Power limitations of the IDTs:** According to the website of Belektronig [219], the power range of their SAW generator (the one used for the conducted experiments) is between 40  $\mu W$  and 4 W. However, for IDT-1 of the 40 MHz and 80 MHz IDT designs, the power application was limited. For IDT-1 of the 40 MHz IDT design and flow rates between 500 and 2500  $\mu L/h$ , the maximum power that could be applied was 2370 mW, while IDT-2 reached the desired value of 2500 mW. This also occurred for IDT-1 of the 80 MHz IDT design, where the maximum power was 2340 mW and 2500 mW for IDT-2. It is unknown why the power input of IDT-1 is limited to 2370 mW and 2340 mW for the 40 MHz and 80 MHz IDT design, respectively.

For the 120 MHz IDT design, the power applied to the system did not function as expected. High resistance occurred between the SAW generator and IDT-1, which could potentially be a result of bad connections between the SAW generator and the IDT-1. Additionally, power limitations could be seen for IDT-2 of the 120 MHz IDT design. At a flow rate of  $500 \mu\text{L}/\text{h}$ , the maximum power input to the system was 1800 mW, whereas the power input reached 1850 mW for flow rates of  $1000 \mu\text{L}/\text{h}$  and  $1500 \mu\text{L}/\text{h}$ .

**Occurrence of bubbles:** Bubbles in the microchannel are not desirable due to the possibility of altering the flow or blocking the microchannel. For several cases during the experiments, bubbles occurred. This occurred especially for the 40 MHz IDT design owing to leakages and fast power applications during the microfluidic mixing experiments.

Bubble generation is illustrated in Figure 4.4. The development of bubbles can be a consequence of heat generation in the microfluidic channel and weak bonding of the assembly. Heating of the assembly is generated as a result of the energy input of the SAW generator. The energy has to dissipate to obtain fluid and particle motion, i.e. mixing. Without sufficient heat transfer or cooling of the assembly, a rise in the temperature may produce gas bubbles. Bubbles can also be generated through small cavities, where there are weak bonds (uncompleted cross-linking) between the microchannel and the IDTs.

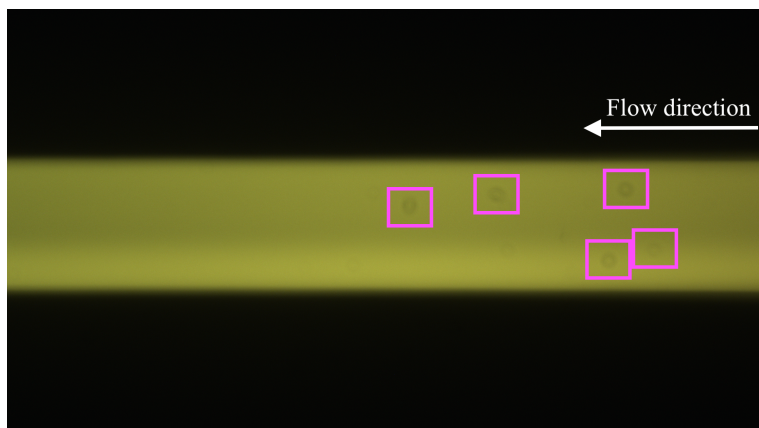


**Figure 4.4:** Bubble occurrence inside the microchannel.

**Leakage:** As explained in Subsection 3.2.4, the assembly of the microchannel and the IDTs is a sensitive process. Complete information about the integrity of the assembly is not obtained before testing. Unsatisfactory cross-linking creates weak bonds between the two elements, causing leakages. The leakages normally occur around the two inlets and the outlet of the microchannel.

Leakages occurred for the 40 MHz IDT design. Fast and incomplete experiments were performed to obtain as much information about the mixing in the microchannel as possible before the leakages could damage the microscope. These fast experiments can have affected the quality of the measurements, where bubbles can be seen for both different

flow rates and power applications.

**Microchannel alignment:** The alignment of the microchannel and the IDTs can affect the mixing performance of the microfluidic device. Table 4.3 shows the distance between the microchannel and the IDT. The differences in the alignment could make uncertainties and errors when comparing the obtained results in Chapter 5 and should be taken into consideration.

**Table 4.3:** Distance between the microchannel and the interdigital transducers for the different IDT designs.

IDT design [MHz]	Distance [mm]	
	IDT-1	IDT-2
40	0.8	0.8875
80	0.625	0.65
120		0.775

## 4.4 Summary

This chapter has presented the experimental campaign for microfluidic mixing using surface acoustic waves and for spectroscopy analysis of nanoplasmonic sensors. For the microfluidic mixing, the mixing efficiency has been investigated for a total of three IDT designs with frequencies of 40, 80, and 120 MHz, flow rates ranging from 500 to 4000  $\mu\text{L}/\text{h}$ , and power inputs between 0 and 2500 mW. The experimental campaign for the nanoplasmonic sensors entails sensor parameters including square or hexagonal nanohole arrays, constant 400 nm diameter nanoholes, gold layer thicknesses between 200 and 250 nm, and periodicities ranging from 700 to 1100 nm. The NTNU acoustofluidics test facility has been described in detail and the objectives for the experimental campaign have been presented. The microfluidic mixing and the nanoplasmonic sensor test procedures, data processing, and experimental uncertainties have also been described.

## Results and Discussion

The conducted test campaign presented in the previous chapter served to enhance the understanding of microfluidic mixing operations by incorporating acoustofluidics and nanoplasmonic sensor experiments. The results obtained from the experimental test campaign will be presented and discussed in the following chapter.

This chapter will be divided into two parts:

1. Microfluidic mixing performance
2. Nanoplasmonic sensor performance

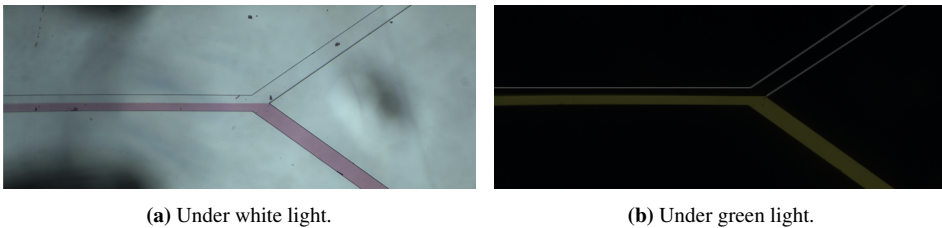
### 5.1 Microfluidic Mixing Performance

The following section will present the microfluidic mixing performance for three different IDT mixer designs with frequencies of 40 MHz, 80 MHz, and 120 MHz. The mixing efficiency for each IDT design will be plotted against the flow rate and power input before the efficiencies for the IDT designs are compared. For all the cases, mixing is not dominated by diffusion owing to flow rates of  $500 \mu\text{L}/\text{h}$  and higher, giving Péclet numbers above 1000 explained by Equation 2.19. The numerical values for the mixing efficiencies of the 40 MHz, 80 MHz, and 120 MHz IDT designs can be found in Appendix F.

As mentioned in Subsection 4.3.4, IDT-1 for both the 40 MHz and 80 MHz IDT design has power limitation at 2370 mW and 2340 mW, respectively. IDT-2 of the 120 MHz IDT design also experienced power limitations. The maximum power input was 1800 mW for a flow rate of  $500 \mu\text{L}/\text{h}$  and 1850 mW for flow rates of  $1000 \mu\text{L}/\text{h}$  and  $1500 \mu\text{L}/\text{h}$ . These

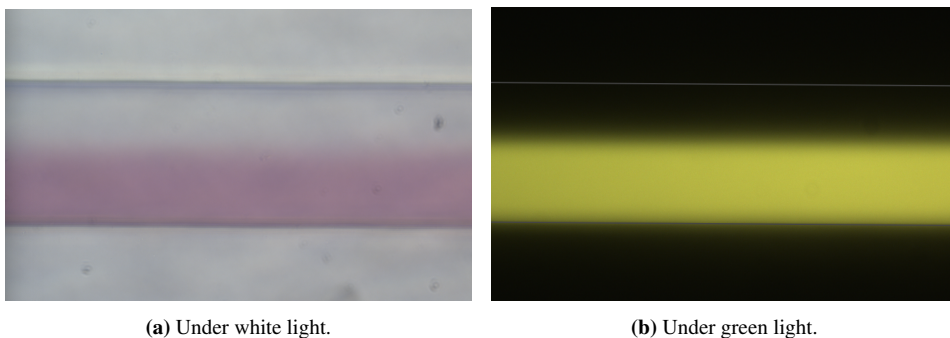
limitations can affect the obtained mixing performance and create additional uncertainties to the results in this work.

Figure 5.1 presents the Y-shaped microfluidic device without the presence of SAWs. One of the inlets is filled with DI water and the other with a mixture of DI water and 0.25% sulforhodamine B. The sulforhodamine B gives a pink color under white light as seen in Figure 5.1a and a green color under green light in Figure 5.1b. It can be seen that the flow inside the microchannel is completely laminar for no power applications.



**Figure 5.1:** The Y-shaped microchannel inlet showing a 50/50 fluid flow with DI water and a mixture of DI water and 0.25% sulforhodamine B under white and green light.

Figure 5.2 shows the microchannel reference for the initial non-mixed state, i.e. without SAW generation, under white and green light. Similar to Figure 5.1, the flow is completely laminar without any fluorescent particles flowing across the visual interface.



**Figure 5.2:** Part of the microchannel for the non-mixed state under white and green light.

The three different IDT designs utilized in the conducted experiments can be seen in Figure 5.3. A reduction in the IDT features is seen for higher frequency IDTs, explained by Equation 2.21. The IDTs have equal finger width and spacing of  $25\ \mu\text{m}$ ,  $12.5\ \mu\text{m}$ , and  $8.6\ \mu\text{m}$  for the 40 MHz, 80 MHz, and 120 MHz IDT designs. They are fabricated on a  $128^\circ$  Y-rotated X-propagating  $\text{LiNbO}_3$  substrate and created by an 80 nm thick gold layer.

The obtained experimental results for IDT-1 and IDT-2 for the 40 MHz and 80 MHz IDT designs yield different mixing efficiencies under similar operating conditions. It is unknown why there is a difference in the obtained mixing performance. It may be attributed

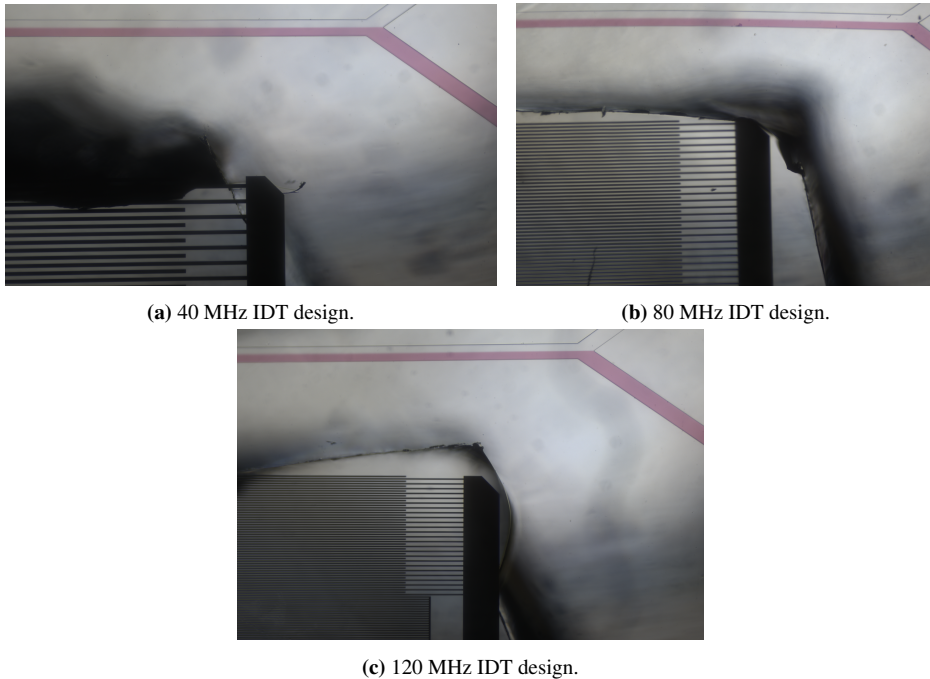


**Figure 5.3:** Visualization of the 40 MHz, 80 MHz, and 120 MHz IDT designs and the microchannel without any power inputs under white light.

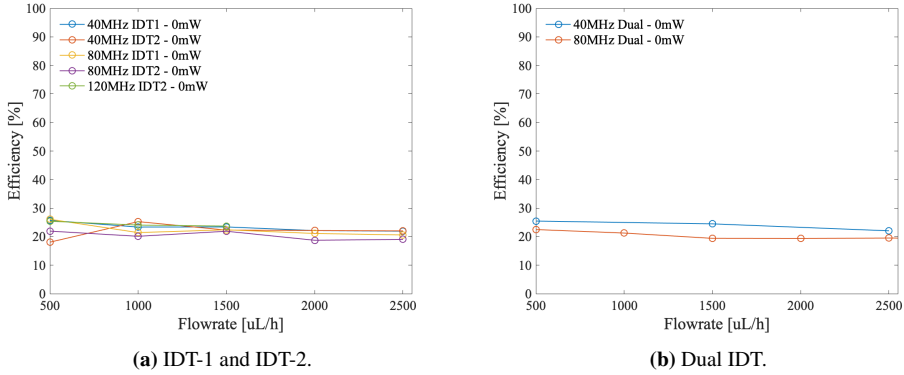
to an inaccurate alignment of the microchannel between the two IDTs, resulting in a difference in the distance between the IDT and the microchannel, as mentioned in Subsection 4.3.4. It may also be a consequence of different resistance between the IDT and the SAW generator for each IDT. Nevertheless, this should be further investigated.

Figure 5.4 displays the mixing efficiencies at different flow rates for the single and dual IDT for the 40 MHz, 80 MHz, and 120 MHz IDT designs with no power input. It functions as a reference to indicate the effect of the different IDTs on the microfluidic mixing. They are not considered in the plots in the following sections as they should be equal in theory. However, the values slightly differ, which could be an effect of measurement uncertainties. It could also be a result of uncertainties in the internal diameter of the microchannel that could cause an internal difference in the fluid velocity.

### 5.1.1 40 MHz IDT Performance

Figure 5.5 displays the mixing efficiency for IDT-1 of the 40 MHz IDT design. The mixing performance is considered at fixed flow rates and power inputs, represented in Figure 5.5a and 5.5b, respectively. From Figure 5.5a, it can be seen that the lower flow rates reach





**Figure 5.4:** Comparison of the mixing efficiencies for IDT-1, IDT-2, and dual IDT of the 40 MHz, 80 MHz, and 120 MHz IDT designs with no power input (0 mW).

complete mixing faster than for higher flow rates. These results coincide well with the numerical observations by Termizi & Shukor [220], where the inlet velocity had significant effects on the mixing performance. They observed that for higher inlet velocities, the mixing quality became lower. Jo & Guldiken [152], Ahmed et al. [217] and Nam & Lim [171] obtained similar results experimentally. The reduction in the mixing efficiency for higher flow rates can be explained by the fluid streams being exposed to the SAWs for a shorter time period, thus reducing the effect of the SAWs on the fluid streams. Figure 5.5b also indicates that higher power applications induce better mixing performance as a result of the higher SAW amplitude, which corresponds to the findings by a number of reviews [150, 152, 217].

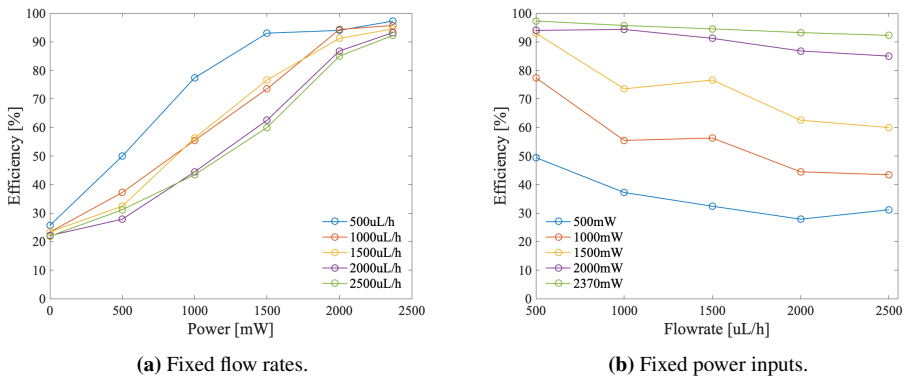


**Figure 5.5:** Mixing efficiency for IDT-1 of the 40 MHz IDT design at fixed flow rates and power applications.

Figure 5.6 presents the mixing performance for IDT-2. Similar to the 40 MHz IDT-1, the lower flow rates induce faster mixing. It can be seen from Figure 5.6a that for 500 and 1000  $\mu\text{L}/\text{h}$ , complete mixing is achieved at 1500 mW, while it is reached at 2500 mW for 1500, 2000, and 2500  $\mu\text{L}/\text{h}$ . The higher flow rates yield lower mixing efficiencies than the obtained values for lower flow rates, where 95.87% mixing is achieved for a flow rate of 500  $\mu\text{L}/\text{h}$ , 94.63% at 1000  $\mu\text{L}/\text{h}$ , 93.01% at 1500  $\mu\text{L}/\text{h}$ , 89.70% at 2000  $\mu\text{L}/\text{h}$ , and 88.33% at 2500  $\mu\text{L}/\text{h}$ . An explanation could be that the fluid streams are less affected by the SAWs for higher flow rates. For higher flow rates, the fluid streams will be in the region of interest for a shorter time period than for lower flow rates, which results in a shorter time interval where the fluid streams absorb the acoustic energy from the SAWs. The tendency of increased mixing efficiency for higher power applications is visible in Figure 5.6b. An apparent reduction can be seen for 500 mW and 1000 mW at low flow rates (500 and 1000  $\mu\text{L}/\text{h}$ ) compared to higher power inputs, which could be an effect of a lower SAW amplitude. The obtained mixing efficiencies at 500  $\mu\text{L}/\text{h}$  are 60.76%, 79.49%, 95.44%, 94.55%, and 95.87% for 500 mW, 1000 mW, 1500 mW, 2000 mW, and 2500 mW respectively.

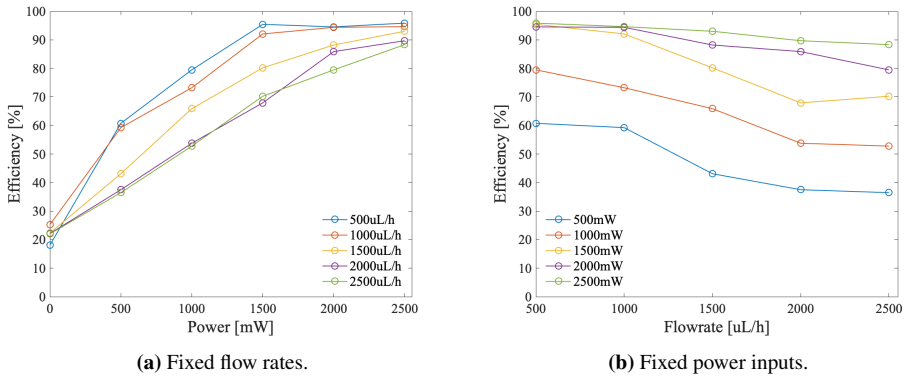


**Figure 5.6:** Mixing efficiency for IDT-2 of the 40 MHz IDT design at fixed flow rates and power applications.

The mixing efficiency for the dual IDT of the 40 MHz IDT design is shown in Figure 5.7. As mentioned in Subsection 4.3.4, the experiments for the 40 MHz IDT design were conducted fast and inconsistent to obtain as much information as possible about the microfluidic mixing owing to leakage between the IDT and the microchannel. Despite the incomplete results for the dual IDT, the measured mixing points give an indication of its mixing efficiency. It can be seen that the microfluidic mixing with dual IDT follows the same tendency as for the single IDT. Accordingly, low flow rates induce faster mixing as seen in Figure 5.7a, while higher power applications reach better mixing efficiency, which can be observed in Figure 5.7b.

In Figure 5.8, the mixing performance for IDT-1, IDT-2, and dual IDT is compared for the 40 MHz IDT design at both fixed flow rates and fixed powers. A clear enhancement in the mixing efficiency can be seen for the dual IDT compared to the single IDTs. The

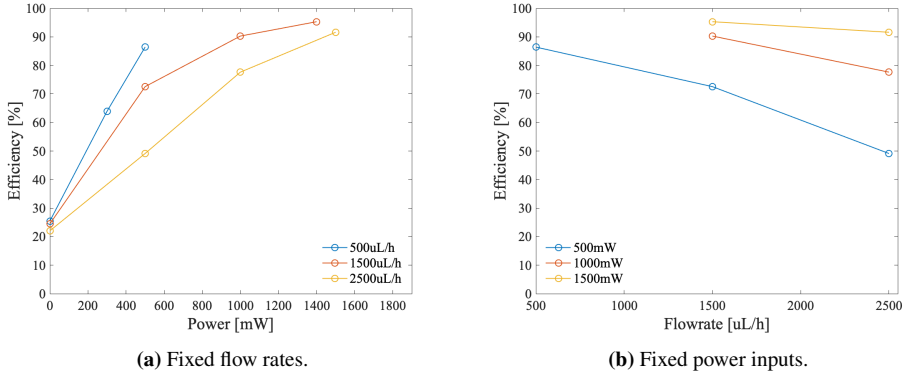


**Figure 5.7:** Mixing efficiency for the dual IDT of the 40 MHz IDT design at fixed flow rates and power applications.

dual IDT mixing efficiency is highly increased and reaches  $\sim 90\%$  at 1000 mW and  $\sim 95\%$  at 1500 mW for a flow rate of  $1500 \mu\text{L}/\text{h}$  as shown in Figure 5.8a. On the other hand, the obtained mixing efficiencies at the same power inputs for IDT-1 and IDT-2 are only  $56.30\%$  and  $65.89\%$  at 1000 mW and  $76.62\%$  and  $80.20\%$  at 1500 mW, respectively. Thus, the required power application to achieve complete mixing is much lower for the dual IDT than for the single IDT. This may be linked to a larger absorbed acoustic energy by the fluids for a dual IDT than for a single IDT due to the generation of SAW by both IDTs. For the single IDTs, IDT-2 yields higher mixing efficiency up to 1500 mW. For 2000 mW and 2500 mW, IDT-1 obtains a higher mixing performance. This also accounts for flow rates of 500 and 2500  $\mu\text{L}/\text{h}$ , which can be seen in Figure F.1 and F.2 in Appendix F.

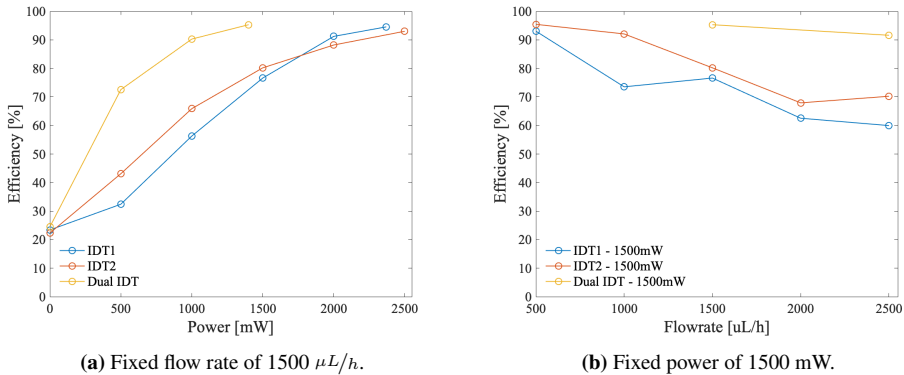


**Figure 5.8:** Comparison of the mixing efficiencies for IDT-1, IDT-2, and dual IDT of the 40 MHz IDT design at a fixed flow rate of  $1500 \mu\text{L}/\text{h}$  and fixed power of 1500 mW.

### 5.1.2 80 MHz IDT Performance

The mixing performance for IDT-1 of the 80 MHz IDT design is presented in Figure 5.9. Low flow rates with high power applications yield both the fastest mixing and highest mixing efficiency. Thus, the trend for the 40 MHz IDT design is also valid for IDT-1 of the 80 MHz IDT design.

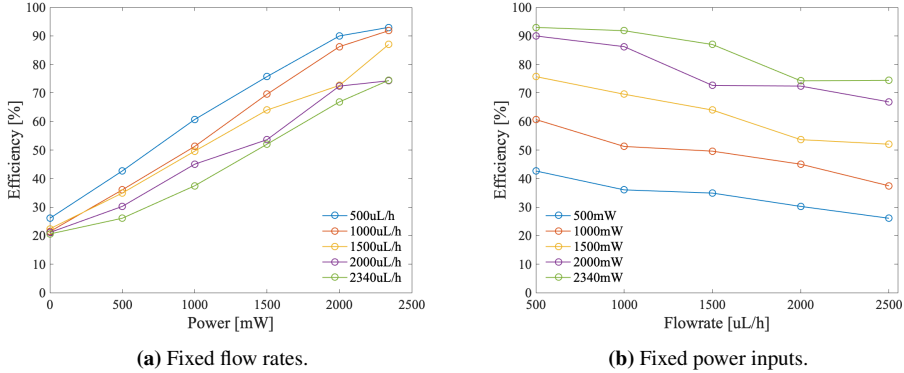


**Figure 5.9:** Mixing efficiency for IDT-1 of the 80 MHz IDT design at fixed flow rates and power applications.

Figure 5.10 shows the mixing performance for IDT-2 of the 80 MHz IDT design. It can be observed that the microfluidic mixing follows the same tendency as for the 40 MHz IDT design and IDT-1 of the 80 MHz IDT design. An increase in the applied power leads to higher mixing efficiencies, whereas higher flow rates decrease the mixing quality due to the shorter time period where the fluid streams are affected by the SAWs. The obtained mixing efficiencies at 2500 mW are 97.91%, 97.16%, 94.03%, 86.78%, and 84.78% for flow rates of 500, 1000, 1500, 2000, and 2500  $\mu\text{L}/\text{h}$ , respectively.

In Figure 5.11, the mixing performance for the dual IDT is presented. The obtained results concur well with findings in the literature [150, 152, 171, 217, 220] and follow the trend for induced mixing and efficiency observed for the 40 MHz single and dual IDT and 80 MHz single IDT. Complete mixing is achieved at 1000 mW for 500 and 1000  $\mu\text{L}/\text{h}$ , at 1500 mW for 1500–2500  $\mu\text{L}/\text{h}$ , and at 2000 mW for 3000 and 4000  $\mu\text{L}/\text{h}$ . As explained previously, higher flow rates require higher power inputs to achieve complete mixing due to lower acoustic energy absorption of the SAW for faster fluid streams. From Figure 5.11b it can be seen that as the flow rate is increased, the mixing efficiency decreases, especially for 500 and 1000 mW. This can be related to a lower SAW amplitude for lower power inputs than for higher power applications.

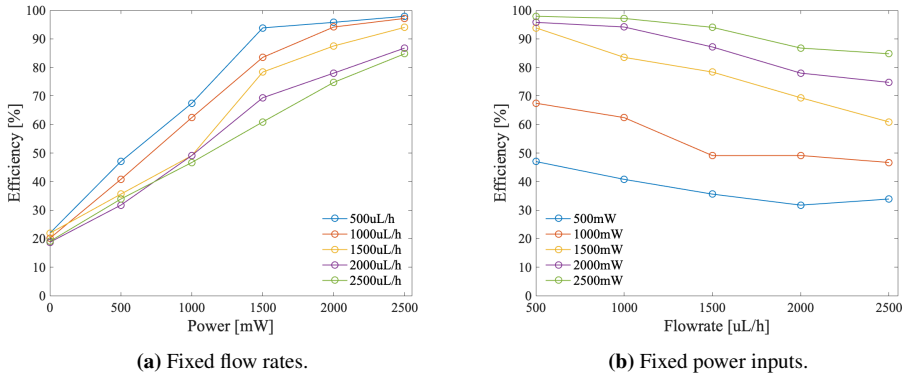


**Figure 5.10:** Mixing efficiency for IDT-2 of the 80 MHz IDT design at fixed flow rates and power applications.

The dual IDT was not tested for 2000 mW for flow rates between 500 and 2000  $\mu\text{L}/\text{h}$  owing to visual confirmation of complete mixing for lower power applications. However, it can be seen that for the higher flow rates (2500-4000  $\mu\text{L}/\text{h}$ ), the mixing efficiency for the 2000 mW is higher than for the lower power applications. Thus, it may be assumed that the mixing efficiency curve with fixed power at 2000 mW for flow rates between 500 and 2000  $\mu\text{L}/\text{h}$  is equal to or slightly better than the obtained results for 1500 mW. This assumption is based on the findings where higher power applications generally result in higher mixing efficiencies.

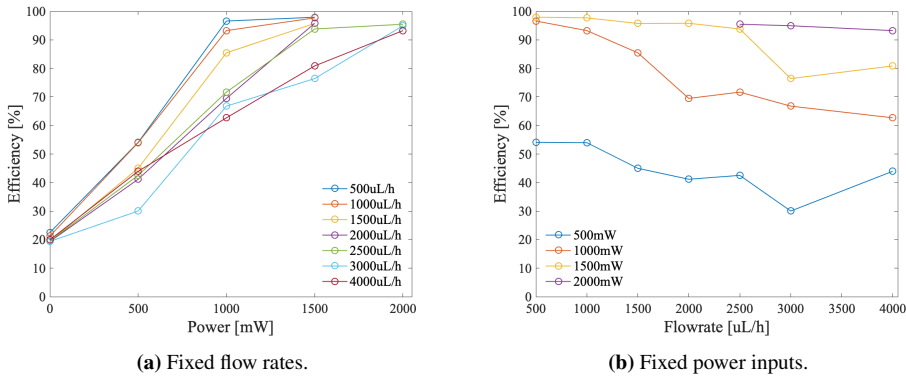


**Figure 5.11:** Mixing efficiency for the dual IDT of the 80 MHz IDT design at fixed flow rates and power applications.

Figure 5.12 displays a comparison of the mixing efficiencies for IDT-1, IDT-2, and dual IDT for the 80 MHz IDT design at fixed flow rates and power applications. It is clear from both Figure 5.12a and 5.12b that the mixing is increased by utilizing two IDTs instead of a single IDT. Thus, the minimum required power input to achieve complete mixing for the

dual IDT is lower than for IDT-1 and IDT-2. As mentioned in Subsection 5.1.1, this is a result of a larger quantity of the acoustic energy being absorbed by the fluids. It can also be observed that IDT-2 reaches complete mixing faster than IDT-1. This is an ongoing trend for flow rates between 500 and 2500  $\mu\text{L}/\text{h}$ . This may be related to measurement uncertainties, inaccurate alignment between the IDT and the microchannel, or imprecise microchannel dimensions, as previously mentioned in Subsection 4.3.4 and Section 5.1. This can be seen in Figure F.6-F.8 in Appendix F.

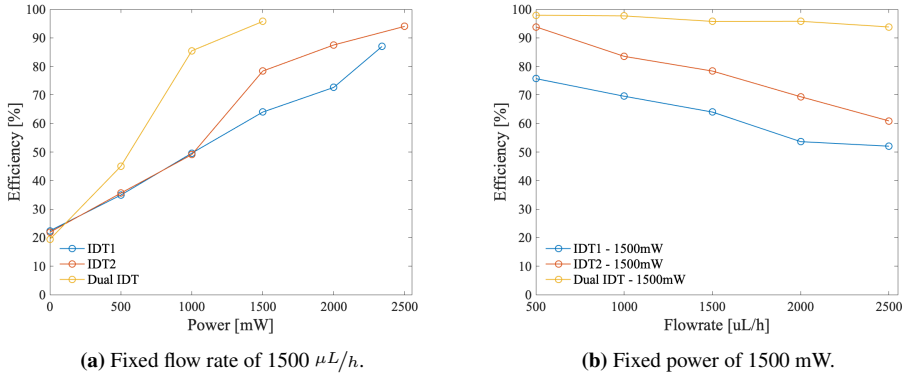


**Figure 5.12:** Comparison of the mixing efficiencies for IDT-1, IDT-2, and dual IDT of the 80 MHz IDT design at a fixed flow rate of 1500  $\mu\text{L}/\text{h}$  and fixed power of 1500 mW.

### 5.1.3 120 MHz IDT Performance

Figure 5.13 shows the mixing efficiency for IDT-2 of the 120 MHz IDT design. A pronounced reduction in the mixing efficiency can be seen for lower power inputs and higher flow rates. This corresponds well with the tendency observed for both the 40 MHz and 80 MHz IDT designs. The highest obtained mixing efficiency is 87.52% with a flow rate of 500  $\mu\text{L}/\text{h}$  flow rate and applied power of 1800 mW.

Only IDT-2 was tested owing to the occurrence of high resistance between the SAW generator and the IDT-1 when applying power. A new sample could be made in order to obtain results for the 120 MHz IDT-1 and dual IDT, but due to COVID-19 and lockdown at the NTNU acoustofluidics test facility and Nanolab, both the fabrication and test period were severely reduced. In the available time frame, this was not achievable.

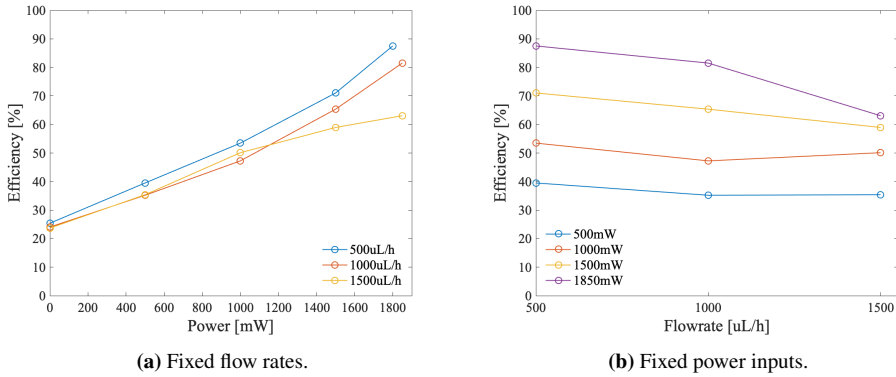


**Figure 5.13:** Mixing efficiency for IDT-2 of the 120 MHz IDT design at fixed flow rates and power applications.

### 5.1.4 Comparison of the Mixing Performance for the IDT Designs

#### Comparison of the mixing efficiencies for IDT-2 of the 40 MHz, 80 MHz, and 120 MHz IDT design

Figure 5.14 displays the comparison of the mixing efficiencies for IDT-2 for each IDT design with a fixed power of 1500 mW. The mixing efficiency is seen to be greater for the 40 MHz and 80 MHz IDT designs for all flow rates compared to the 120 MHz IDT design. From the literature and Equation 2.20, a higher frequency IDT is assumed to yield a lower mixing efficiency due to a reduction in the attenuating length of the SAW into the fluids. As a consequence, the fluids will absorb less acoustic energy owing to the shorter decay length and faster dissipation of the acoustic energy from the SAW. This trend is valid for the 120 MHz IDT design, however, the mixing performance for the 40 MHz and 80 MHz IDT designs does not provide large differences. It is unknown why the results differ from the literature.

Power limitations for the IDT-2 of the 120 MHz IDT design were found during the experiments as previously mentioned in this section. Additionally, the IDT-2 was only tested for flow rates between 500 and 1500  $\mu\text{L}/\text{h}$ . This was a result of small visible changes in the fluids streams when higher power inputs were applied during the experiments, especially for the flow rates of 1000  $\mu\text{L}/\text{h}$  and 1500  $\mu\text{L}/\text{h}$ . Although the 120 MHz IDT design results are not considered for flow rates of 2000 and 2500  $\mu\text{L}/\text{h}$ , the measured points provide insight into the mixing efficiency of the 120 MHz IDT design compared to the obtained performances of the 40 MHz and 80 MHz IDT designs.

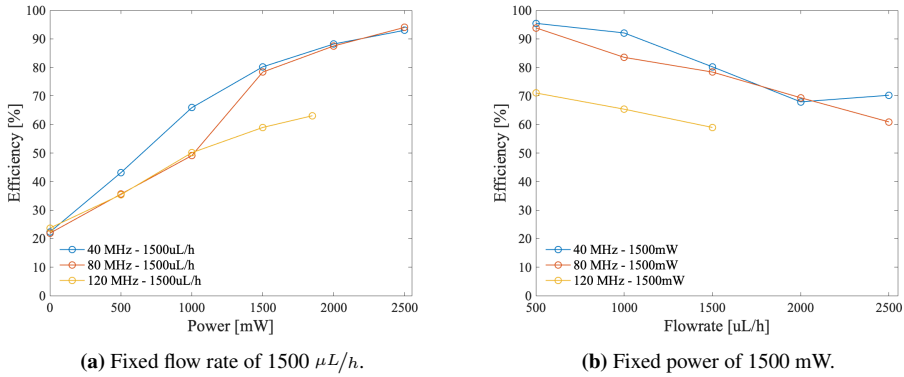


**Figure 5.14:** Comparison of the mixing efficiencies for IDT-2 of the 40 MHz, 80 MHz, and 120 MHz IDT designs at a fixed flow rate of 1500  $\mu\text{L}/\text{h}$  and fixed power of 1500 mW.

### Comparison of the mixing efficiencies for the 40 MHz and 80 MHz IDT design

The mixing efficiencies for the IDT-1 and IDT-2 of the 40 MHz and 80 MHz IDT designs are presented in Figure 5.15. It is clear from Figure 5.15 that the 80 MHz IDT-1 yields the lowest mixing efficiency for the single IDTs under similar operating conditions. The 40 MHz IDT-2 obtains the highest mixing performance for lower power applications (500-1500 mW), while for 2000-2500 mW the 80 MHz IDT-2 yields the highest efficiency.

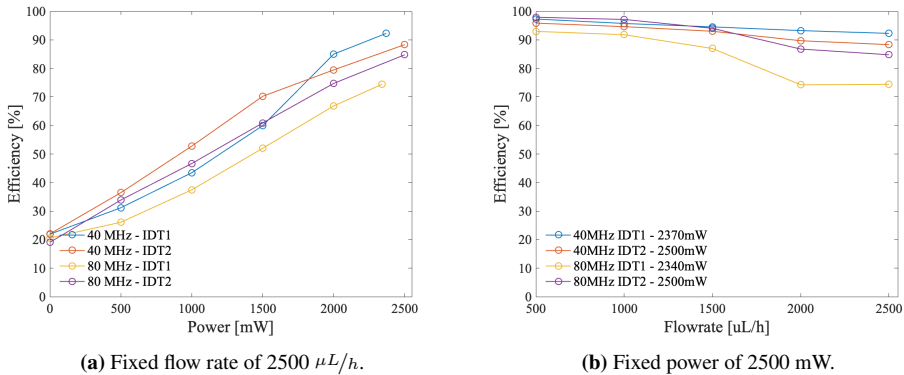


**Figure 5.15:** Comparison of the mixing efficiencies for IDT-1 and IDT-2 of the 40 MHz and 80 MHz IDT designs at a fixed flow rate of 2500  $\mu\text{L}/\text{h}$  and fixed power of 2500 mW.

As previously mentioned, the small difference in the mixing efficiency results between the 40 MHz and 80 MHz IDT designs is contradictory to the expected results found in the literature. The 40 MHz IDT design was anticipated to yield higher mixing efficiencies and faster mixing than the 80 MHz IDT design. This could be explained by Equation 2.20 and the longer attenuation length of the SAW into the fluid streams for higher frequency IDTs.



The same trend can also be seen for lower flow rates in Figure F.12-F.15 in Appendix F. Additional experiments and investigations should be conducted to explain the differences in the obtained mixing performance with the results found in the literature. The small difference in the mixing performance of the IDT designs and the specific IDT may be explained by the difference in the microchannel position related to the IDT, which may cause a dissimilar energy distribution from the SAW, or as a result of a difference in the resistance between the IDT and the SAW generator.

The same effect can be seen for the mixing efficiency curves for the dual IDT in Figure 5.16 and Figure F.16-F.18 in Appendix F, where the 40 MHz and 80 MHz IDT designs achieve similar mixing performances. The dual IDTs yield mixing efficiencies with values of 95.31% and 91.61% for the 40 MHz IDT design and 95.76% and 93.82% for the 80 MHz IDT design for flow rates of 1500 and 2500  $\mu\text{L}/\text{h}$  with a power input of 1500 mW, respectively.

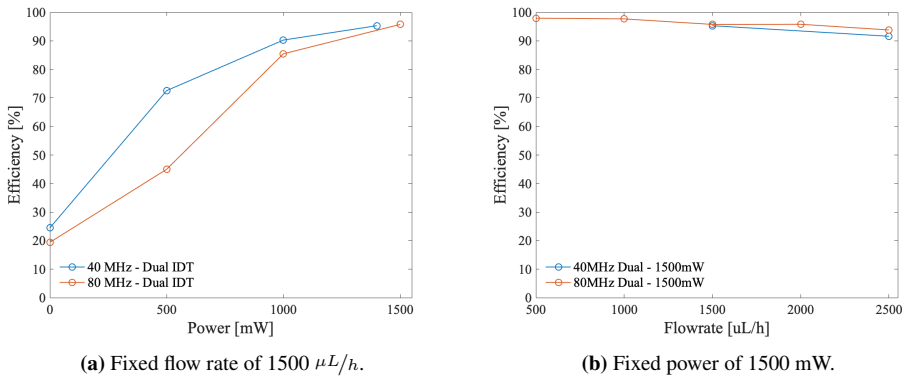
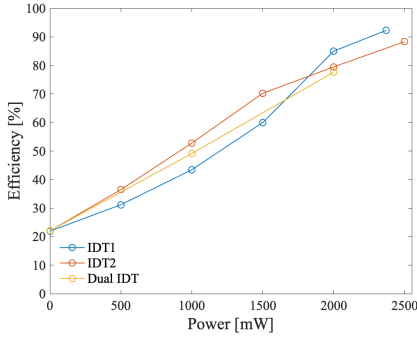


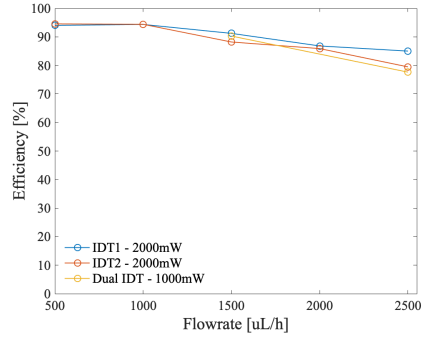
**Figure 5.16:** Comparison of the mixing efficiencies for the dual IDT for the 40 MHz and 80 MHz IDT designs at a fixed flow rate of 1500  $\mu\text{L}/\text{h}$  and fixed power of 1500 mW.

As mentioned in Subsection 2.7.3, only a few studies in the literature [152, 171, 201] have investigated and compared the mixing efficiencies for a single and dual IDT design. The comparison method for these reviews is not specified, but there is reason to believe that they have examined the mixing efficiencies for the single and dual IDT design at equal power inputs (e.g. input of 500 mW for the single and dual IDT). The obtained test results presented in this section concur well with these findings. However, considering that each IDT receives power from the SAW generator for the dual IDT, the total amount of power applied into the system is doubled as opposed to a single IDT. Thus, the energy put into the system to mix the two fluids is not identical. When comparing the mixing efficiency for equal power applications for the single and dual IDT designs (e.g. input of 1000 mW for single IDT and input of 500 mW for dual IDT), no significant difference in the mixing performance can be seen for all flow rates and power applications. This can also be observed in Figure 5.17-5.19 and Figure F.19-F.25 in Appendix F.

## 5.1 Microfluidic Mixing Performance

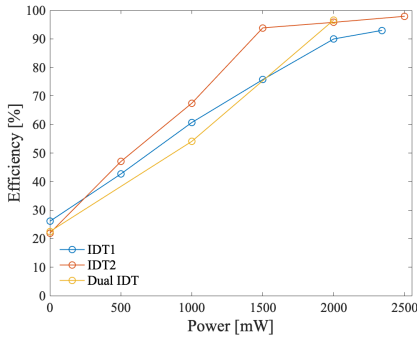


(a) Fixed flow rate of  $2500 \mu\text{L}/\text{h}$ .

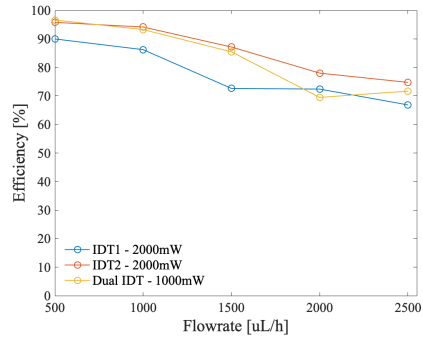


(b) Fixed power of 2000 mW for the single IDTs and 1000 mW for the dual IDT.

**Figure 5.17:** Comparison of the mixing efficiencies for IDT-1, IDT-2, and dual IDT of the 40 MHz IDT design at a fixed flow rate of  $2500 \mu\text{L}/\text{h}$  and fixed power of 2000 mW for the single IDTs and 1000 mW for the dual IDT.

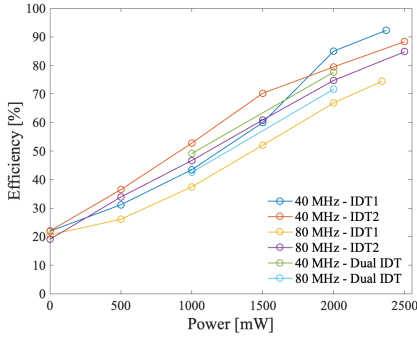


(a) Fixed flow rate of  $500 \mu\text{L}/\text{h}$ .

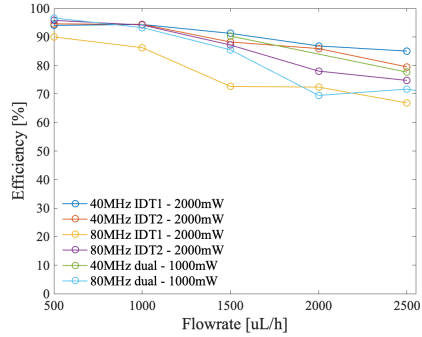


(b) Fixed power of 2000 mW for the single IDTs and 1000 mW for the dual IDT.

**Figure 5.18:** Comparison of the mixing efficiencies for IDT-1, IDT-2, and dual IDT of the 80 MHz IDT design at a fixed flow rate of  $500 \mu\text{L}/\text{h}$  and fixed power of 2000 mW for the single IDTs and 1000 mW for the dual IDT.



(a) Fixed flow rate of  $2500 \mu\text{L}/\text{h}$ .



(b) Fixed power of 2000 mW for the single IDTs and 1000 mW for the dual IDT.

**Figure 5.19:** Comparison of the mixing efficiencies for IDT-1, IDT-2, and dual IDT of the 40 MHz and 80 MHz IDT designs at a fixed flow rate of  $2500 \mu\text{L}/\text{h}$  and fixed power of 2000 mW for the single IDTs and 1000 mW for the dual IDT.

## 5.2 Nanoplasmonic Sensor Performance

In the following section, the nanoplasmonic sensor sensitivity performance will be presented. The effects of the polynomial order of the regression curve and the gold layer thickness on the sensitivity performance are discussed. Further, the sensor sensitivity for both square and hexagonal nanohole arrays are presented and later compared. The maximum obtained sensitivity from the experiments is compared to sensitivities reported in the literature.

### 5.2.1 Effect of the Polynomial Order on the Sensitivity Performance

As explained in Subsection 4.3.4, the nanoplasmonic sensor sensitivity is dependent on the wavelength shift of the spectrum peaks as well as the utilized polynomial curve fitting order. Figure 5.20 and 5.21 show the polynomial curve fitting of the obtained experimental spectra and their calibration curve, respectively, for a hexagonal nanohole array with a nanohole diameter of 400 nm, 250 nm gold layer thickness, and 1000 nm periodicity with the polynomial orders  $P=15$ ,  $P=25$ , and  $P=50$ . Additionally, Table 5.1 presents how the resonance wavelength peak position and sensitivity are affected by the polynomial order.

## 5.2 Nanoplasmonic Sensor Performance

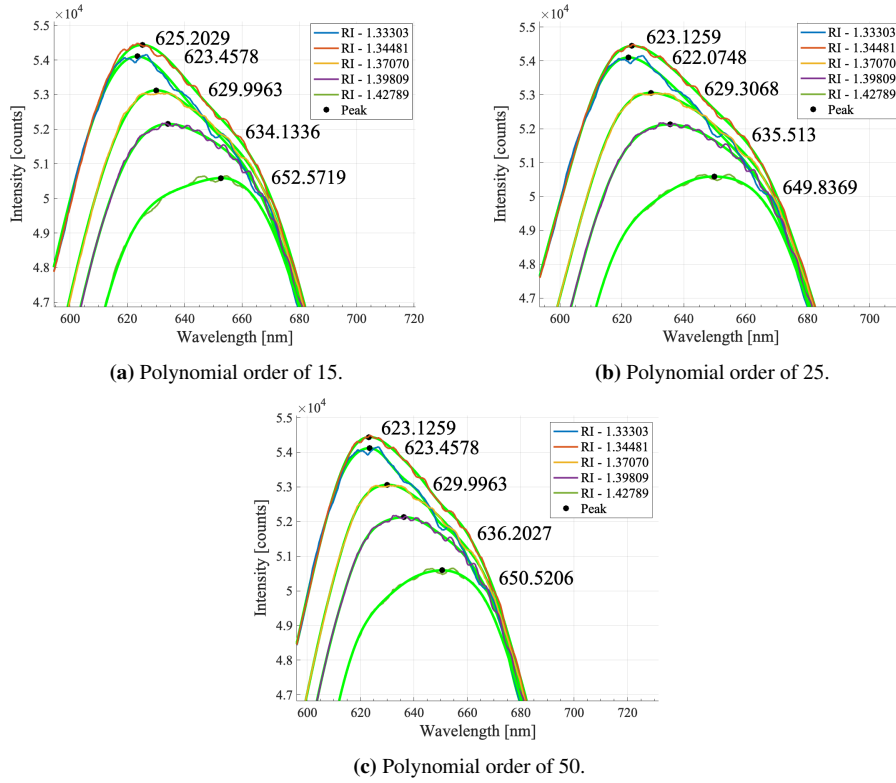


**Figure 5.20:** Representation of the equivalence between the obtained experimental spectra for a hexagonal nanohole array with a nanohole diameter of 400 nm, 250 nm gold layer thickness, and 1000 nm periodicity and the polynomial curve fitting for polynomial orders of 15, 25 and 50. The green curves indicate the fitted curves.

**Table 5.1:** Effect of the polynomial curve fitting order on the sensitivity and resonance wavelength peak for a hexagonal nanohole array with nanohole diameters of 400 nm, 250 nm gold layer thickness, and 1000 nm periodicity.

Polynomial order	Resonance peak wavelength [nm]					Sensitivity [nm/RIU]
	RI = 1.33303	RI = 1.34481	RI = 1.37070	RI = 1.39809	RI = 1.42789	
P = 15	625.2029	623.4578	629.9963	634.1336	652.5719	297.4163
P = 25	623.1259	622.0748	629.3068	635.5130	649.8369	283.6045
P = 50	623.1259	623.4578	629.9963	636.2027	650.5206	276.4618

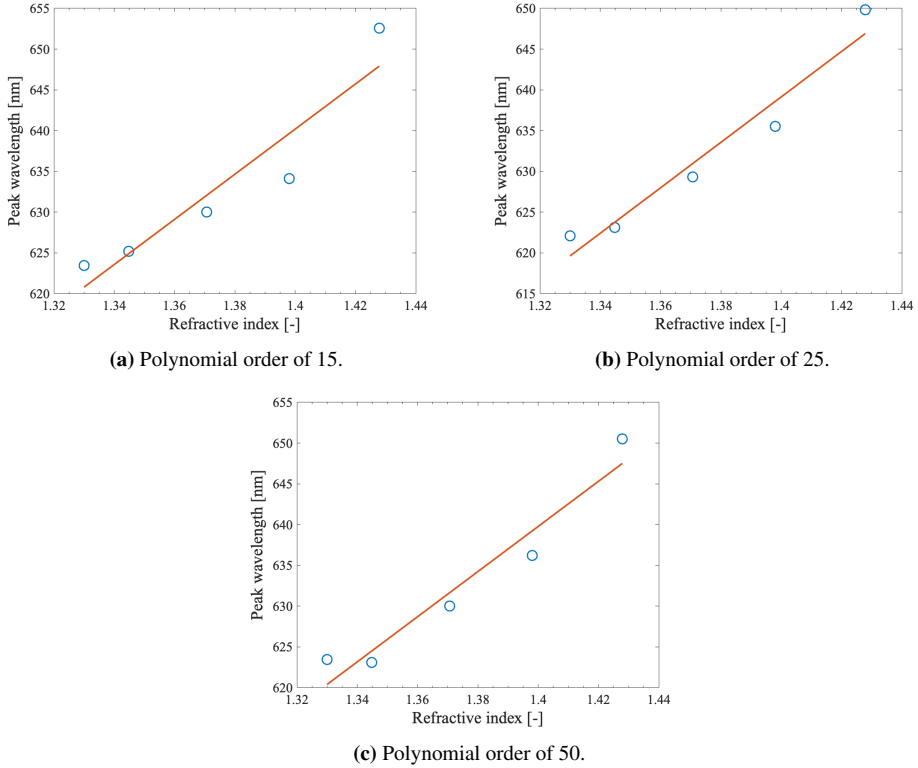


**Figure 5.21:** Refractive index plotted against the resonance wavelength peak from the polynomial curve fitting for polynomial orders of 15, 25, and 50 for a sensor with a hexagonal nanohole array, a nanohole diameter of 400 nm, 250 nm gold layer thickness, and 1000 nm periodicity.

Table 5.2 displays the sensitivity of the different polynomial orders for various sensor parameters. A clear variation in the sensitivity can be observed for the three polynomial orders as a consequence of the different wavelength peaks acquired from the curve fittings. Thus, a mean sensitivity has been computed from the three obtained sensitivity values for the different polynomial orders. The variance presented in Table 5.2 is calculated from the difference in the wavelength peak positions between the measured points and the values obtained from the polynomial curve fitting for their respective refractive indices. The table also presents two cases with identical parameters; a sensor with a hexagonal nanohole array, nanohole diameters of 400 nm, 250 nm gold layer thickness, and 800 nm periodicity. However, the obtained mean sensitivities are dissimilar with values of 126.4714 nm/RIU and 118.2178 nm/RIU. The difference can be a result of measurement uncertainties, environmental fluctuations, different resonance wavelength peak positions due to the polynomial curve fittings, or a combination of them. To conclude on the main factors behind the differences, additional investigations and tests should be performed.

**Table 5.2:** Dimensions and experimental results for the different nanoplasmonic sensors.

Sensor parameters				Sensitivity [nm/RIU]			Variance			Mean sensitivity [nm/RIU]
Lattice	nm gold	nm diameter	nm pitch	P = 15	P = 25	P = 50	P = 15	P = 25	P = 50	
Square	250	400	700	35.3478	28.2783	21.2087	0.0729	0.0608	0.0738	28.2783
Hexagonal	250	400	700	101.3902	178.7161	185.7299	0.1175	1.8051	2.4240	155.2787
Square	250	400	800	27.8765	49.1064	49.0852	0.0783	0.2359	0.5675	42.0227
Hexagonal	250	400	800	70.1730	161.6886	147.5528	0.4623	1.8609	2.8373	126.4715
Square	250	400	900	67.0813	74.1331	45.9044	0.1255	0.0492	0.3674	62.3729
Hexagonal	250	400	900	118.9524	161.2150	132.9132	0.2617	0.9896	0.7041	137.6935
Square	250	400	1000	158.4636	186.6121	158.3598	0.4397	1.0166	0.5122	167.8118
Hexagonal	250	400	1000	297.4163	283.6043	276.4618	4.3576	1.0323	0.7088	285.8275
Square	250	400	1100	217.6206	189.2859	168.0772	0.7705	0.4105	0.5967	191.6612
Hexagonal	250	400	1100	45.7978	59.9578	59.9578	0.1202	0.1287	0.0503	55.2378
Square	200	400	700	17.7351	17.7341	17.7351	0.0191	0.0192	0.0829	17.7348
Square	200	400	800	49.6042	42.5179	49.6042	0.0083	0.0395	0.2074	47.2421
Square	200	400	900	24.7329	17.6466	17.6466	0.0421	0.0258	0.0697	20.0087
Square	200	400	1000	38.7672	38.7842	45.8705	0.0093	0.0094	0.1041	41.1406
Square	200	400	1100	35.1227	35.1637	49.3206	0.3734	0.1452	0.3021	39.8690
Hexagonal	250	400	800	77.4895	125.0414	152.1225	0.1458	0.6772	2.8853	118.2178

## 5.2.2 Relation Between Wavelength Peak and Refractive Index

Figure 5.22 displays the relation between the wavelength peak and the refractive index for nanoplasmonic sensors with square and hexagonal nanohole arrays, periodicities ranging from 700 to 1100 nm with a constant nanohole diameter of 400 nm and a 250 nm gold layer thickness. It can be seen that as the RI increases, the wavelength peaks shift towards longer wavelengths, i.e. redshifts. This is a well-documented tendency in the literature [125, 221, 222, 223], substantiating the credibility of the obtained results. The straight line indicates the linear relationship between the wavelength peak position and the refractive index. Hence, the calibration curves can be utilized to determine the refractive index of a specific, unknown fluid concentration when the wavelength peak is known. It should be noted that the correlation is only valid for nanoparticles dispersed in solution.

## 5.2.3 Square Nanohole Array

Figure 5.23 presents the nanoplasmonic sensor with square nanohole arrays, a constant nanohole diameter of 400 nm, and gold layer thickness of 250 nm with periodicities ranging from 700 to 1100 nm. It can be seen that the slopes become steeper as the periodicity increases. This indicates that the sensitivity can be enhanced by increasing the periodicity in the nanohole arrays. The obtained sensitivities for the periodicities of 700 nm, 800 nm, 900 nm, 1000 nm, and 1100 nm are 28.2783 nm/RIU, 42.0227 nm/RIU, 62.3729 nm/RIU, 167.8118 nm/RIU, and 191.6612 nm/RIU, respectively.

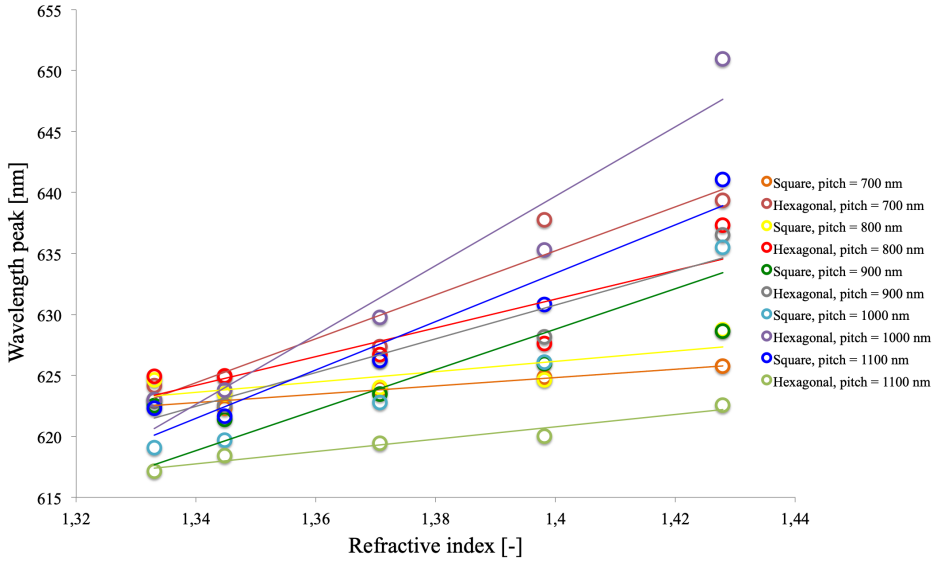


**Figure 5.22:** Relation between the wavelength peak and the refractive index for square and hexagonal nanohole arrays with constant nanohole diameters of 400 nm, constant gold layer thicknesses of 250 nm, and periodicities ranging from 700 to 1100 nm.

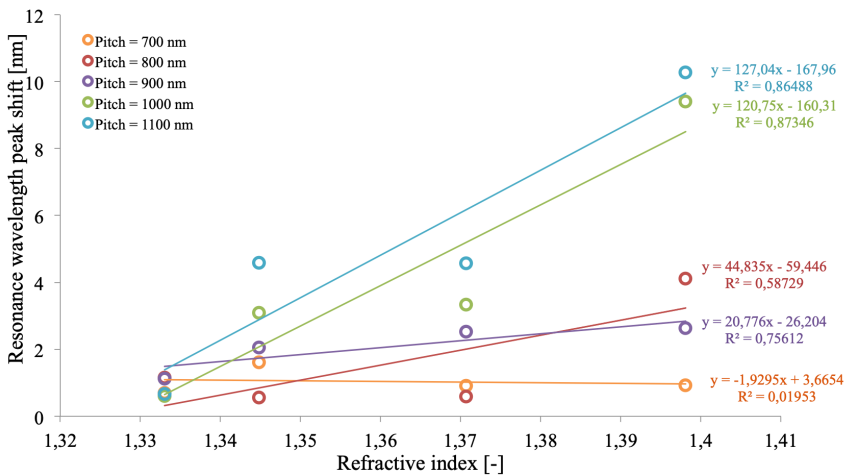


**Figure 5.23:** Relation between the resonance wavelength peak shifts and the refractive indices for square nanohole arrays with constant nanohole diameters of 400 nm, constant gold layer thickness of 250 nm, and periodicities ranging from 700 to 1100 nm. The linear regression function and corresponding  $R^2$  values are indicated.

### 5.2.4 Hexagonal Nanohole Array

Figure 5.24 displays the comparison of the nanoplasmonic sensor sensitivity for a sensor with hexagonal nanohole arrays, periodicities from 700 to 1100 nm, fixed nanohole diameter of 400 nm, and a gold layer thickness of 250 nm. The same tendency obtained for the sensor with square nanohole arrays can be seen, where the sensitivity increases for a larger pitch between the nanoholes, with 1100 nm pitch as an exception. It is unknown why the obtained sensitivity for the periodicity of 1100 nm differs from the observed trend. The acquired sensitivities are 155.2787 nm/RIU, 126.4715 nm/RIU, 137.6935 nm/RIU, 285.8275 nm/RIU, and 55.2378 nm/RIU for the different periodicities of 700 nm, 800 nm, 900 nm, 1000 nm, and 1100 nm, respectively.

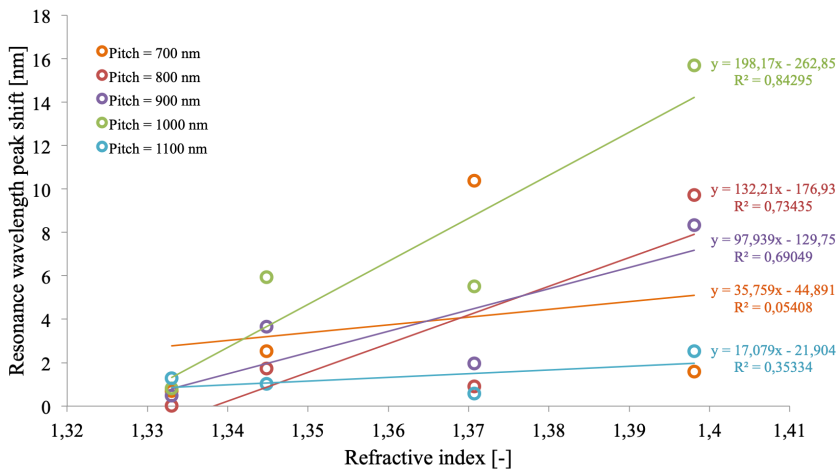


**Figure 5.24:** Relation between the resonance wavelength peak shifts and the refractive indices for hexagonal nanohole arrays with constant nanohole diameters of 400 nm, constant gold layer thickness of 250 nm, and periodicities ranging from 700 to 1100 nm. The linear regression function and corresponding  $R^2$  values are indicated.

### 5.2.5 Comparison of Square and Hexagonal Nanohole Array

Figure 5.25 shows the comparison of the two best sensor designs with square and hexagonal nanohole alignment, extracted from Figure 5.23 and 5.24. From the obtained results, it is clear that the hexagonal nanohole array with a periodicity of 1000 nm gives the highest sensitivity compared to the hexagonal alignment with an 800 nm pitch and the square alignments with 1000 and 1100 nm periodicities.



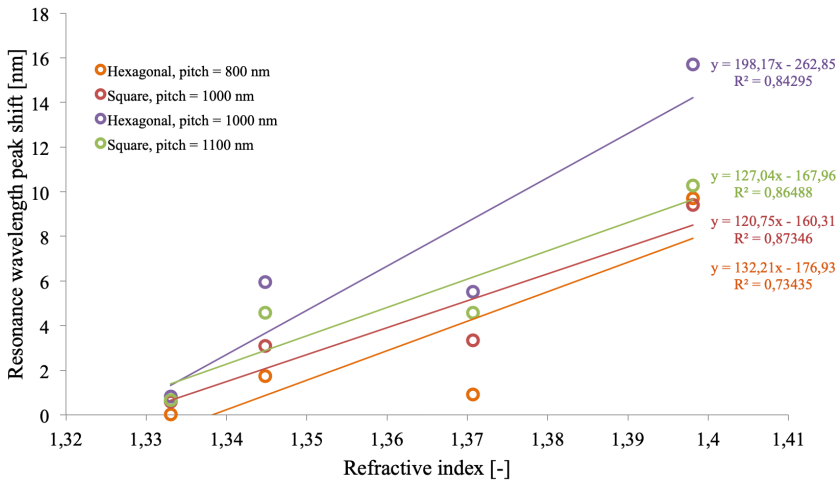


**Figure 5.25:** Comparison of the resonance wavelength peak shift against the refractive indices for the two best sensor designs with square and hexagonal nanohole arrays with constant nanohole diameters of 400 nm, constant gold layer thicknesses of 250 nm, and periodicities ranging from 700 to 1100 nm. The linear regression function and corresponding  $R^2$  values are indicated.

The sensitivity for the sensors with a constant nanohole diameter of 400 nm, 250 nm gold layer thickness, periodicity from 700 to 1100 nm, and a square or hexagonal nanohole alignment is compared in Figure 5.26.

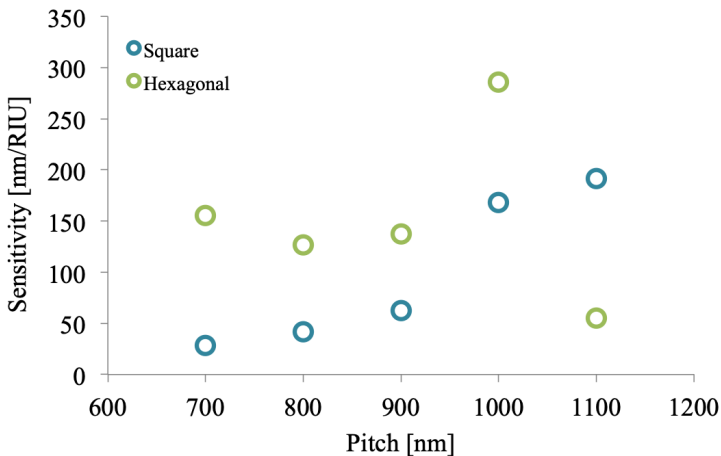


**Figure 5.26:** Comparison of the obtained sensitivity plotted against the pitch for square and hexagonal nanohole arrays. The sensor parameters are periodicities ranging between 700 and 1100 nm, a constant gold layer thickness of 250 nm, and a nanohole diameter of 400 nm.

From the results, it is clear that the sensitivity is generally higher for the hexagonal alignment than for the square arrays, except for the 1100 nm periodicity. This tendency coincides well with the obtained results by Ekşioğlu et al. [118] and Cetin et al. [134].

The higher sensitivity obtained for the hexagonal nanohole arrays can be helped explained by Equation 2.14. As seen from Table 5.3, the resonance wavelength peak shifts for the hexagonal nanohole array are larger than for the square alignment. Owing to the constant change in the refractive index, the sensitivity is directly affected by the resonance wavelength peak shift. Thus, a larger shift increases the sensor sensitivity.

**Table 5.3:** Difference in the resonant wavelength peak value for sensors with square and hexagonal nanohole arrays, a constant nanohole diameter of 400 nm, 250 nm gold layer thickness, and periodicities ranging from 700 to 1100 nm.

Nanohole array	Refractive index [-]	Resonance wavelength peak [nm]				
		Pitch = 700 nm	Pitch = 800 nm	Pitch = 900 nm	Pitch = 1000 nm	Pitch = 1100 nm
Square	1.33303	623.0067	624.6215	622.5297	619.0851	622.3147
	1.34481	622.3147	623.4706	621.4105	619.6866	621.6447
	1.37070	623.9294	624.0347	623.4706	622.7760	626.2284
	1.39809	624.8447	624.6243	625.9978	626.1118	630.8050
	1.42789	625.7749	628.7351	628.6354	635.5122	641.0764
Hexagonal	1.33303	624.1628	624.9426	623.0428	622.9968	617.1431
	1.34481	624.8551	624.9689	622.5656	623.8182	618.4268
	1.37070	627.3815	626.6976	626.2284	629.7664	619.4553
	1.39809	637.7610	627.6122	628.1842	635.2831	620.0311
	1.42789	639.3631	637.3229	636.5216	650.9765	622.5503

## 5.2.6 Relation Between Gold Layer Thickness and Sensor Sensitivity

Figure 5.27 shows the relation between the gold layer thickness and the refractive index sensitivity for sensors with a constant nanohole diameter of 400 nm, square nanohole alignment, and a periodicity ranging between 700 and 1100 nm.

For 700 and 800 nm periodicity, the sensitivity yields similar results for the 200 and 250 nm gold layer thicknesses. The sensitivity of the 200 nm gold layer thickness is 17.7347 nm/RIU and 47.2421 nm/RIU for 700 and 800 nm periodicity, respectively, while for the 250 nm gold layer thickness the sensitivity is 28.2783 nm/RIU for the 700 nm pitch and 42.0227 nm/RIU for the 800 nm pitch. As the periodicity is increased, the sensitivity of the sensor with 250 nm gold layer thickness is enhanced. In contrast, the sensor sensitivity with 200 nm gold layer thickness stays at a relatively low sensitivity value. The highest obtained sensitivity for the 250 nm gold layer thickness is 191.6612 nm/RIU with a periodicity of 1100 nm, whereas for the 200 nm gold layer thickness, the highest sensitivity value is 47.2421 nm/RIU for the sensor with an 800 nm periodicity. The sensitivity difference between the two gold layer thicknesses may be attributed to the decreasing resonant peak value for thinner gold film thicknesses displayed in Table 5.4. This concurs with the results obtained by Wu et al. [224].

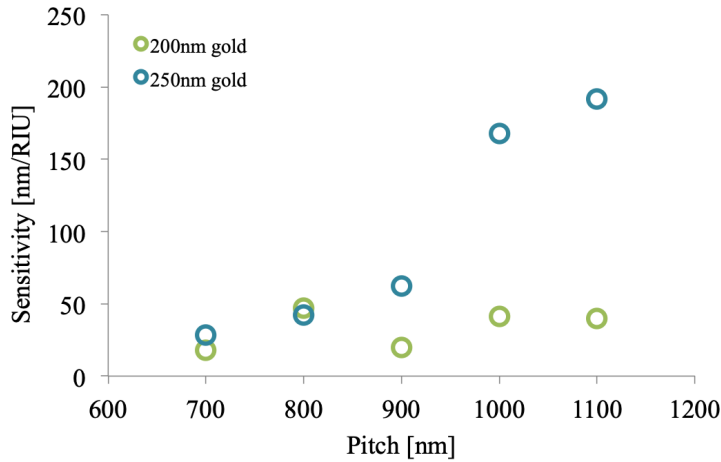


**Figure 5.27:** Relation between the gold layer thickness and refractive index sensitivity for square nanohole arrays with constant nanohole diameter of 400 nm and periodicities between 700 and 1100 nm.

**Table 5.4:** Difference in the resonant wavelength peak value for sensors with 200 and 250 nm gold layer thicknesses, a constant nanohole diameter of 400 nm, periodicities ranging from 700 to 1100 nm, and square nanohole arrays.

Gold layer thickness [nm]	Refractive index [-]	Resonance wavelength peak [nm]				
		Pitch = 700 nm	Pitch = 800 nm	Pitch = 900 nm	Pitch = 1000 nm	Pitch = 1100 nm
200	1.33303	617.0256	617.3743	617.1569	617.8367	619.1063
	1.34481	616.9254	618.7616	618.068	618.5304	617.8367
	1.37070	617.4912	619.7999	618.9929	619.4553	621.3939
	1.39809	618.5304	620.6115	619.3375	620.149	622.0861
	1.42789	618.7616	621.9988	619.1156	621.864	623.0091
250	1.33303	623.0067	624.6215	622.5297	619.0851	622.3147
	1.34481	622.3147	623.4706	621.4105	619.6866	621.6447
	1.37070	623.9294	624.0347	623.4706	622.7760	626.2284
	1.39809	624.8447	624.6243	625.9978	626.1118	630.8050
	1.42789	625.7749	628.7351	628.6354	635.5122	641.0764

Additionally, from Figure 5.28, the obtained spectra for the 250 nm gold layer thickness are observed to be sharper than for the 200 nm gold layer thickness. The peak sharpening will improve the sensing resolution and lower the detection limit. These observations correspond well with the findings of Chung et al. [111].

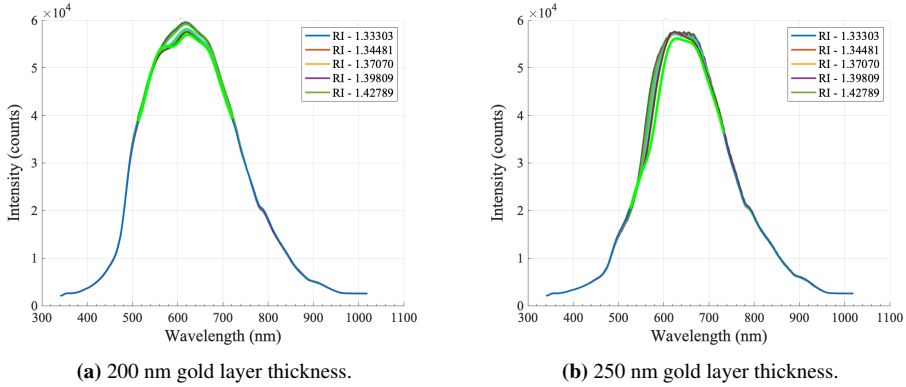


**Figure 5.28:** Experimental spectra of nanoplasmonic sensors with square nanohole arrays, a constant nanohole diameter of 400 nm, periodicities ranging from 700 to 1100 nm, and different gold layer thicknesses of 200 and 250 nm. A higher gold layer thickness results in a sharper peak.

### 5.2.7 Obtained Sensitivity Compared to Values From the Literature

The maximum sensitivity and the corresponding wavelength peak obtained from the experiments are compared with results found in the literature. The obtained sensitivity yields a relatively low value of  $\sim 286$  nm/RIU and the wavelength peak at 641 nm lies in the visible region. From Figure 5.29, it can be seen that for wavelengths in the near-infrared region (780-2500 nm), the sensitivity has a higher value than the obtained value in this work. Additionally, it can be seen from Table 5.5 that the higher sensitivities obtained in the literature are achieved by utilizing a nanohole diameter that size-matches with the exosome diameter. Thus, the low sensitivity value obtained in this work compared to the findings in the literature can be explained by the large nanohole diameter and a resonance wavelength peak that lies in the visible region.

**Table 5.5:** Comparison of the maximum obtained sensitivity and wavelength peak to values found in the literature.

Sensor parameters				Sensitivity [nm/RIU]	Wavelength peak [nm]	Reference
Lattice	nm Au	nm diameter	nm pitch			
Square	200	200	1400	1022	1550	[121]
Square (Double hole)	100	200 190 center spacing	600-800	600	850	[122]
Square	150-200	300	1500	1520	1540	[124]
Square	40	70-200	500-600	393	1000	[126]
Square	100	200	600	615	900	[128]
Square	125	200	600	600	850	[131]
Square	50	100	450	286	800	[133]
Hexagonal	250	400	1000	286	641	This work

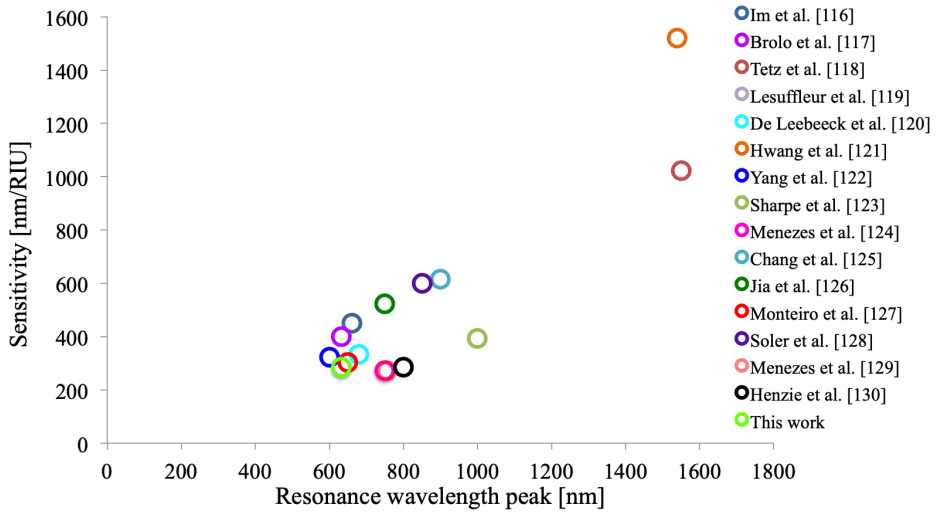


**Figure 5.29:** Maximum obtained sensitivity and resonance wavelength peak position compared to results found in the literature.

# Chapter 6

## Conclusion and Further Work

An experimental test campaign and an extensive literature review have been conducted in order to investigate the nanoplasmonic sensor sensitivity performance for different sensor designs and the mixing efficiency of three IDT designs for various flow rates and power applications. The following chapter provides concluding remarks based on the obtained results and discussion as well as recommendations for further work. This will be presented separately for the microfluidic mixing and the nanoplasmonic sensor.

### 6.1 Conclusion

#### Microfluidic Mixing

To the author's knowledge, the microchannels utilized in the conducted microfluidic mixing experiments possess the smallest features compared to the literature with their height of  $56\ \mu\text{m}$  and width of  $100\ \mu\text{m}$ . High mixing efficiencies are achieved and are comparable to results found in the literature. The highest mixing efficiency is obtained for the dual IDT of the 80 MHz IDT design with a value of 97.93% at a flow rate of  $500\ \mu\text{L}/\text{h}$  and a power input of 1500 mW.

The experimental results display a clear degradation of the mixing efficiency for higher flow rates. This observation is thought to be linked to the shorter SAW exposure time to the fluid streams. Another prominent reduction is observed for lower power applications into the system. This could be related to the decreased SAW amplitude affecting the amount of acoustic energy being absorbed by the fluid streams. The literature showed that for a lower frequency IDT design the mixing efficiency was anticipated to be higher than for higher

frequency IDTs. This was not observed for the 40 MHz and 80 MHz IDT designs, which displayed similar mixing performances for all flow rates and power inputs. However, both IDT designs had superior mixing efficiencies compared to the 120 MHz IDT design.

The comparison of the mixing performance of the single and dual IDT for certain power inputs indicated a faster mixing and an increased mixing efficiency for the dual IDT for all flow rates and power applications. The enhanced mixing performance of the dual IDT could be linked to the SAW generation by two IDTs, where the absorbed acoustic energy from the SAWs into the fluid streams is increased. However, by comparing the single and dual IDT for the same total energy input in the microfluidic device, there is no considerable increase in the mixing performance for the dual IDT.

## **Nanoplasmonic Sensor**

The effect of different geometrical parameters, including nanohole array, gold thickness, and periodicity on the nanoplasmonic sensor sensitivity has been investigated. Spectroscopy analysis of the different sensors demonstrates that the sensor made with a hexagonal nanohole array, nanohole diameters of 400 nm, 250 nm gold layer thickness, and a 1000 nm periodicity gives the highest sensitivity of 285.8275 nm/RIU.

The experimental results display an increase in the sensor sensitivity for the hexagonal nanohole array compared to the square alignment. The difference is a consequence of the larger spectrum shifts observed for the hexagonal nanohole arrangements. The variation in the gold layer thickness indicates a higher sensitivity and sharper spectrum curve for a higher thickness. This observation could be a result of the lower resonant wavelength peak value for the sensor with a thinner gold layer thickness.

The polynomial curve fitting order of the obtained spectra shows a significant effect on the sensitivity performance for the different nanoplasmonic sensor designs. The observed sensitivity variations are associated with the change in the resonance wavelength peak position from the fitted curves for polynomial orders of 15, 25, and 50.

## 6.2 Further Work

Based on the obtained knowledge from the literature review and the experimental testing, the recommended focus points for further research are:

- Microfluidic mixing
  - Study the temperature effect of the piezoelectric mixers as many biological samples are temperature-sensitive.
  - Further examine the mixing efficiency by analyzing the collected mixed fluids at the outlet.
  - Investigate why power limitations occur for the IDTs during experiments.
  - Investigate the mechanisms causing dissimilarities in the obtained mixing performances for similar IDTs as observed for IDT-1 and IDT-2 in this experimental campaign.
  - Further investigate the mixing performance of the 40 MHz and 80 MHz IDT designs to verify the findings in this master thesis.
- Nanoplasmonic sensor
  - Study how other geometrical features that offer strong electromagnetic field enhancements such as nanostars and nanorods affect the sensor sensitivity.
  - Study the effect on the sensor sensitivity by changing the nanohole parameters to coincide with exosome characteristics, such as size-matching and spectrum shifts towards the near-infrared region for analysis.
  - Investigate how smaller periodicities affect the sensor sensitivity.
  - Perform experiments with fluids acquiring different refractive indices to obtain calibration curves for the determination of refractive indices for specific fluid concentrations (e.g. exosomes, virus, proteins).
  - Investigate the difference in sensitivity for different polynomial orders of the regression curve fitting.
- Develop a device consisting of a nanoplasmonic sensor, microfluidic channel, and interdigital transducers for surface acoustic wave generation. Investigate if the incorporation of SAWs affects the sensor detection performance.





# Bibliography

- [1] The International Agency for Research on Cancer (IARC). "Press release N° 292 - Latest global cancer data: Cancer burden rises to 19.3 million new cases and 10.0 million cancer deaths in 2020". Available: [https://www.iarc.who.int/wp-content/uploads/2020/12/pr292\\_E.pdf](https://www.iarc.who.int/wp-content/uploads/2020/12/pr292_E.pdf), 2020. (Accessed: 2021-02-19).
- [2] A. Sønstebø. "Andelen som dør, har aldri vært mindre". Available: <https://www.ssb.no/befolkning/artikler-og-publikasjoner/andelen-som-dor-har-aldri-vaert-mindre>, 2019. (Accessed: 2021-02-19).
- [3] Cancer Registry of Norway. "Cancer in Norway 2019 - Cancer incidence, mortality, survival and prevalence in Norway". Available: [https://www.kreftregisteret.no/globalassets/cancer-in-norway/2019/cin\\_report.pdf](https://www.kreftregisteret.no/globalassets/cancer-in-norway/2019/cin_report.pdf), 2020. (Accessed: 2021-02-19).
- [4] A. P. Mathiesen. Nanoplasmonic biosensing for exosome and virus detection. Master's thesis, Norwegian University of Science and Technology, Trondheim, 2020.
- [5] M. H. Rashed, E. Bayraktar, G. K. Helal, M. F. Abd-Ellah, P. Amero, A. Chavez-Reyes, and C. Rodriguez-Aguayo. Exosomes: From garbage bins to promising therapeutic targets. *International Journal of Molecular Sciences*, 18(3):538, 2017.
- [6] A. V. Vlassov, S. Magdaleno, R. Setterquist, and R. Conrad. Exosomes: Current knowledge of their composition, biological functions, and diagnostic and therapeutic potentials. *Biochimica et Biophysica Acta (BBA) - General Subjects*, 1820(7):940–948, 2012.
- [7] J. A. Jackman, A. R. Ferhan, and N. Cho. Nanoplasmonic sensors for biointerfacial science. *Chemical Society Reviews*, 46(12):3615–3660, 2017.
- [8] C. Théry, L. Zitvogel, and S. Amigorena. Exosomes: composition, biogenesis and function. *Nature Reviews Immunology*, 2(8):569–579, 2002.

- 
- [9] M. Simons and G. Raposo. Exosomes – vesicular carriers for intercellular communication. *Current Opinion in Cell Biology*, 21(4):575–581, 2009.
- [10] H. Im, H. Shao, Y. I. Park, V. M. Peterson, C. M. Castro, R. Weissleder, and H. Lee. Label-free detection and molecular profiling of exosomes with a nano-plasmonic sensor. *Nature biotechnology*, 32(5):490–495, 2014.
- [11] C. de la Torre Gomez, R. V. Goreham, J. J. Bech Serra, T. Nann, and M. Kussmann. ”Exosomics” - a review of biophysics, biology and biochemistry of exosomes with a focus on human breast milk. *Frontiers in Genetics*, 9, 2018.
- [12] D. Raghu, J. A. Christodoulides, M. Christophersen, J. L. Liu, G. P. Anderson, M. Robitaille, J. M. Byers, M. P. Raphael, and K. Hamad-Schifferli. Nanoplasmonic pillars engineered for single exosome detection. *PLOS ONE*, 13(8):e0202773, 2018.
- [13] H. Valadi, K. Ekström, A. Bossios, M. Sjöstrand, J. J. Lee, and J. O. Lötvall. Exosome-mediated transfer of mrnas and micrnas is a novel mechanism of genetic exchange between cells. *Nature Cell Biology*, 9(6):654–659, 2007.
- [14] V. Palanisamy, S. Sharma, A. Deshpande, H. Zhou, J. Gimzewski, and D. T. Wong. Nanostructural and transcriptomic analyses of human saliva derived exosomes. *PLoS ONE*, 5(1), 2010.
- [15] X. Chen, Y. Ba, L. Ma, X. Cai, Y. Yin, K. Wang, J. Guo, Y. Zhang, J. Chen, X. Guo, Q. Li, X. Li, W. Wang, Y. Zhang, J. Wang, X. Jiang, Y. Xiang, C. Xu, J. Zheng, P. and Zhang, R. Li, H. Zhang, X. Shang, T. Gong, G. Ning, J. Wang, K. Zen, J. Zhang, and C. Zhang. Characterization of micrnas in serum: a novel class of biomarkers for diagnosis of cancer and other diseases. *Cell Research*, 18(10):997–1006, 2008.
- [16] A. R. Ferhan, J. A. Jackman, J. H. Park, N. Cho, and D. Kim. Nanoplasmonic sensors for detecting circulating cancer biomarkers. *Advanced Drug Delivery Reviews*, 125:48–77, 2018.
- [17] M. C. Henderson and D. O. Azorsa. The genomic and proteomic content of cancer cell-derived exosomes. *Frontiers in Oncology*, 2, 2012.
- [18] D. D. Taylor and C. Gerçel-Taylor. Microrna signatures of tumor-derived exosomes as diagnostic biomarkers of ovarian cancer. *Gynecologic Oncology*, 110(1):13–21, 2008.
- [19] G. Rabinowits, C. Gerçel-Taylor, J. M. Day, D. D. Taylor, and G. H. Kloecker. Exosomal microrna: A diagnostic marker for lung cancer. *Clinical Lung Cancer*, 10(1):42–46, 2009.
- [20] G. Tavoosidana, G. Ronquist, S. Darmanis, J. Yan, L. Carlsson, D. Wu, T. Conze, P. Ek, A. Semjonow, E. Eltze, A. Larsson, U. D. Landegren, and M. Kamali-Moghaddam. Multiple recognition assay reveals prostasomes as promising plasma biomarkers for prostate cancer. *Proceedings of the National Academy of Sciences*, 108(21):8809–8814, 2011.

- 
- [21] M. Logozzi, A. De Milito, L. Lugini, M. Borghi, L. Calabrò, M. Spada, M. Perdicchio, M. L. Marino, C. Federici, E. Iessi, D. Brambilla, G. Venturi, F. Lozupone, M. Santinami, V. Huber, M. Maio, L. Rivoltini, and S. Fais. High levels of exosomes expressing cd63 and caveolin-1 in plasma of melanoma patients. *PLoS ONE*, 4(4), 2009.
- [22] J. Li, C. A. Sherman-Baust, M. Tsai-Turton, R. E. Bristow, R. B. Roden, and P. J. Morin. Claudin-containing exosomes in the peripheral circulation of women with ovarian cancer. *BMC Cancer*, 9(1):244, 2009.
- [23] J. Nilsson, J. Skog, A. Nordstrand, V. Baranov, L. Mincheva-Nilsson, X. O. Breakefield, and A. Widmark. Prostate cancer-derived urine exosomes: a novel approach to biomarkers for prostate cancer. *British Journal of Cancer*, 100(10):1603–1607, 2009.
- [24] C. Corcoran, A. M. Friel, M. J. Duffy, J. Crown, and L. O’Driscoll. Intracellular and extracellular micrnas in breast cancer. *Clinical Chemistry*, 57(1):18–32, 2011.
- [25] G. Di Noto, M. Chiarini, L. Paolini, E. Mazzoldi, V. Giustini, A. Radeghieri, L. Caimi, and D. Ricotta. Immunoglobulin free light chains and gags mediate multiple myeloma extracellular vesicles uptake and secondary nfkb nuclear translocation. *Frontiers in Immunology*, 5, 2014.
- [26] E. G. Trams, C. J. Lauter, S. J. Norman, and U. Heine. Exfoliation of membrane ecto-enzymes in the form of micro-vesicles. *Biochimica et Biophysica Acta (BBA) - Biomembranes*, 645(1):63–70, 1981.
- [27] C. Harding, J. Heuser, and P. Stahl. Receptor-mediated endocytosis of transferrin and recycling of the transferrin receptor in rat reticulocytes. *Journal of Cell Biology*, 97(2):329–339, 1983.
- [28] B. T. Pan, K. Teng, C. Wu, M. Adam, and R. M. Johnstone. Electron microscopic evidence for externalization of the transferrin receptor in vesicular form in sheep reticulocytes. *The Journal of Cell Biology*, 101(3):942–948, 1985.
- [29] R. M. Johnstone, M. Adam, J. R. Hammond, L. Orr, and C. Turbide. Vesicle formation during reticulocyte maturation. association of plasma membrane activities with released vesicles (exosomes). *Journal of Biological Chemistry*, 262(19):9412–9420, 1987.
- [30] G. Raposo, H. W. Nijman, W. Stoorvogel, R. Liejendekker, C. V. Harding, C. J. Melief, and H. J. Geuze. B lymphocytes secrete antigen-presenting vesicles. *The Journal of Experimental Medicine*, 183(3):1161–1172, 1996.
- [31] R. Wu, W. Gao, K. Yao, and J. Ge. Roles of exosomes derived from immune cells in cardiovascular diseases. *Frontiers in Immunology*, 10, 2019.
- [32] C. Emanuelli, A. I. U. Shearn, A. Laftah, F. Fiorentino, B. C. Reeves, C. Beltrami, A. Mumford, A. Clayton, M. Gurney, S. Shantikumar, and G. D. Angelini. Coronary artery-bypass-graft surgery increases the plasma concentration of exosomes
-

- 
- carrying a cargo of cardiac micrnas: An example of exosome trafficking out of the human heart with potential for cardiac biomarker discovery. *PLOS ONE*, 11(4):e0154274, 2016.
- [33] S. Matsumoto, Y. Sakata, S. Suna, D. Nakatani, M. Usami, M. Hara, T. Kitamura, T. Hamasaki, S. Nanto, Y. Kawahara, and I. Komuro. Circulating p53-responsive micrnas are predictive indicators of heart failure after acute myocardial infarction. *Circulation Research*, 113(3):322–326, 2013.
- [34] J. Skog, T. Würdinger, S. van Rijn, D. H. Meijer, L. Gainche, W. T. Curry, B. S. Carter, A. M. Krichevsky, and X. O. Breakefield. Glioblastoma microvesicles transport rna and proteins that promote tumour growth and provide diagnostic biomarkers. *Nature Cell Biology*, 10(12):1470–1476, 2008.
- [35] L. Rajendran, M. Honsho, T. R. Zahn, P. Keller, K. D. Geiger, P. Verkade, and K. Simons. Alzheimer’s disease  $\beta$ -amyloid peptides are released in association with exosomes. *Proceedings of the National Academy of Sciences*, 103(30):11172–11177, 2006.
- [36] S. Saman, W. Kim, M. Raya, Y. Visnick, S. Miro, S. Saman, B. Jackson, A. C. McKee, V. E. Alvarez, N. C. Y. Lee, and G. F. Hall. Exosome-associated tau is secreted in tauopathy models and is selectively phosphorylated in cerebrospinal fluid in early alzheimer disease. *Journal of Biological Chemistry*, 287(6):3842–3849, 2012.
- [37] L. Alvarez-Erviti, Y. Seow, A. H. Schapira, C. Gardiner, I. L. Sargent, M. J. A. Wood, and J. M. Cooper. Lysosomal dysfunction increases exosome-mediated alpha-synuclein release and transmission. *Neurobiology of Disease*, 42(3):360–367, 2011.
- [38] T. Yang, P. Martin, B. Fogarty, A. Brown, K. Schurman, R. Phipps, V. P. Yin, P. Lockman, and S. Bai. Exosome delivered anticancer drugs across the blood-brain barrier for brain cancer therapy in danio rerio. *Pharmaceutical Research*, 32(6):2003–2014, 2015.
- [39] X. Zhuang, X. Xiang, W. Grizzle, D. Sun, S. Zhang, R. C. Axtell, S. Ju, J. Mu, L. Zhang, L. Steinman, D. Miller, and H. Zuang. Treatment of brain inflammatory diseases by delivering exosome encapsulated anti-inflammatory drugs from the nasal region to the brain. *Molecular Therapy*, 19(10):1769–1779, 2011.
- [40] S. Antimisiaris, S. Mourtas, and A. Marazioti. Exosomes and exosome-inspired vesicles for targeted drug delivery. *Pharmaceutics*, 10(4):218, 2018.
- [41] W. Ying, M. Riopel, G. Bandyopadhyay, Y. Dong, A. Birmingham, J. B. Seo, J. M. Ofrecio, J. Wollam, A. Hernandez-Carret, W. Fu, P. Li, and J. M. Olefsky. Adipose tissue macrophage-derived exosomal mirnas can modulate in vivo and in vitro insulin sensitivity. *Cell*, 171(2):372–384.e12, 2017.
- [42] M. Garcia-Contreras, R. W. Brooks, L. Boccuzzi, P. D. Robbins, and C. Ricordi. Exosomes as biomarkers and therapeutic tools for type 1 diabetes mellitus. *European Review for Medical and Pharmacological Sciences*, 21:2940–2956, 2017.

- 
- [43] S. Gatti, S. Bruno, M. C. Deregibus, A. Sondi, V. Cantaluppi, C. Tetta, and G. Camussi. Microvesicles derived from human adult mesenchymal stem cells protect against ischaemia–reperfusion-induced acute and chronic kidney injury. *Nephrology Dialysis Transplantation*, 26(5):1474–1483, 2011.
- [44] J. Ratajczak, K. Miekus, M. Kucia, J. Zhang, R. Reza, P. Dvorak, and M. Z. Ratajczak. Embryonic stem cell-derived microvesicles reprogram hematopoietic progenitors: evidence for horizontal transfer of mrna and protein delivery. *Leukemia*, 20(5):847–856, 2006.
- [45] I. del Conde, C. N. Shrimpton, P. Thiagarajan, and J. A. López. Tissue-factor–bearing microvesicles arise from lipid rafts and fuse with activated platelets to initiate coagulation. *Blood*, 106(5):1604–1611, 2005.
- [46] X. Zhang, X. Yuan, H. Shi, L. Wu, H. Qian, and W. Xu. Exosomes in cancer: small particle, big player. *Journal of Hematology & Oncology*, 8(1):83, 2015.
- [47] K. A. Willets and R. P. Van Duyne. Localized surface plasmon resonance spectroscopy and sensing. *Annual Review of Physical Chemistry*, 58(1):267–297, 2007.
- [48] S. Mariani and M. Minunni. Surface plasmon resonance applications in clinical analysis. *Analytical and Bioanalytical Chemistry*, 406(9):2303–2323, 2014.
- [49] B. Liedberg, C. Nylander, and I. Lundström. Biosensing with surface plasmon resonance — how it all started. *Biosensors and Bioelectronics*, 10(8):i–ix, 1995.
- [50] R. B. M. Schasfoort and A. J. Tudos. *Handbook of Surface Plasmon Resonance*. Royal Society of Chemistry, 2008.
- [51] L. Rayleigh. On the dynamical theory of gratings. *Proceedings of the Royal Society of London. Series A, Containing Papers of a Mathematical and Physical Character*, 79(532):399–416, 1907.
- [52] R. W. Wood. Anomalous diffraction gratings. *Physical Review*, 48(12):928–936, 1935.
- [53] U. Fano. The theory of anomalous diffraction gratings and of quasi-stationary waves on metallic surfaces (sommerfeld’s waves). *Journal of the Optical Society of America*, 31(3):213–222, 1941.
- [54] D. Bohm and D. Pines. A collective description of electron interactions. i. magnetic interactions. *Physical Review*, 82(5):625–634, 1951.
- [55] C. H. Palmer. Parallel diffraction grating anomalies\*. *Journal of the Optical Society of America*, 42(4):269, 1951.
- [56] C. J. Powell and J. B. Swan. Effect of oxidation on the characteristic loss spectra of aluminum and magnesium. *Physical Review*, 118(3):640–643, 1960.
-

- 
- [57] U. Jönsson, L. Fägerstam, B. Ivarsson, B. Johnsson, R. Karlsson, K. Lundh, S. Löfås, B. Persson, H. Roos, I. Rönnberg, S. Sjölander, E. Stenberg, R. Ståhlberg, C. Urbaniczky, H. Östlin, and M. Malmqvist. Real-time biospecific interaction analysis using surface plasmon resonance and a sensor chip technology. *Biotechniques*, 11:620–627, 1991.
- [58] M. Pirzada and Z. Altintas. Recent progress in optical sensors for biomedical diagnostics. *Micromachines*, 2020:356, 2020.
- [59] A. Roointan, T. A. Mir, S. I. Wani, Mati ur Rehman, K. K. Hussain, B. Ahmed, S. Abraham, A. Savardashtaki, G. Gandomani, M. Gandomani, R. Chinnappan, and M. H. Akhtar. Early detection of lung cancer biomarkers through biosensor technology: A review. *Journal of Pharmaceutical and Biomedical Analysis*, 164:93–103, 2019.
- [60] Deepa, S. Pundir, and C. S. Pundir. Detection of tumor suppressor protein p53 with special emphasis on biosensors: A review. *Analytical Biochemistry*, 588:113473, 2020.
- [61] L. Qian, Q. Li, K. Baryeh, W. Qiu, K. Li, J. Zhang, Q. Yu, D. Xu, W. Liu, R. E. Brand, X. Zhang, W. Chen, and G. Liu. Biosensors for early diagnosis of pancreatic cancer: a review. *Translational Research*, 213:67–89, 2019.
- [62] S. Mohammadzadeh-Asl, A. Keshtkar, J. E. N. Dolatabadi, and M. de la Guardia. Nanomaterials and phase sensitive based signal enhancement in surface plasmon resonance. *Biosensors and Bioelectronics*, 110:118–131, 2018.
- [63] F. Fathi, M. Rashidi, and Y. Omid. Ultra-sensitive detection by metal nanoparticles-mediated enhanced spr biosensors. *Talanta*, 192:118–127, 2019.
- [64] G. Yang, Z. Xiao, C. Tang, Y. Deng, H. Huang, and Z. He. Recent advances in biosensor for detection of lung cancer biomarkers. *Biosensors and Bioelectronics*, 141:111416, 2019.
- [65] B. de la Franier and M. Thompson. Early stage detection and screening of ovarian cancer: A research opportunity and significant challenge for biosensor technology. *Biosensors and Bioelectronics*, 135:71–81, 2019.
- [66] N. Chiu, T. Lin, and C. Kuo. Highly sensitive carboxyl-graphene oxide-based surface plasmon resonance immunosensor for the detection of lung cancer for cytokeratin 19 biomarker in human plasma. *Sensors and Actuators B: Chemical*, 265:264–272, 2018.
- [67] M. Loyez, J. Larrieu, S. Chevineau, M. Rimmelink, D. Leduc, B. Bondue, P. Lambert, J. Devière, R. Wattiez, and C. Caucheteur. In situ cancer diagnosis through online plasmonics. *Biosensors and Bioelectronics*, 131:104–112, 2019.
- [68] C. Ribaut, M. Loyez, J. Larrieu, S. Chevineau, P. Lambert, M. Rimmelink, R. Wattiez, and C. Caucheteur. Cancer biomarker sensing using packaged plasmonic optical fiber gratings: Towards in vivo diagnosis. *Biosensors and Bioelectronics*, 92:449–456, 2017.

- 
- [69] G. Ertürk, H. Özen, M. A. Tümer, B. Mattiasson, and A. Denizli. Microcontact imprinting based surface plasmon resonance (spr) biosensor for real-time and ultra-sensitive detection of prostate specific antigen (psa) from clinical samples. *Sensors and Actuators B: Chemical*, 224:823–832, 2016.
- [70] H. Kim, J. Park, D. H. Jeong, H. Lee, and S. Lee. Real-time detection of prostate-specific antigens using a highly reliable fiber-optic localized surface plasmon resonance sensor combined with micro fluidic channel. *Sensors and Actuators B: Chemical*, 273:891–898, 2018.
- [71] Y. Khan, A. Li, L. Chang, L. Li, and L. Guo. Gold nano disks arrays for localized surface plasmon resonance based detection of psa cancer marker. *Sensors and Actuators B: Chemical*, 255:1298–1307, 2018.
- [72] R. Liu, Q. Wang, Q. Li, X. Yang, K. Wang, and W. Nie. Surface plasmon resonance biosensor for sensitive detection of microrna and cancer cell using multiple signal amplification strategy. *Biosensors and Bioelectronics*, 87:433–438, 2017.
- [73] A. Weremijewicz, A. Sankiewicz, M. Tylicka, M. Komarowska, A. Tokarzewicz, W. Debek, E. Gorodkiewicz, and A. Hermanowicz. Matrix metalloproteinase-2 and its correlation with basal membrane components laminin-5 and collagen type iv in paediatric burn patients measured with surface plasmon resonance imaging (spri) biosensors. *Burns*, 44(4):931–940, 2018.
- [74] G. Breveglieri, E. D’Aversa, T. E. Gallo, P. Pellegatti, G. Guerra, L. C. Cosenza, A. Finotti, R. Gambari, and M. Borgatti. A novel and efficient protocol for surface plasmon resonance based detection of four  $\beta$ -thalassemia point mutations in blood samples and salivary swabs. *Sensors and Actuators B: Chemical*, 260:710–718, 2018.
- [75] F. Fathi, A. Rezagbakhsh, R. Rahbarghazi, and M. Rashidi. Early-stage detection of ve-cadherin during endothelial differentiation of human mesenchymal stem cells using spr biosensor. *Biosensors and Bioelectronics*, 96:358–366, 2017.
- [76] M. S. Iqbal, A. A. Siddiqui, C. Banerjee, S. Nag, S. Mazumder, R. De, S. J. Saha, S. K. Karri, and U. Bandyopadhyay. Detection of retromer assembly in plasmodium falciparum by immunosensing coupled to surface plasmon resonance. *Biochimica et Biophysica Acta (BBA) - Proteins and Proteomics*, 1866(5):722–730, 2018.
- [77] A. Sankiewicz, L. Romanowicz, M. Pyc, A. Hermanowicz, and E. Gorodkiewicz. Spr imaging biosensor for the quantitation of fibronectin concentration in blood samples. *Journal of Pharmaceutical and Biomedical Analysis*, 150:1–8, 2018.
- [78] H. Bhardwaj, G. Sumana, and C. A. Marquette. A label-free ultrasensitive microfluidic surface plasmon resonance biosensor for aflatoxin b1 detection using nanoparticles integrated gold chip. *Food Chemistry*, 307:125530, 2020.
- [79] H. Chen, F. Qi, H. Zhou, S. Jia, Y. Gao, K. Koh, and Y. Yin. Fe<sub>3</sub>O<sub>4</sub>@Au nanoparticles as a means of signal enhancement in surface plasmon resonance spectroscopy for thrombin detection. *Sensors and Actuators B: Chemical*, 212:505–511, 2015.
-



- 
- [80] D. A. Sadik, I. H. Boyaci, and M. Mutlu. Mixed monolayer decorated spr sensing surface for thrombin detection. *Journal of Pharmaceutical and Biomedical Analysis*, 176:112822, 2019.
- [81] Q. Li, Q. Wang, X. Yang, K. Wang, H. Zhang, and W. Nie. High sensitivity surface plasmon resonance biosensor for detection of microrna and small molecule based on graphene oxide-gold nanoparticles composites. *Talanta*, 174:521–526, 2017.
- [82] S. O. Kasap. *Optoelectronics and Photonics: Principles and Practices*. Prentice-Hall, Inc., 2001.
- [83] J. M. Cunningham, R. Pallardy, V. Setia, G. Shukla, and S. Sinha. "Definition of Snell's law". Available: <https://www.britannica.com/science/Snells-law>, 2020. (Accessed: 2020-06-21).
- [84] A. S. Hughes. Biosensing on the end of an optical fiber. Master's thesis, The George Washington University, Washington, 2015.
- [85] J. R. Reitz, F. J. Milford, and R. W. Christy. *Foundations of Electromagnetic Theory (4th Edition)*. Addison-Wesley Publishing Company, USA, 4 edition, 2008.
- [86] M. Cardona. Fresnel reflection and surface plasmons. *American Journal of Physics*, 39(10):1277–1277, 1971.
- [87] M. Li, S. K. Cushing, and N. Wu. Plasmon-enhanced optical sensors: a review. *Analyst*, 140(2):386–406, 2015.
- [88] A. J. Haes, S. Zou, G. C. Schatz, and R. P. Van Duyne. A nanoscale optical biosensor: The long range distance dependence of the localized surface plasmon resonance of noble metal nanoparticles. *The Journal of Physical Chemistry B*, 108(1):109–116, 2004.
- [89] P. Englebienne. Use of colloidal gold surface plasmon resonance peak shift to infer affinity constants from the interactions between protein antigens and antibodies specific for single or multiple epitopes. *Analyst*, 123(7):1599–1603, 1998.
- [90] G. Raschke, S. Kowarik, T. Franzl, C. Sönnichsen, T. A. Klar, J. Feldmann, A. Nichtl, and K. Kürzinger. Biomolecular recognition based on single gold nanoparticle light scattering. *Nano Letters*, 3(7):935–938, 2003.
- [91] A. J. Haes, L. Chang, W. L. Klein, and R. P. Van Duyne. Detection of a biomarker for alzheimer's disease from synthetic and clinical samples using a nanoscale optical biosensor. *Journal of the American Chemical Society*, 127(7):2264–2271, 2005.
- [92] M. Retsch, M. Schmelzeisen, H. Butt, and E. L. Thomas. Visible mie scattering in nonabsorbing hollow sphere powders. *Nano Letters*, 11(3):1389–1394, 2011.
- [93] D. Sarkar and N. J. Halas. General vector basis function solution of maxwell's equations. *Physical Review E*, 56(1):1102–1112, 1997.
-

- 
- [94] A. J. Haes, C. L. Haynes, and R. P. Van Duyne. Nanosphere lithography: Self-assembled photonic and magnetic materials. *MRS Proceedings*, 636:D4.8.1, 2000.
- [95] J. N. Anker, W. P. Hall, O. Lyandres, N. C. Shah, J. Zhao, and R. P. Van Duyne. Biosensing with plasmonic nanosensors. *Nature Materials*, 7(6):442–453, 2008.
- [96] P. K. Jain, K. s. Lee, I. H. El-Sayed, and M. A. El-Sayed. Calculated absorption and scattering properties of gold nanoparticles of different size, shape, and composition: Applications in biological imaging and biomedicine. *The Journal of Physical Chemistry B*, 110(14):7238–7248, 2006.
- [97] K. Lee and M. A. El-Sayed. Gold and silver nanoparticles in sensing and imaging: Sensitivity of plasmon response to size, shape, and metal composition. *The Journal of Physical Chemistry B*, 110(39):19220–19225, 2006.
- [98] A. Dmitriev. *Nanoplasmonic Sensors*. Springer New York, 2012.
- [99] J. S. Wilson. *Sensor Technology Handbook*. Elsevier, 2004.
- [100] J. Homola, S. S. Yee, and G. Gauglitz. Surface plasmon resonance sensors: review. *Sensors and Actuators B: Chemical*, 54(1):3–15, 1999.
- [101] C. M. Hussain and R. Keçili. *Modern Environmental Analysis Techniques for Pollutants*. Elsevier Inc., 2020.
- [102] P. K. Jain, X. Huang, I. H. El-Sayed, and M. A. El-Sayed. Noble metals on the nanoscale: Optical and photothermal properties and some applications in imaging, sensing, biology, and medicine. *Accounts of Chemical Research*, 41(12):1578–1586, 2008.
- [103] R. Weissleder. A clearer vision for in vivo imaging. *Nature Biotechnology*, 19(4):316–317, 2001.
- [104] E. Martinsson. *Nanoplasmonic Sensing using Metal Nanoparticles*. PhD thesis, Linköping University, Sweden, 2014.
- [105] L. Guo, J. A. Jackman, H. Yang, P. Chen, N. Cho, and D. Kim. Strategies for enhancing the sensitivity of plasmonic nanosensors. *Nano Today*, 10(2):213–239, 2015.
- [106] P. K. Jain and M. A. El-Sayed. Surface plasmon resonance sensitivity of metal nanostructures: Physical basis and universal scaling in metal nanoshells. *The Journal of Physical Chemistry C*, 111(47):17451–17454, 2007.
- [107] Y. Sun and Y. Xia. Increased sensitivity of surface plasmon resonance of gold nanoshells compared to that of gold solid colloids in response to environmental changes. *Analytical Chemistry*, 74(20):5297–5305, 2002.
- [108] P. K. Jain, W. Huang, and M. A. El-Sayed. On the universal scaling behavior of the distance decay of plasmon coupling in metal nanoparticle pairs: A plasmon ruler equation. *Nano Letters*, 7(7):2080–2088, 2007.
-

- 
- [109] A. D. McFarland and R. P. Van Duyne. Single silver nanoparticles as real-time optical sensors with zeptomole sensitivity. *Nano Letters*, 3(8):1057–1062, 2003.
- [110] A. J. Haes and R. P. Van Duyne. A nanoscale optical biosensor: Sensitivity and selectivity of an approach based on the localized surface plasmon resonance spectroscopy of triangular silver nanoparticles. *Journal of the American Chemical Society*, 124(35):10596–10604, 2002.
- [111] T. Chung, S. Lee, E. Y. Song, H. Chun, and B. Lee. Plasmonic nanostructures for nano-scale bio-sensing. *Sensors*, 11(11):10907–10929, 2011.
- [112] W. J. Galush, S. A. Shelby, M. J. Mulvihill, A. Tao, P. Yang, and J. T. Groves. A nanocube plasmonic sensor for molecular binding on membrane surfaces. *Nano Letters*, 9(5):2077–2082, 2009.
- [113] S. K. Dondapati, T. K. Sau, C. Hrelescu, T. A. Klar, F. D. Stefani, and J. Feldmann. Label-free biosensing based on single gold nanostars as plasmonic transducers. *ACS Nano*, 4(11):6318–6322, 2010.
- [114] A. Agharazy Dormeny, P. Abedini Sohi, and M. Kahrizi. Design and simulation of a refractive index sensor based on spr and lspr using gold nanostructures. *Results in Physics*, 16:102869, 2020.
- [115] X. Wang, Y. Wang, X. Yang, and Y. Cao. Numerical simulation on the lspr-effective core-shell copper/graphene nanofluids. *Solar Energy*, 181:439–451, 2019.
- [116] M. R. Rakhshani and M. A. Mansouri-Birjandi. Engineering hexagonal array of nanoholes for high sensitivity biosensor and application for human blood group detection. *IEEE Transactions on Nanotechnology*, 17(3):475–481, 2018.
- [117] P. Singh. Spr biosensors: Historical perspectives and current challenges. *Sensors and Actuators B: Chemical*, 229:110–1301, 2016.
- [118] Y. Ekşioğlu, A. E. Cetin, and J. Petráček. Optical response of plasmonic nanohole arrays: Comparison of square and hexagonal lattices. *Plasmonics*, 11(3):851–856, 2016.
- [119] H. Im, S. H. Lee, N. J. Wittenberg, T. W. Johnson, N. C. Lindquist, P. Nagpal, D. J. Norris, and S. Oh. Template-stripped smooth ag nanohole arrays with silica shells for surface plasmon resonance biosensing. *ACS Nano*, 5(8):6244–6253, 2011.
- [120] A. G. Brolo, R. Gordon, B. Leathem, and K. L. Kavanagh. Surface plasmon sensor based on the enhanced light transmission through arrays of nanoholes in gold films. *Langmuir*, 20(12):4813–4815, 2004.
- [121] K. A. Tetz, L. Pang, and Y. Fainman. High-resolution surface plasmon resonance sensor based on linewidth-optimized nanohole array transmittance. *Optics Letters*, 31(10):1528–1530, 2006.

- 
- [122] A. Lesuffleur, H. Im, N. C. Lindquist, and S. Oh. Periodic nanohole arrays with shape-enhanced plasmon resonance as real-time biosensors. *Applied Physics Letters*, 90(24):243110, 2007.
- [123] A. De Leebeeck, L. K. S. Kumar, V. de Lange, D. Sinton, R. Gordon, and A. G. Brolo. On-chip surface-based detection with nanohole arrays. *Analytical Chemistry*, 79(11):4094–4100, 2007.
- [124] G. M. Hwang, L. Pang, E. H. Mullen, and Y. Fainman. Plasmonic sensing of biological analytes through nanoholes. *IEEE Sensors Journal*, 8(12):2074–2079, 2008.
- [125] J. Yang, J. Ji, J. M. Hogle, and D. N. Larson. Metallic nanohole arrays on fluoropolymer substrates as small label-free real-time bioprobes. *Nano Letters*, 8(9):2718–2724, 2008.
- [126] J. C. Sharpe, J. S. Mitchell, L. Lin, N. Sedoglavich, and R. J. Blaikie. Gold nanohole array substrates as immunobiosensors. *Analytical Chemistry*, 80(6):2244–2249, 2008.
- [127] J. W. de Menezes, A. Thesing, C. Valsecchi, L. E. G. Armas, and A. G. Brolo. Improving the performance of gold nanohole array biosensors by controlling the optical collimation conditions. *Applied Optics*, 54(21):6502–6507, 2015.
- [128] T. Chang, M. Huang, A. A. Yanik, H. Tsai, P. Shi, S. Aksu, M. F. Yanik, and H. Altug. Large-scale plasmonic microarrays for label-free high-throughput screening. *Lab on a Chip*, 11(21):3596–3602, 2011.
- [129] P. Jia, H. Jiang, J. Sabarinathan, and J. Yang. Plasmonic nanohole array sensors fabricated by template transfer with improved optical performance. *Nanotechnology*, 24(19):195501, 2013.
- [130] J. P. Monteiro, J. H. de Oliveira, E. Radovanovic, A. G. Brolo, and E. M. Girotto. Microfluidic plasmonic biosensor for breast cancer antigen detection. *Plasmonics*, 11:45–51, 2016.
- [131] M. Soler, A. Belushkin, A. Cavallini, C. Kebbi-Beghdadi, G. Greub, and H. Altug. Multiplexed nanoplasmonic biosensor for one-step simultaneous detection of chlamydia trachomatis and neisseria gonorrhoeae in urine. *Biosensors and Bioelectronics*, 94:560–567, 2017.
- [132] J. W. de Menezes, J. Ferreira, M. J. L. Santos, L. Cescato, and A. G. Brolo. Large-area fabrication of periodic arrays of nanoholes in metal films and their application in biosensing and plasmonic-enhanced photovoltaics. *Advanced Functional Materials*, 20(22):3918–3924, 2010.
- [133] J. Henzie, M. H. Lee, and T. W. Odom. Multiscale patterning of plasmonic metamaterials. *Nature Nanotechnology*, 2(9):549–554, 2007.
-

- 
- [134] A. E. Cetin, M. Dršata, Y. Ekşioğlu, and J. Petráček. Effect of lattice geometry on optical transmission through subwavelength nanohole arrays. In *2016 10th International Congress on Advanced Electromagnetic Materials in Microwaves and Optics (METAMATERIALS)*, pages 280–282, 2016.
- [135] L. Pang, G. M. Hwang, B. Slutsky, and Y. Fainman. Spectral sensitivity of two-dimensional nanohole array surface plasmon polariton resonance sensor. *Applied Physics Letters*, 91(12):123112, 2007.
- [136] I. Dolev, I. Epstein, and A. Arie. Surface-plasmon holographic beam shaping. *Physical Review Letters*, 109(20):203903, 2012.
- [137] L. D. Negro. Engineering aperiodic order in nanoplasmonics: past, present, and future opportunities. In *Photonic and Phononic Properties of Engineered Nanostructures*, San Francisco, California, United States, 2011.
- [138] C. Forestiere, G. Miano, S. V. Boriskina, and L. D. Negro. The role of nanoparticle shapes and deterministic aperiodicity for the design of nanoplasmonic arrays. *Optics Express*, 17(12):9648–9661, 2009.
- [139] M. Schnell, A. García-Etxarri, A. J. Huber, K. Crozier, J. Aizpurua, and R. Hillenbrand. Controlling the near-field oscillations of loaded plasmonic nanoantennas. *Nature Photonics*, 3(5):287–291, 2009.
- [140] P. K. Jain and M. A. El-Sayed. Plasmonic coupling in noble metal nanostructures. *Chemical Physics Letters*, 487(4):153–164, 2010.
- [141] R. Taubert, R. Ameling, T. Weiss, A. Christ, and H. Giessen. From near-field to far-field coupling in the third dimension: Retarded interaction of particle plasmons. *Nano Letters*, 11(10):4421–4424, 2011.
- [142] A. E. Schlather, N. Large, A. S. Urban, P. Nordlander, and N. J. Halas. Near-field mediated plexcitonic coupling and giant rabi splitting in individual metallic dimers. *Nano Letters*, 13(7):3281–3286, 2013.
- [143] Y. Huang, X. Zhang, E. Ringe, M. Hou, L. Ma, and Z. Zhang. Tunable lattice coupling of multipole plasmon modes and near-field enhancement in closely spaced gold nanorod arrays. *Scientific Reports*, 6(1):23159, 2016.
- [144] G. M. Whitesides. The origins and the future of microfluidics. *Nature*, 442(7101):368–373, 2006.
- [145] A. Barani, H. Paktinat, M. Janmaleki, A. Mohammadi, P. Mosaddegh, A. Fadaei-Tehrani, and A. Sanati-Nezhad. Microfluidic integrated acoustic waving for manipulation of cells and molecules. *Biosensors and Bioelectronics*, 85:714–725, 2016.
- [146] S. Zhang, Y. Wang, P. Onck, and J. den Toonder. A concise review of microfluidic particle manipulation methods. *Microfluidics and Nanofluidics*, 24(4):24, 2020.
- [147] V. Hessel, H. Löwe, and F. Schönfeld. Micromixers—a review on passive and active mixing principles. *Chemical Engineering Science*, 60(8):2479–2501, 2005.
-

- 
- [148] C. Lee, C. Chang, Y. Wang, and L. Fu. Microfluidic mixing: A review. *International Journal of Molecular Sciences*, 12(5):3263–3287, 2011.
- [149] N. Nguyen and Z. Wu. Micromixers—a review. *Journal of Micromechanics and Microengineering*, 15:1, 2005.
- [150] W. Tseng, J. Lin, W. Sung, S. Chen, and G. Lee. Active micro-mixers using surface acoustic waves on y-cut 128° linbo3. *Journal of Micromechanics and Microengineering*, 16(3):539–548, 2006.
- [151] T. Luong, V. Phan, and N. Nguyen. High-throughput micromixers based on acoustic streaming induced by surface acoustic wave. *Microfluidics and Nanofluidics*, 10(3):619–625, 2011.
- [152] M. C. Jo and R. Guldiken. Dual surface acoustic wave-based active mixing in a microfluidic channel. *Sensors and Actuators A: Physical*, 196:1–7, 2013.
- [153] Q. Zeng, F. Guo, L. Yao, H. W. Zhu, L. Zheng, Z. X. Guo, W. Liu, Y. Chen, S. S. Guo, and X. Z. Zhao. Milliseconds mixing in microfluidic channel using focused surface acoustic wave. *Sensors and Actuators B: Chemical*, 160(1):1552–1556, 2011.
- [154] Z. Mao, Y. Xie, F. Guo, L. Ren, P. Huang, Y. Chen, J. Rufo, F. Costanzo, and T. J. Huang. Experimental and numerical studies on standing surface acoustic wave microfluidics. *Lab on a Chip*, 16(3):515–524, 2016.
- [155] M. C. Jo and R. Guldiken. Effects of polydimethylsiloxane (pdms) microchannels on surface acoustic wave-based microfluidic devices. *Microelectronic Engineering*, 113:98–104, 2014.
- [156] K. Sritharan, C. J. Strobl, M. F. Schneider, A. Wixforth, and Z. Guttenberg. Acoustic mixing at low reynold’s numbers. *Applied Physics Letters*, 88(5):054102, 2006.
- [157] V. Skowronek, R. W. Rambach, L. Schmid, K. Haase, and T. Franke. Particle deflection in a poly(dimethylsiloxane) microchannel using a propagating surface acoustic wave: Size and frequency dependence. *Analytical Chemistry*, 85(20):9955–9959, 2013.
- [158] G. Destgeer and H. J. Sung. Recent advances in microfluidic actuation and micro-object manipulation via surface acoustic waves. *Lab on a Chip*, 15(13):2722–2738, 2015.
- [159] J. M. Ribe. *Microfluidic devices for active and passive separation of submicron particles*. PhD thesis, Norwegian University of Science and Technology, Trondheim, 2017.
- [160] H. Bruus. Acoustofluidics 1: Governing equations in microfluidics. *Lab on a Chip*, 11(22):3742–3751, 2011.
-

- 
- [161] Y. Q. Fu, J. K. Luo, N. T. Nguyen, A. J. Walton, A. J. Flewitt, X. T. Zu, Y. Li, G. McHale, A. Matthews, E. Iborra, H. Du, and W. I. Milne. Advances in piezoelectric thin films for acoustic biosensors, acoustofluidics and lab-on-chip applications. *Progress in Materials Science*, 89:31–91, 2017.
- [162] L. Y. Yeo and J. R. Friend. Ultrafast microfluidics using surface acoustic waves. *Biomicrofluidics*, 3(1), 2009.
- [163] J. R. Friend and L. Y. Yeo. Microscale acoustofluidics: Microfluidics driven via acoustics and ultrasonics. *Reviews of Modern Physics*, 83(2):647–704, 2011.
- [164] L. Y. Yeo and J. R. Friend. Surface acoustic wave microfluidics. *Annual Review of Fluid Mechanics*, 46(1):379–406, 2014.
- [165] G. L. Coté, R. M. Lec, and M. V. Pishko. Emerging biomedical sensing technologies and their applications. *IEEE Sensors Journal*, 3(3):251–266, 2003.
- [166] L. Rayleigh. On waves propagated along the plane surface of an elastic solid. *Proceedings of the London Mathematical Society*, s1-17(1):4–11, 1885.
- [167] N. Tesla. "Electrical condenser". Available: <https://patentimages.storage.googleapis.com/ce/f7/77/74de1fb70f15d0/US464667.pdf>. (Pat. No. US464667A).
- [168] R. M. White and F. W. Voltmer. Direct piezoelectric coupling to surface elastic waves. *Applied Physics Letters*, 7(12):314–316, 1965.
- [169] G. S. Calabrese, H. Wohlthen, and M. K. Roy. Surface acoustic wave devices as chemical sensors in liquids. evidence disputing the importance of rayleigh wave propagation. *Analytical Chemistry*, 59(6):833–837, 1987.
- [170] A. Yotsumoto, R. Nakamura, S. Shoji, and T. Wada. Fabrication of an integrated mixing/reaction micro flow cell for  $\mu$ tas. In: *Harrison D.J., van den Berg A. (eds). Micro Total Analysis Systems '98, Springer, Dordrecht*, pages 185–188, 1998.
- [171] J. Nam and C. S. Lim. Micromixing using swirling induced by three-dimensional dual surface acoustic waves (3d-dsaw). *Sensors and Actuators B: Chemical*, 255:3434–3440, 2018.
- [172] M. Z. Atashbar, A. Z. Sadek, W. Wlodarski, S. Sriram, M. Bhaskaran, C. J. Cheng, R. B. Kaner, and K. Kalantar-zadeh. Layered saw gas sensor based on csa synthesized polyaniline nanofiber on aln on  $64^\circ$  yx linbo3 for h2 sensing. *Sensors and Actuators B: Chemical*, 138(1):85–89, 2009.
- [173] M. Z. Atashbar, B. J. Bazuin, M. Simpeh, and S. Krishnamurthy. 3d fe simulation of h2 saw gas sensor. *Sensors and Actuators B: Chemical*, 111-112:213–218, 2005.
- [174] M. Plotner, O. Berger, H. Stab, W. Fischer, P. Konig, D. Beyerlein, and A. Schwarz. Miniaturized gas monitoring system employing several saw sensors. In *Proceedings of the 2001 IEEE International Frequency Control Symposium and PDA Exhibition (Cat. No.01CH37218)*, 2001.
-

- 
- [175] S. Sivaramakrishnan, R. Rajamani, C. S. Smith, K. A. McGee, K. R. Mann, and N. Yamashita. Carbon nanotube-coated surface acoustic wave sensor for carbon dioxide sensing. *Sensors and Actuators B: Chemical*, 132(1):296–304, 2008.
- [176] F. M. Yasin, K. F. Tye, and M. B. I. Reaz. Design and implementation of interface circuitry for cmos-based saw gas sensors. In *Proceedings 2005 IEEE International SOC Conference*, 2005.
- [177] N. Levit, D. Pestov, and G. Tepper. High surface area polymer coatings for saw-based chemical sensor applications. *Sensors and Actuators B: Chemical*, 82(2):241–249, 2002.
- [178] D. Li and M. Ma. Surface acoustic wave microsensors based on cyclodextrin coatings. *Sensors and Actuators B: Chemical*, 69(1):75–84, 2000.
- [179] O. Onen, A. Sisman, N. D. Gallant, P. Kruk, and R. Guldiken. A urinary bcl-2 surface acoustic wave biosensor for early ovarian cancer detection. *Sensors*, 12(6):7423–7437, 2012.
- [180] A. Tretjakov, V. Syritski, J. Reut, R. Boroznjak, and A. Öpik. Molecularly imprinted polymer film interfaced with surface acoustic wave technology as a sensing platform for label-free protein detection. *Analytica Chimica Acta*, 902:182–188, 2016.
- [181] X. Liu, J. Wang, X. Mao, Y. Ning, and G. Zhang. Single-shot analytical assay based on graphene-oxide-modified surface acoustic wave biosensor for detection of single-nucleotide polymorphisms. *Analytical Chemistry*, 87(18):9352–9359, 2015.
- [182] K. Chang, Y. Pi, W. Lu, F. Wang, F. Pan, F. Li, S. Jia, J. Shi, S. Deng, and M. Chen. Label-free and high-sensitive detection of human breast cancer cells by aptamer-based leaky surface acoustic wave biosensor array. *Biosensors and Bioelectronics*, 60:318–324, 2014.
- [183] Y. W. Kim, M. T. Meyer, A. Berkovich, S. Subramanian, A. A. Iliadis, W. E. Bentley, and R. Ghodssi. A surface acoustic wave biofilm sensor integrated with a treatment method based on the bioelectric effect. *Sensors and Actuators A: Physical*, 238:140–149, 2016.
- [184] D. Li, Y. Feng, L. Zhou, Z. Ye, J. Wang, Y. Ying, C. Ruan, R. Wang, and Y. Li. Label-free capacitive immunosensor based on quartz crystal au electrode for rapid and sensitive detection of escherichia coli o157:h7. *Analytica Chimica Acta*, 687(1):89–96, 2011.
- [185] T. Wang, R. Green, R. R. Nair, M. Howell, S. Mohapatra, R. Guldiken, and S. S. Mohapatra. Surface acoustic waves (saw)-based biosensing for quantification of cell growth in 2d and 3d cultures. *Sensors*, 15(12):32045–32055, 2015.
- [186] D. Matatagui, J. L. Fontecha, M. J. Fernández, I. Gràcia, C. Cané, J. P. Santos, and M. C. Horrillo. Love-wave sensors combined with microfluidics for fast detection of biological warfare agents. *Sensors*, 14(7):12658–12669, 2014.
-



- 
- [187] M. Puiu, A. Gurban, L. Rotariu, S. Brajnicov, C. Viespe, and C. Bala. Enhanced sensitive love wave surface acoustic wave sensor designed for immunoassay formats. *Sensors*, 15(5):10511–10525, 2015.
- [188] D. Matatagui, D. Moynet, M. J. Fernández, J. Fontecha, J. P. Esquivel, I. Gràcia, C. Cané, C. Déjous, D. Rebière, J. P. Santos, and M. C. Horrillo. Detection of bacteriophages in dynamic mode using a love-wave immunosensor with microfluidics technology. *Sensors and Actuators B: Chemical*, 185:218–224, 2013.
- [189] R. J. Shilton, M. Travagliati, F. Beltram, and M. Cecchini. Nanoliter-droplet acoustic streaming via ultra high frequency surface acoustic waves. *Advanced Materials*, 26(29):4941–4946, 2014.
- [190] R. J. Shilton, V. Mattoli, M. Travagliati, M. Agostini, A. Desii, F. Beltram, and M. Cecchini. Rapid and controllable digital microfluidic heating by surface acoustic waves. *Advanced Functional Materials*, 25(37):5895–5901, 2015.
- [191] J. T. Luo, N. R. Gerdali, J. H. Guan, G. McHale, G. G. Wells, and Y. Q. Fu. Slippery liquid-infused porous surfaces (slips) and surface acoustic wave droplet transportation. *American Physical Society*, 7(1):014017, 2017.
- [192] T. Frommelt, M. Kostur, M. Wenzel-Schäfer, P. Talkner, P. Hänggi, and A. Wixforth. Microfluidic mixing via acoustically driven chaotic advection. *Physical Review Letters*, 100(3):034502, 2008.
- [193] X. Ding, P. Li, S. Steven Lin, Z. S. Stratton, N. Nama, F. Guo, D. Slotcavage, X. Mao, J. Shi, F. Costanzo, and T. Jun Huang. Surface acoustic wave microfluidics. *Lab on a Chip*, 13(18):3626–3649, 2013.
- [194] S. S. Lin, X. Mao, and T. J. Huang. Surface acoustic wave (saw) acoustophoresis: now and beyond. *Lab on a Chip*, 12(16):2766–2770, 2012.
- [195] Y. J. Guo, H. B. Lv, Y. F. Li, X. L. He, J. Zhou, J. K. Luo, X. T. Zu, A. J. Walton, and Y. Q. Fu. High frequency microfluidic performance of linbo<sub>3</sub> and zno surface acoustic wave devices. *Journal of Applied Physics*, 116(2):024501, 2014.
- [196] W. Connacher, N. Zhang, A. Huang, J. Mei, S. Zhang, T. Gopesh, and J. Friend. Micro/nano acoustofluidics: materials, phenomena, design, devices, and applications. *Lab on a Chip*, 18(4):1952–1996, 2018.
- [197] W. Cui, H. Zhang, H. Zhang, Y. Yang, M. He, H. Qu, W. Pang, D. Zhang, and X. Duan. Localized ultrahigh frequency acoustic fields induced micro-vortices for submilliseconds microfluidic mixing. *Applied Physics Letters*, 109(25):253503, 2016.
- [198] P. Gelin, Ö. Sukas, K. Hellemans, D. Maes, and W. Malsche. Study on the mixing and migration behavior of micron-size particles in acoustofluidics. *Chemical Engineering Journal*, 369, 2019.
-

- 
- [199] M. Alghane, B. X. Chen, Y. Q. Fu, Y. Li, J. K. Luo, and A. J. Walton. Experimental and numerical investigation of acoustic streaming excited by using a surface acoustic wave device on a  $128^\circ$  yx-linbo3 substrate. *Journal of Micromechanics and Microengineering*, 21(1):015005, 2011.
- [200] M. Alghane, Y. Q. Fu, B. X. Chen, Y. Li, M. P. Y. Desmulliez, and A. J. Walton. Frequency effect on streaming phenomenon induced by rayleigh surface acoustic wave in microdroplets. *Journal of Applied Physics*, 112(8):084902, 2012.
- [201] G. A. Álvarez. Microfluidics mixing using surface acoustic waves (saw). Master's thesis, Norwegian University of Science and Technology (NTNU), 2019.
- [202] R. A. Lawson and A. P. G. Robinson. *Frontiers of Nanoscience*. Elsevier, 2016.
- [203] A. Pimpin and W. Srituravanich. Review on micro- and nanolithography techniques and their applications. *Engineering Journal*, 16(1):37–56, 2012.
- [204] Y. Xia and G. M. Whitesides. Soft lithography. *Annual Review of Materials Science*, 28(1):153–184, 1998.
- [205] The Dow Chemical Company. Sylgard 184 silicone elastomer product information. (11):4, 2017.
- [206] V. R. Manfrinato, L. Zhang, D. Su, H. Duan, R. G. Hobbs, E. A. Stach, and K. K. Berggren. Resolution limits of electron-beam lithography toward the atomic scale. *Nano Letters*, 13(4):1555–1558, 2013.
- [207] NTNU NorFab. "Tutorial - Beam Current and Pitch". Available: <http://ntnu.norfab.no/WebForms/Equipment/EquipmentView.aspx?toolId=87>. Document: Spot size - Pitch guide, (Accessed: 2020-11-19).
- [208] M. Altissimo. E-beam lithography for micro-/nanofabrication. *Biomicrofluidics*, 4(2):026503, 2010.
- [209] K. M. Beckwith. Ebl tricks: Improving ebl performance for writing nanostructure arrays over large areas. 2013.
- [210] J. C. McDonald, D. C. Duffy, J. R. Anderson, D. T. Chiu, H. Wu, O. J. A. Schueller, and G. M. Whitesides. Fabrication of microfluidic systems in poly(dimethylsiloxane). *ELECTROPHORESIS*, 21(1):27–40, 2000.
- [211] I. Wong and C. Ho. Surface molecular property modifications for poly(dimethylsiloxane) (pdms) based microfluidic devices. *Microfluidics and Nanofluidics*, 7(3):291–306, 2009.
- [212] D. C. Duffy, J. C. McDonald, O. J. A. Schueller, and G. M. Whitesides. Rapid prototyping of microfluidic systems in poly(dimethylsiloxane). *Analytical Chemistry*, 70(23):4974–4984, 1998.
-

- 
- [213] D. S. Saldaña. Fabrication of nanoplasmonic sensor device using electron beam lithography (ebl) and optimization performance for submicron particle detection. Master's thesis, Norwegian University of Science and Technology (NTNU), 2019.
- [214] M. J. Madou. *Manufacturing Techniques for Microfabrication and Nanotechnology*. CRC Press, 2011.
- [215] S. Gupta and A. Bit. *Bioelectronics and Medical Devices*. Woodhead Publishing, 2019.
- [216] L. F. Hoyt. New table of the refractive index of pure glycerol at 20°C. *Industrial & Engineering Chemistry*, 26(3):329–332, 1934.
- [217] H. Ahmed, J. Park, G. Destgeer, M. Afzal, and H. J. Sung. Surface acoustic wave-based micromixing enhancement using a single interdigital transducer. *Applied Physics Letters*, 114(4):043702, 2019.
- [218] K. H. Gilchrist, L. Giovangrandi, R. H. Whittington, and G. T. A. Kovacs. Sensitivity of cell-based biosensors to environmental variables. *Biosensors & Bioelectronics*, 20(7):1397–1406, 2005.
- [219] Belektronig. "SAW GENERATOR BSG". Available: [https://www.belektronig.de/en\\_US/frequency-controller-acoustofluidics/saw-generator-bsg-series](https://www.belektronig.de/en_US/frequency-controller-acoustofluidics/saw-generator-bsg-series). (Accessed: 2021-01-08).
- [220] S. N. A. A. Termizi and S. R. A. Shukor. *Computational Fluid Dynamics of Mixing Performance in Microchannel*. IntechOpen, 2020.
- [221] A. Prasad, J. Choi, Z. Jia, S. Park, and M. R. Gartia. Nanohole array plasmonic biosensors: Emerging point-of-care applications. *Biosensors and Bioelectronics*, 130(9):185–203, 2019.
- [222] K. Nakamoto, R. Kurita, O. Niwa, T. Fujii, and M. Nishida. Development of a mass-producible on-chip plasmonic nanohole array biosensor. *Nanoscale*, 3(12):5067–5075, 2011.
- [223] H. Im, J. N. Sutherland, J. A. Maynard, and S. Oh. Nanohole-based surface plasmon resonance instruments with improved spectral resolution quantify a broad range of antibody-ligand binding kinetics. *Analytical Chemistry*, 84(4):1941–1947, 2012.
- [224] L. Wu, P. Bai, X. Zhou, and E. P. Li. Reflection and transmission modes in nanohole-array-based plasmonic sensors. *IEEE Photonics Journal*, 4(1):26–33, 2012.
- [225] M. Chou and K. Chang. Uv/ozone degradation of gaseous hexamethyldisilazane (hmds). *Chemosphere*, 69(5):697–704, 2007.
- [226] F. H. Dill. Optical lithography. *IEEE Transactions on Electron Devices*, 22(7):440–444, 1975.

- 
- [227] R. Andok, A. Bencurova, P. Nemeč, A. Konečnicková, L. Matay, J. Skriniarova, and P. Hrkút. The az 5214e resist in ebdw lithography and its use as a rie etch-mask in etching thin ag layers in n2 plasma. *Journal of Electrical Engineering*, 64, 2013.
- [228] NTNU NorFab. "Spin coater". Available: <https://www.norfab.no/technologies/chemical-and-biological-methods/ntnu-nanolab/spin-coater/>. (Accessed: 2020-11-23).
- [229] NTNU NorFab. "Reflectometer". Available: <https://www.norfab.no/technologies/characterization/ntnu-nanolab-2/reflectometer/>. (Accessed: 2020-11-23).
- [230] NTNU NorFab. "Mask Aligner MA6". Available: <https://www.norfab.no/technologies/lithography/ntnu-nanolab-2/maskaligner-ma6/>. (Accessed: 2020-11-23).
- [231] NTNU NorFab. "E-Beam evaporator & Sputter AJA". Available: <https://www.norfab.no/technologies/deposition/ntnu-nanolab-2/e-beam-evaporator-sputter-aja-international/>. (Accessed: 2020-11-23).
- [232] NTNU NorFab. "Wire Bonder". Available: <https://www.norfab.no/technologies/packaging/ntnu-nanolab-2/wire-bonder/>. (Accessed: 2020-11-23).



# Fabrication Recipe For a Nanoplasmonic Sensor

The fabrication recipe for the nanoplasmonic sensors utilized in this master thesis is presented. The process is produced by Ribe [159] and later validated by Saldaña [213].

1. Cleaning of glass substrate
  - Clean with acetone, rinse in isopropanol (IPA). Dry with nitrogen  $N_2(g)$
  - Plasma cleaner for 5 minutes with oxygen ( $O_2$ ). 50% power / 50% oxygen
2. Dehydration bake
  - Type: Soft baking
  - 250°C for 5 minutes
3. HMDS deposition
  - Chemical vapor deposition
  - Desiccator with HMDS over night
4. Spin coating of photoresist
  - Positive photoresist: CSAR 6200.13
  - Speed of 1000 rpm for 6 seconds with an acceleration of 1000 rpm/sec
  - Speed of 5750 rpm for 60 seconds with an acceleration of 1000 rpm/sec

- 
5. Soft bake
    - 150°C for 1 minute
  6. Spin coating of conductive layer
    - Protective coating PMMA Electra 92 AR-PC 5090.02
    - Speed of 1000 rpm for 2 seconds with an acceleration of 1000 rpm/sec
    - Speed of 2000 rpm for 60 seconds with an acceleration of 1000 rpm/sec
  7. Pre-exposure soft bake
    - Type: Soft baking
    - 90°C for 2 minutes
  8. EBL exposure
    - Parameters determined by the photoresist CSAR 6200.13
    - Dose: 172.5  $\mu\text{C}/\text{cm}^2$
    - Current: 5 nA
  9. Development
    - Developer DI water: Substrate submerged in DI water for 60 seconds to dissolve PMMA Electra 92 AR-PC 5090.02
    - Developer AR 6000-546: Substrate submerged in AR 6000-546 for 60 seconds to dissolve the resisting photoresist layers
    - Stopper: MIBK/IPA with a ratio of 1:3 for 2-3 seconds
    - Rinse in IPA and dry with  $N_2(\text{g})$
  10. Metallization with electron beam evaporator
    - Metal: Ti/Au
    - Thickness: 5 nm / 200 nm
    - Rate: 5  $\text{\AA}/\text{sec}$
  11. Lift-off
    - Ultrasonic bath with stripper for 90 seconds
    - Rinse in acetone and IPA. Dry with  $N_2(\text{g})$

# Appendix B

## Fabrication Recipe For a Microfluidic Channel

The fabrication recipe for the microfluidic channels utilized in this master thesis is produced by Ribe [159] and later validated by Saldaña [213]. The detailed fabrication process is presented below.

1. Cleaning of the silicon substrate
  - Clean with acetone and rinse in isopropanol (IPA). Dry with nitrogen  $N_2(g)$
  - Plasma cleaner for 5 minutes with  $O_2$ . 50% power / 50% oxygen
2. Dehydration bake
  - Type: Soft baking
  - 250°C for 5 minutes
3. Spin coating of photoresist
  - Negative photoresist: SU-8 3050. Desired thickness of 50  $\mu m$
  - Initial speed: 500 rpm for 12 seconds. Rampage: 250 rpm/sec
  - Final speed: 3000 rpm for 46 seconds. Rampage: 250 rpm/sec
4. Soft bake
  - 90°C for 15 minutes



- 
5. Maskless Aligner (MLA) Exposure – 375 nm wavelength laser
    - Dose:  $2000 \text{ mJ/cm}^2$
  6. Post-exposure bake
    - Type: Soft baking
    - $65^\circ\text{C}$  for 1 minute, then  $95^\circ\text{C}$  for 4 minutes
  7. Development
    - Submerged in developer mr-Dev 600 for 5 minutes
    - Rinse with acetone and IPA. Dry with  $N_2(\text{g})$
  8. Tridecafluoro-silane deposition
    - Desiccator under vacuum for a few seconds
    - Leave for 1-2 hours
  9. PDMS application
    - PDMS: Base/curing agent with ratio of 10:1. Mixed by stirring for  $\sim 5$  minutes
    - Dry in oven at  $65^\circ\text{C}$  for 2 hours
    - Pierce inlets
    - Bond the microchannel to the substrate. Place in the plasma cleaner for 30 seconds with  $O_2$  at 50% with 20% power
    - Dry in an oven at  $65^\circ\text{C}$  for 5 minutes to finish the cross-linking
  10. Curing and peeling

# Fabrication Recipe For an Interdigital Transducer

The fabrication recipe for the interdigital transducers utilized in this master thesis is produced by Ribe [159] and presented beneath.

1. Cleaning of the  $LiNbO_3$  substrate
  - Clean with acetone and rinse in isopropanol (IPA). Dry with nitrogen  $N_2(g)$
  - Plasma cleaner for 5 minutes with  $O_2$ . Power 50% / 50% oxygen
2. Dehydration bake
  - Type: Soft baking
  - 100°C for 5 minutes
3. Spin coating of photoresist
  - Positive photoresist AZ 5214E. Desired thickness of 1.5  $\mu m$
  - Speed of 4000 rpm for 46 seconds. Rampage: 4000 rpm/sec
4. Soft bake
  - 95°C for 90 seconds
5. MLA Exposure – 405 nm wavelength laser
  - Dose: 27  $mJ/cm^2$

- 
6. Image reversal bake
    - 113°C for 2 minutes
  7. MA-6 flood exposure
    - Dose: 200  $mJ/cm^2$
  8. Development
    - Developer AZ726 MIF for 40 seconds. The last 10 seconds under agitation
    - Rinse in DI water and dry with  $N_2(g)$
  9. Metallization with electron beam evaporator
    - Metal: Ti/Au
    - Thickness: 5 nm / 80 nm
    - Rate: 5 Å/sec
  10. Lift-off
    - Ultrasonic bath with acetone for 1 minute at 50°C two times
  11. Wire bonding
    - 25  $\mu m$  gold wires

# Fabrication Materials, Chemicals, and Instruments

## D.1 Substrates

**Glass:** A glass substrate with a 2" diameter is used for the nanoplasmonic sensor fabrication due to its transparency and low cost. HMDS, for enhanced adhesion, and PMMA Electra 92 AR-PC 5090.02, for conductivity and electron dissipation, are two additional fabrication steps performed to enable the use of a glass substrate for spectroscopy analysis.

**Silicon:** For the fabrication of the microchannel, a 2" diameter silicon wafer is utilized.

**Lithium Niobate:** The lithium niobate ( $LiNbO_3$ ) wafer is an electrically conductive substrate, which possesses piezoelectric effects. The interdigital transducers are made on these substrates to generate and detect surface acoustic waves.

## D.2 Chemicals

**Acetone, isopropanol, and nitrogen:** The three fluids; acetone, isopropanol (IPA), and nitrogen ( $N_2(g)$ ) are used for the substrate cleaning. The wafers at the NTNU Nanolab are provided from different suppliers and may obtain particles attached to the substrate surface. Acetone and IPA are selected to eliminate residues due to their low density and boiling point. The wafers are immersed in acetone, rinsed with IPA, and dried with  $N_2(g)$  to remove contaminants.

---

**Hexamethyldisilazane (HMDS):** HMDS appears as a clear liquid at room temperature and is considered as a priming process. It is used for improving the resist adhesion and is applied for silanization of the surface by vapor deposition. The oxide surface reacts with the HMDS, creating strong bonds at the surface. However, some free bonds are left to assure reactions between the surface and the photoresist, which enhances the adhesion. Good adhesion of the photoresist is essential to ensure the integrity of pattern/electrical characteristic transfer [225].

**Resists (photoresists and electron beam resists):** Resists are light-sensitive organic compounds that can be applied as thin-film coatings on surfaces where a pattern is to be delineated [226]. When exposed to UV light or an electron beam, the resist will experience a change in solubility in a developer solution. The resist can be selected from a variety of physical properties according to its purpose. Some of these characteristics are sensitivity, contrast, etch resistance, resolution, surface tension, film thickness, and adhesion. The resist can be divided into two main categories: positive or negative resist. In a positive resist, the exposed regions become more soluble in the developer, causing the structures to break. On the other hand, for a negative resist, the exposed regions are cross-linked, which makes them hardened and less soluble. In this case, the non-exposed regions will dissolve in contact with the developer.

- Nanoplasmonic sensor: The photoresist utilized to obtain the desired pattern is CSAR 6200.13. It is a positive photoresist with a suitable resolution to produce nanoholes with a diameter equal to or smaller than  $400 \mu\text{m}$ . Another benefit is that CSAR 6200.13 has an acceptable sensitivity to provide a controlled and stable developer step later in the fabrication process.
- Microchannel: SU-8 3050 is a negative photoresist. It is selected based on the comparison between SU-8 3050 and mr-DWL 40 performed by Álvarez [201]. Álvarez found that SU-8 3050 was the best-suited photoresist for the microchannel fabrication due to a shorter total fabrication time and better pattern features.
- Interdigital transducer: In general AZ 5214E is a positive photoresist. However, it is frequently used as a negative photoresist during image reversal due to its thermal stability and dry etch resistance [227]. The image reversal capability of the resist is obtained by a special cross-linking agent which becomes active at temperatures above  $110^\circ$  and only in the exposed areas of the resist [227].

**Conductive layer:** A conductive layer of PMMA Electra 92 AR-PC 5090.02 is applied to the substrate surface of the nanoplasmonic sensors after the photoresist to ensure the dissipation of charges during the electron exposure. The thin conductive layer creates a path for the electrons to escape from the surface. This is an important step to achieve a good final pattern result.

---

**Developer:** A developer is a solution that will remove unexposed negative resist or exposed positive resist. For each resist, a specific developer is recommended for removal. The developing time is determined by the exposure dose. In this master thesis, three different developers are utilized. The substrate is submerged in the developer under the development process.

- Nanoplasmonic sensor: The solvent-based developer AR 600-546 is applied to remove the positive CSAR 6200.14 photoresist. It is a relatively weak developer, enabling longer developing time, increased control, and higher resolution without significant erosion.
- Microchannel: mr-Dev 600 is a solvent-based developer complementing the negative photoresists SU-8 3050.
- Interdigital transducer: AZ726 metal ion free, or AZ726 MIF, is a developer where tetramethylammonium hydroxide (TMAH) is added in water with surface-active substances (surfactants) for spreading and wetting of the surface. It is used in combination with the photoresist AZ 5214E.

After development, the substrates are rinsed with a stopper to end the developing process, then cleaned with IPA and dried with  $N_2(g)$ .

**Lift-off chemical:** For the nanoplasmonic sensor, the lift-off chemical Remover AR 600-71 is used to remove excess photoresist and metal layer deposition after development. To enhance the photoresist removal, mechanical stress is added to an ultrasonic bath to peel off the remaining photoresist on the surface.

**Poly(dimethylsiloxane) (PDMS):** PDMS is a silicon-based organic elastomer that is isotropic and homogeneous with optical transparency down to  $\sim 300$  nm [204]. The elastomer is typically supplied in a two-component kit with a base (vinyl-terminated PDMS) and a curing agent (copolymers of methylhydrosiloxane and dimethylsiloxane mixed with a platinum complex) [159].

**Trichloro(1H,1H,2H,2H-perfluorooctyl)silane:** Trichloro(1H,1H,2H,2H-perfluorooctyl)silane is a fluorine-based silane which forms self-assembled monolayers on different substrates. It is a biocompatible polymer obtaining low surface energy and is mainly used to modify surfaces with superhydrophobic properties.

## D.3 Instruments

The fabrication processes are intricate, consisting of multiple fabrication steps and instruments. This can be seen from the fabrication recipes in the Subsections 3.2.1-3.2.4 and Appendices A-C.

---

The instruments used to fabricate the nanoplasmonic sensors are a plasma cleaner, desiccator, spin coater, reflectometer, EBL Elionix, DIC microscope, AJA sputter and evaporator, and an SEM microscope. The microchannels are developed by using a plasma cleaner, spin coater, and maskless aligner (MLA-150) with a 375 nm wavelength laser. The interdigital transducers are made with a plasma cleaner, spin coater, MLA-150 with a 405 nm wavelength laser, mask aligner (MA-6), AJA sputter and evaporator, and wire bonder.

**Plasma cleaner:** The plasma system can be used for cleaning, removing photoresist, or for activation of surfaces. Oxygen from ambient air or an external supply is utilized in the system. The substrate surface is both physically and chemically cleaned by ion bombardment and ionized gas, respectively. The ions from the oxygen break the organic compound chains, reducing the number of particles originally attached to the surface.

**Desiccator:** The desiccator is used to deposit a thin monolayer of HMDS by chemical vapor deposition. The layer of HMDS can promote the adhesion between the substrate and the resist. A small quantity of HMDS is placed in a holder in the desiccator together with the substrate. Vacuum is applied for easier evaporation of the HMDS in the chamber. After some time, the chamber is exposed to air, which makes the HMDS particles predicate and form a thin homogeneous HMDS layer on the substrate surface.

**Spin coater:** The spin coater has several operating characteristics such as cleaning, etching, developing, and coating. At the NTNU Nanolab facility, the single wafer spin processor is compatible with solvents, strong bases, and acids [228]. The spin coater consists of a chuck, a chamber with a nitrogen purge, and a control panel for parameter selection. In this master thesis, the spin coater is used for resist coating on different substrate types. The substrate is loaded and maintain on the chuck by vacuum. A specific amount of resist based on the desired thin film thickness is applied in the center of the substrate with a pipette. For the photoresist utilized in this master thesis, the time, speed, and acceleration are selected to obtain the desired thin film thickness.

**Reflectometer:** The reflectometer analyzes reflected light from the substrate surface to determine dielectric films, film thickness, and optical constants of the semiconductor. The reflectometer can measure optically smooth film thicknesses such as semiconductor process films (e.g. resists, oxides, and polysilicon) and optical coatings, including flat panel display films (e.g. polyimides, resist, cell gaps) and hardness and anti-reflection coatings [229].

**EBL Elionix:** The NTNU Nanolab facility possesses an Elionix ELS-G100, which is a 100KV EBL system and 100MHz pattern generator. The instruments have two second-electron (SE) detectors and one back-scattered electron (BSE) detector. The detectors function as height sensors to maintain the sample in focus during exposure. For this master thesis, the EBL Elionix creates the pattern on the photoresist through electron beams for the nanoplasmonic sensors.

---

**Maskless aligner (MLA) 150:** The maskless aligner 150 (MLA-150) is a high-power laser tool for direct writing. Hence, there is no need for a preparation of a photomask to transfer the pattern to the resist. The system has two laser sources with wavelengths of 375 nm and 405 nm. The method is fast and flexible, great for prototyping, and gives typically a resolution of 2  $\mu m$ .

**Mask aligner (MA-6):** The mask aligner MA-6 utilizes ultraviolet light to pattern the resist through a photomask. The instrument has five different exposure modes; vacuum, low vacuum, soft, hard, and proximity. The MA-6 can also be used to perform flood exposure by filtering wavelengths to 320 nm, 365 nm, or 405 nm [230].

**DIC microscope:** The differential interference contrast (DIC) microscope is an instrument for the characterization of the sample after the development process. The performance of the development process is inspected to determine if the sample surface is acceptable for metal deposition.

**AJA sputter and electron beam evaporator:** The AJA sputter and electron beam evaporator is used for thin film deposition by either sputtering or electron beam evaporation. Thin-film deposition by sputtering occurs when the atoms of the desired deposition metal are removed from their surface by bombardment with ionized argon atoms. These metal atoms will impact the substrate, coating the surface with a thin metal film. Thin-film deposition by an electron beam evaporator is executed by sweeping an electron beam over the target surface. This is executed in a high vacuum chamber, enabling free evaporation of the target atoms, transforming them into a gaseous phase. These atoms will form a solid coating through their precipitation. The deposition thickness is controlled by a quartz crystal monitor and the deposition rate can be varied from 1  $\text{\AA}/s$  to 10  $\text{\AA}/s$  [231].

**Scanning electron microscope:** The scanning electron microscope (SEM) is utilized for the characterization of the final features of the substrate. The sample surface is imaged by electrons. Through in-lens detectors (BSE and SE), an exceptional contrast-to-noise ratio can be obtained, and by utilizing a low acceleration voltage, the contrast and resolution can be optimized.

**Wire bonder:** A wire bonder is used to make electrical connections to electronic devices by attaching a very thin wire to the system [232]. Ball bonding, wedge bonding, and compliant bonding are variants of bonding connection methods.





## Calibration Equipment

### E.1 Additional Equipment for Microfluidic Mixing Experiments

- **Fluids:** Sulforhodamine B (fluorescent dye) is used with DI water to reach a 0.25% sulforhodamine B concentration.
- **ThermoFisher Scientific Finnpipette F2 pipette:** For handling 100-1000  $\mu\text{L}$  fluid contents. Utilized for creating the desired concentration of DI water and sulforhodamine B.
- **VWS analog vortex mixer 230V Fixed speed:** For mixing of the sulforhodamine B and DI water to obtain a homogeneous fluid.
- **Micro medical tubing:** To transport the fluids from the syringe pumps to the microchannel inlets and the collecting tube after the microchannel outlet.
- **Tube:** To collect the mixed fluid leaving the outlet of the microchannel.
- **Syringe needles:** To store the fluid content of DI water and the fluorescent mixture separately in the syringe pumps.
- **Syringe tips:** Used to attach the micro medical tubing with the syringe needles.
- **Needle:** Used to attach the micro medical tubing with the inlets and outlet of the microchannel.

---

## E.2 Additional Equipment for Nanoplasmonic Experiments

- **Fluid mixtures:** Deionized (DI) water and glycerol mixtures obtaining 10%, 30%, 50%, and 70% glycerol content.
- **Menzel-Gläser coverslips:** 18x18 mm with 0.13-0.16 mm thickness. Applied to accomplish an even distribution of the fluid mixture on the sample.
- **ThermoFisher Scientific Finnpiquette F2 pipette:** For handling 2-20  $\mu\text{L}$  fluid contents. Utilized to apply the desired quantity of fluid mixture on the sample.
- **VWR pipel tips:** Used to dispense and release specific volumes of the fluid mixture.
- **VWS analog vortex mixer 230V Fixed speed:** Utilized to stir the glycerol mixtures to obtain a homogeneous fluid.
- **Tweezer:** To handle the sample in the platform area and during the cleaning process.
- **Isopropanol (IPA) and beaker:** IPA is poured into a glass beaker to remove excess glycerol from the sample.
- **Paper:** Used to remove excess DI water or glycerol mixture on the sample. Also used after IPA cleaning for glycerol concentrations.

# Appendix F

## Mixing Performance

**Table F.1:** Numerical values of the mixing efficiency for IDT-1 of the 40 MHz IDT design.

IDT design	Flow rate [ $\mu\text{L}/\text{h}$ ]	Power [mW]					
		0	500	1000	1500	2000	2370
40 MHz IDT-1	500	25.70	49.95	77.41	93.05	94.02	97.30
	1000	23.36	37.22	55.47	73.54	94.35	95.74
	1500	23.40	32.41	56.30	76.62	91.22	94.55
	2000	22.12	27.87	44.46	62.54	86.82	93.25
	2500	21.91	31.17	43.45	59.97	85.01	92.27

**Table F.2:** Numerical values of the mixing efficiency for IDT-2 of the 40 MHz IDT design.

IDT design	Flow rate [ $\mu\text{L}/\text{h}$ ]	Power [mW]					
		0	500	1000	1500	2000	2500
40 MHz IDT-2	500	18.06	60.76	79.49	95.44	94.55	95.87
	1000	25.26	59.25	73.23	92.08	94.39	94.63
	1500	22.30	43.10	65.89	80.20	88.20	93.01
	2000	22.14	37.49	53.78	67.93	85.89	89.70
	2500	22.02	36.46	52.78	70.24	79.48	88.33

**Table F.3:** Numerical values of the mixing efficiency for the dual IDT of the 40 MHz IDT design.

IDT design	Flow rate [ $\mu\text{L}/\text{h}$ ]	Power [mW]					
		0	300	500	1000	1400	1500
40 MHz Dual IDT	500	25.46	63.92	86.42			
	1500	24.48		72.56	90.28	95.31	
	2500	22.04		49.13	77.64		91.61

**Table F.4:** Numerical values of the mixing efficiency for IDT-1 of the 80 MHz IDT design.

IDT design	Flow rate [ $\mu\text{L}/\text{h}$ ]	Power [mW]					
		0	500	1000	1500	2000	2340
80 MHz IDT-1	500	26.08	42.66	60.69	75.72	89.97	92.97
	1000	21.42	36.04	51.25	69.55	86.22	91.81
	1500	22.40	34.91	49.60	64.00	72.64	86.97
	2000	21.11	30.24	45.03	53.63	72.40	74.26
	2500	20.59	26.09	37.46	52.04	66.86	74.42

**Table F.5:** Numerical values of the mixing efficiency for IDT-2 of the 80 MHz IDT design.

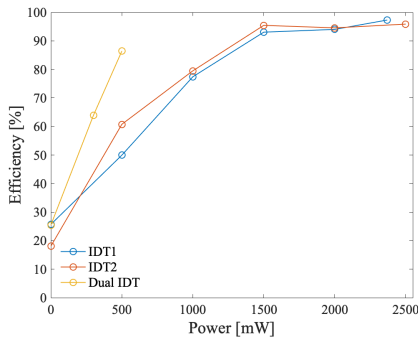
IDT design	Flow rate [ $\mu\text{L}/\text{h}$ ]	Power [mW]					
		0	500	1000	1500	2000	2500
80 MHz IDT-2	500	21.94	47.01	67.45	93.85	95.79	97.91
	1000	20.12	40.77	62.41	83.52	94.15	97.16
	1500	21.89	35.60	49.10	78.37	87.51	94.03
	2000	18.73	31.74	49.13	69.37	78.00	86.78
	2500	19.05	33.88	46.68	60.90	74.75	84.78

**Table F.6:** Numerical values of the mixing efficiency for the dual IDT of the 80 MHz IDT design.

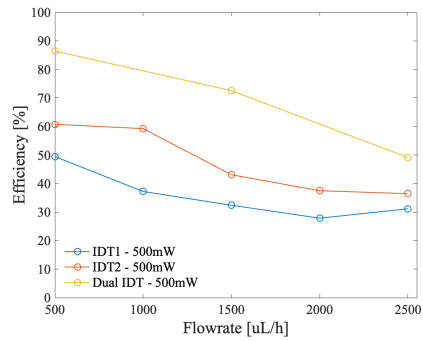
IDT design	Flow rate [ $\mu\text{L}/\text{h}$ ]	Power [mW]				
		0	500	1000	1500	2000
80 MHz Dual IDT	500	22.48	54.08	96.60	97.93	
	1000	21.26	53.97	93.25	97.70	
	1500	19.40	45.00	85.46	95.76	
	2000	19.34	41.16	69.49	95.81	
	2500	19.51	42.52	71.69	93.82	95.47
	3000	19.38	30.02	66.78	76.44	94.95
	4000	19.94	43.96	62.69	80.87	93.24

**Table F.7:** Numerical values of the mixing efficiency for IDT-2 of the 120 MHz IDT design.

IDT design	Flow rate [ $\mu\text{L}/\text{h}$ ]	Power [mW]					
		0	500	1000	1500	1800	1850
120 MHz IDT-2	500	25.40	39.51	53.47	71.04	87.52	
	1000	24.05	35.20	47.25	65.36		81.52
	1500	23.70	35.39	50.11	58.96		63.07

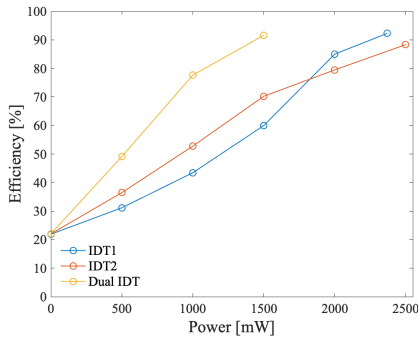


(a) Fixed flow rate of  $500 \mu\text{L}/\text{h}$ .

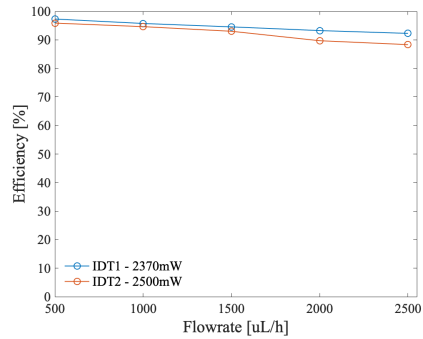


(b) Fixed power of 500 mW.

**Figure F.1:** Comparison of the mixing efficiencies for IDT-1, IDT-2, and dual IDT for the 40 MHz IDT design at a fixed flow rate of  $500 \mu\text{L}/\text{h}$  and fixed power of 500 mW.

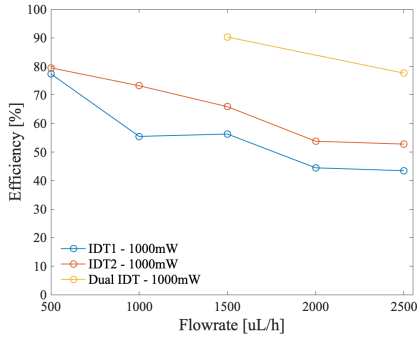


(a) Fixed flow rate of  $2500 \mu\text{L}/\text{h}$ .

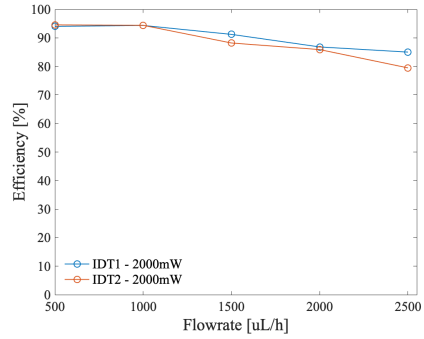


(b) Fixed power of 2500 mW.

**Figure F.2:** Comparison of the mixing efficiencies for IDT-1, IDT-2, and dual IDT for the 40 MHz IDT design at a fixed flow rate of  $2500 \mu\text{L}/\text{h}$  and fixed power of 2500 mW.

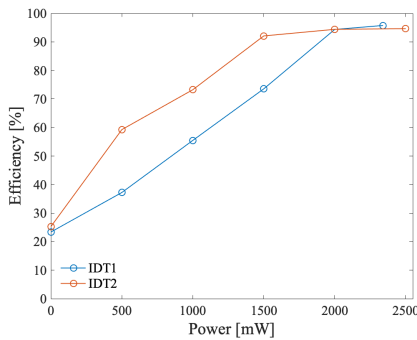


(a) Fixed power of 1000 mW.

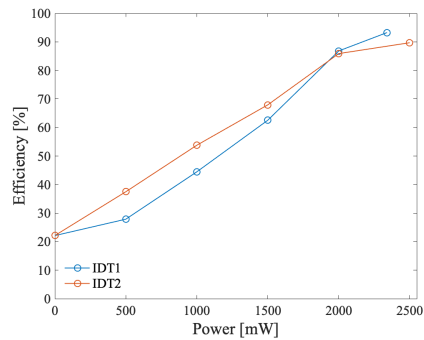


(b) Fixed power of 2000 mW.

**Figure F.3:** Comparison of the mixing efficiencies for IDT-1 and IDT-2 for the 40 MHz IDT design at fixed power of 1000 and 2000 mW.

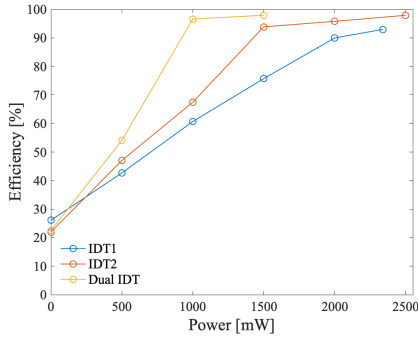


(a) Fixed flow rate of 1000  $\mu\text{L}/\text{h}$ .

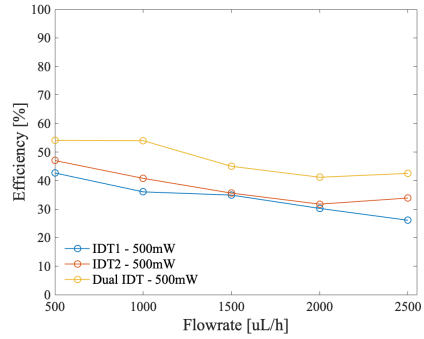


(b) Fixed flow rate of 2000  $\mu\text{L}/\text{h}$ .

**Figure F.4:** Comparison of the mixing efficiencies for IDT-1 and IDT-2 for the 40 MHz IDT design at a fixed flow rate of 1000 and 2000  $\mu\text{L}/\text{h}$ .

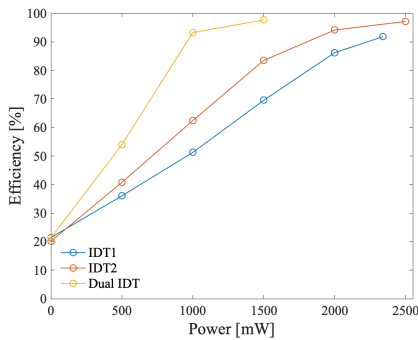


(a) Fixed flow rate of 500  $\mu\text{L}/\text{h}$ .

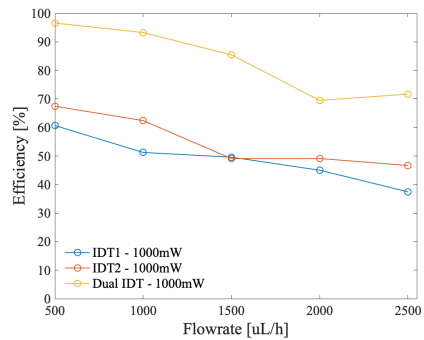


(b) Fixed power of 500 mW.

**Figure F.5:** Comparison of the mixing efficiencies for IDT-1, IDT-2, and dual IDT of the 80 MHz IDT design at a fixed flow rate of 500  $\mu\text{L}/\text{h}$  and fixed power of 500 mW.



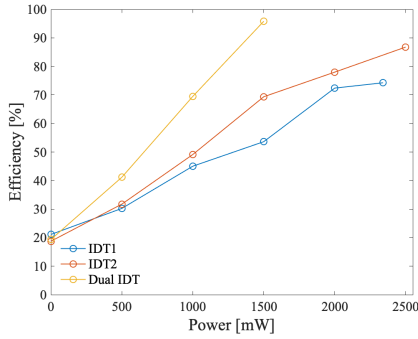
(a) Fixed flow rate of 1000  $\mu\text{L}/\text{h}$ .



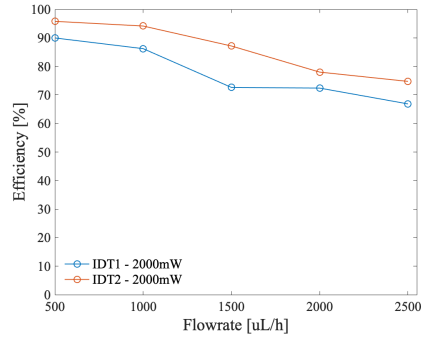
(b) Fixed power of 1000 mW.

**Figure F.6:** Comparison of the mixing efficiencies for IDT-1, IDT-2, and dual IDT of the 80 MHz IDT design at a fixed flow rate of 1000  $\mu\text{L}/\text{h}$  and fixed power of 1000 mW.



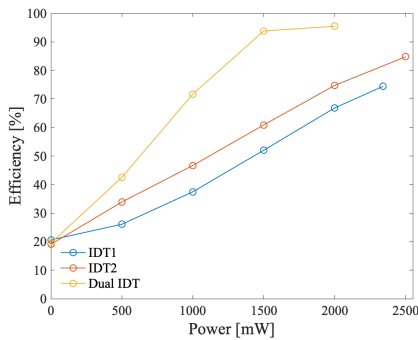


(a) Fixed flow rate of 2000  $\mu\text{L}/\text{h}$ .

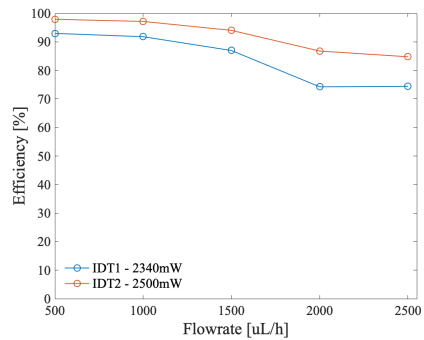


(b) Fixed power of 2000 mW.

**Figure F.7:** Comparison of the mixing efficiencies for IDT-1, IDT-2, and dual IDT of the 80 MHz IDT design at a fixed flow rate of 2000  $\mu\text{L}/\text{h}$  and IDT-1 and IDT-2 at fixed power of 2000 mW.

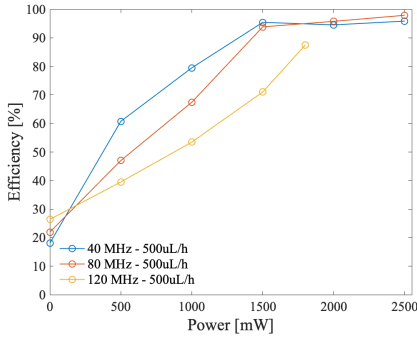


(a) Fixed flow rate of 2500  $\mu\text{L}/\text{h}$ .

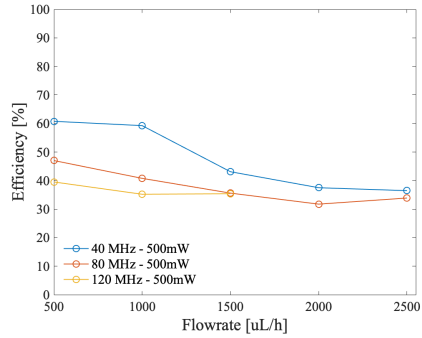


(b) Fixed power of 2500 mW.

**Figure F.8:** Comparison of the mixing efficiencies for IDT-1, IDT-2, and dual IDT of the 80 MHz IDT design at a fixed flow rate of 2500  $\mu\text{L}/\text{h}$  and IDT-1 and IDT-2 at fixed power of 2500 mW.

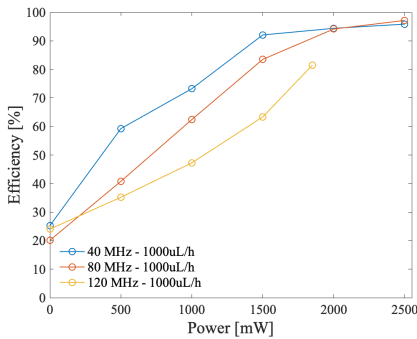


(a) Fixed flow rate of 500  $\mu\text{L}/\text{h}$ .

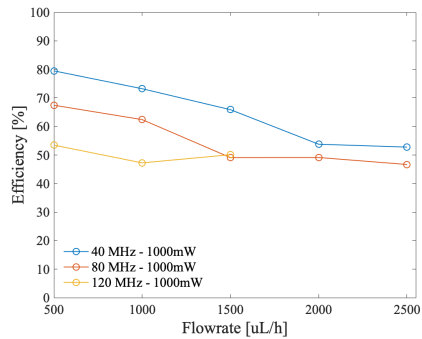


(b) Fixed power of 500 mW.

**Figure F.9:** Comparison of the mixing efficiencies for IDT-2 of the 40 MHz, 80 MHz, and 120 MHz IDT designs at a fixed flow rate of 500  $\mu\text{L}/\text{h}$  and fixed power of 500 mW.



(a) Fixed flow rate of 1000  $\mu\text{L}/\text{h}$ .



(b) Fixed power of 1000 mW.

**Figure F.10:** Comparison of the mixing efficiencies for IDT-2 of the 40 MHz, 80 MHz, and 120 MHz IDT designs at a fixed flow rate of 1000  $\mu\text{L}/\text{h}$  and fixed power of 1000 mW.

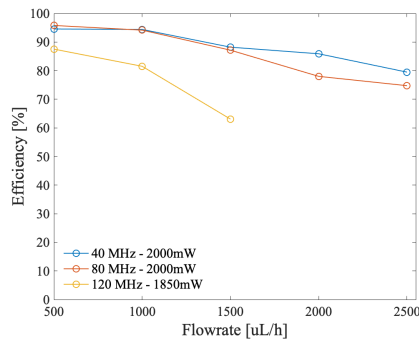
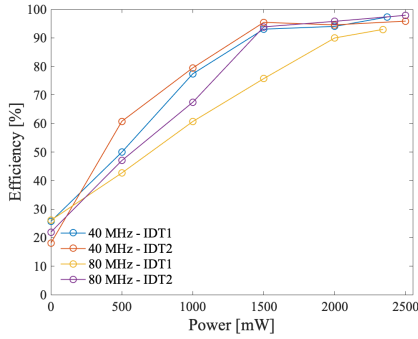
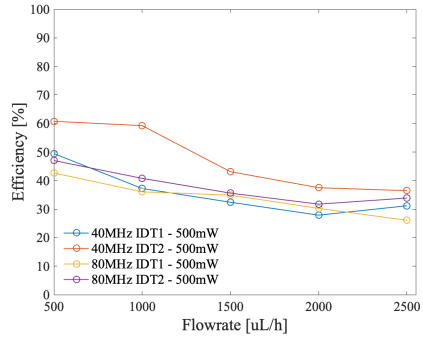


**Figure F.11:** Comparison of the mixing efficiencies for IDT-2 of the 40 MHz, 80 MHz, and 120 MHz IDT designs at fixed power of 2000 mW.

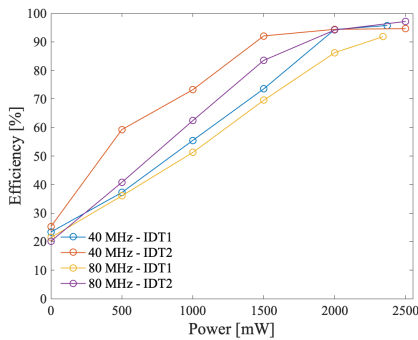


(a) Fixed flow rate of 500  $\mu\text{L}/\text{h}$ .

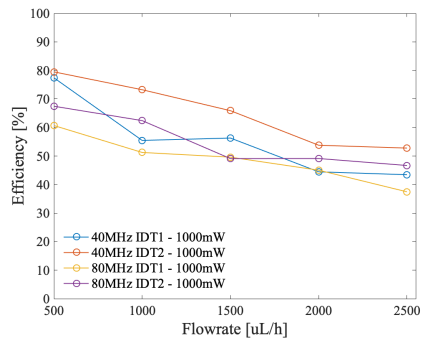


(b) Fixed power of 500 mW.

**Figure F.12:** Comparison of the mixing efficiencies for single IDT of the 40 MHz and 80 MHz IDT designs at a fixed flow rate of 500  $\mu\text{L}/\text{h}$  and fixed power of 500 mW.

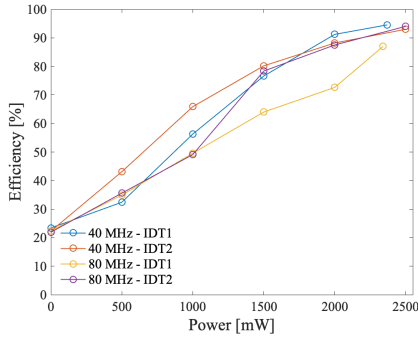


(a) Fixed flow rate of 1000  $\mu\text{L}/\text{h}$ .

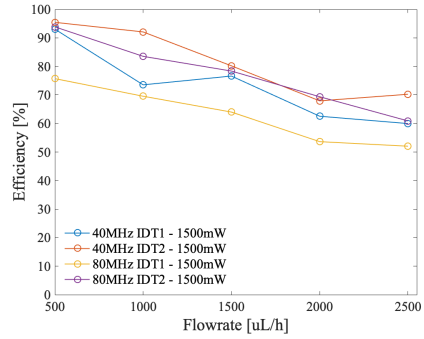


(b) Fixed power of 1000 mW.

**Figure F.13:** Comparison of the mixing efficiencies for single IDT of the 40 MHz and 80 MHz IDT designs at a fixed flow rate of 1000  $\mu\text{L}/\text{h}$  and fixed power of 1000 mW.

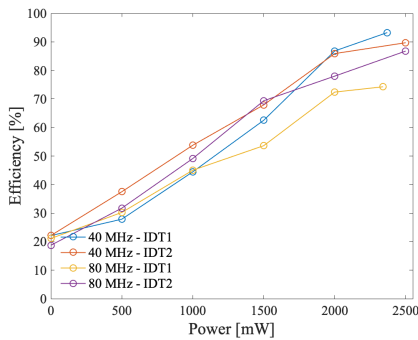


(a) Fixed flow rate of 1500  $\mu\text{L}/\text{h}$ .

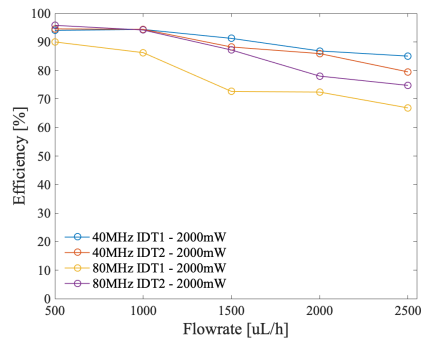


(b) Fixed power of 1500 mW.

**Figure F.14:** Comparison of the mixing efficiencies for single IDT of the 40 MHz and 80 MHz IDT designs at a fixed flow rate of 1500  $\mu\text{L}/\text{h}$  and fixed power of 1500 mW.

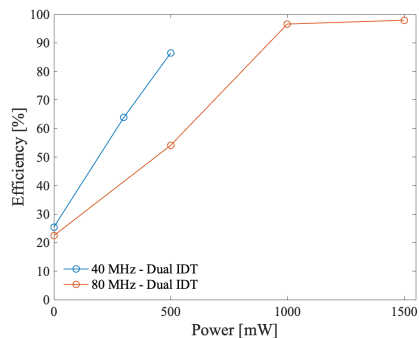


(a) Fixed flow rate of 2000  $\mu\text{L}/\text{h}$ .

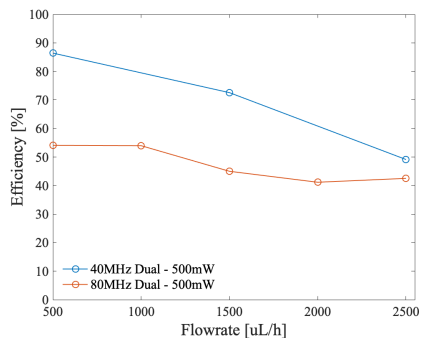


(b) Fixed power of 2000 mW.

**Figure F.15:** Comparison of the mixing efficiencies for single IDT of the 40 MHz and 80 MHz IDT designs at a fixed flow rate of 2000  $\mu\text{L}/\text{h}$  and fixed power of 2000 mW.



(a) Fixed flow rate of 500  $\mu\text{L}/\text{h}$ .



(b) Fixed power of 500 mW.

**Figure F.16:** Comparison of the mixing efficiencies for the dual IDT of the 40 MHz and 80 MHz IDT designs at a fixed flow rate of 500  $\mu\text{L}/\text{h}$  and fixed power of 500 mW.

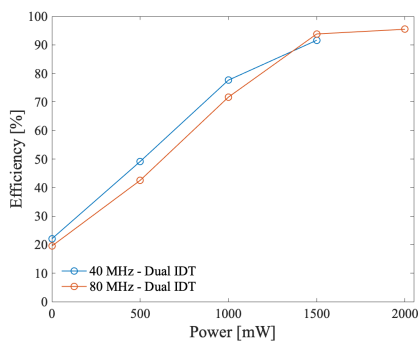


**Figure F.17:** Comparison of the mixing efficiencies for the dual IDT of the 40 MHz and 80 MHz IDT designs at a fixed flow rate of 2500  $\mu\text{L}/\text{h}$ .

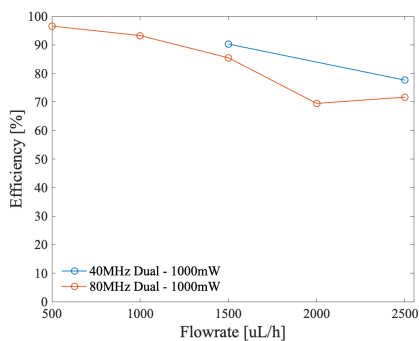
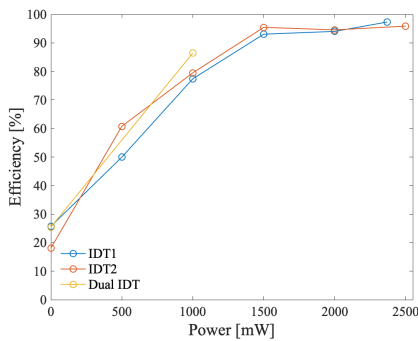
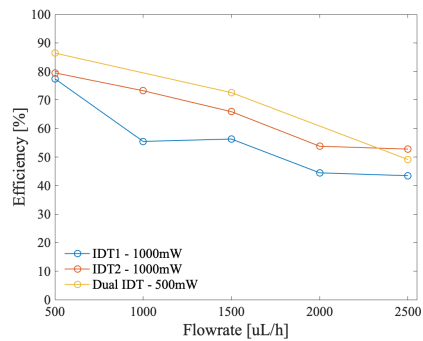


**Figure F.18:** Comparison of the mixing efficiencies for the dual IDT of the 40 MHz and 80 MHz IDT designs at fixed power of 1000 mW.



(a) Fixed flow rate of  $500 \mu\text{L}/\text{h}$ .



(b) Fixed power of 1000 mW for the single IDTs and 500 mW for the dual IDT.

**Figure F.19:** Comparison of the mixing efficiencies for IDT-1, IDT-2, and dual IDT of the 40 MHz IDT design at a fixed flow rate of  $500 \mu\text{L}/\text{h}$  and fixed power of 1000 mW for the single IDTs and 500 mW for the dual IDT.

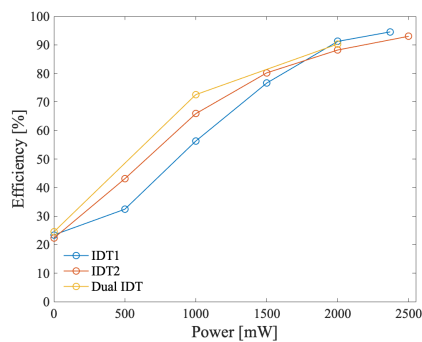
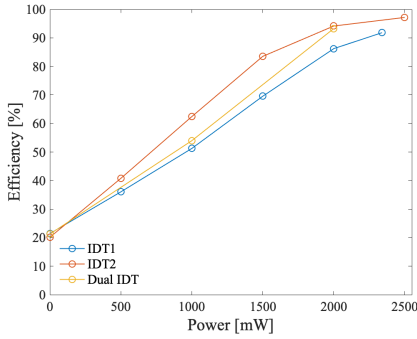
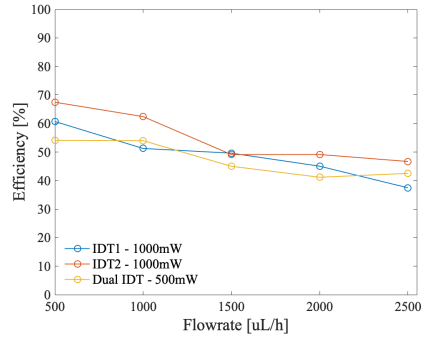


**Figure F.20:** Comparison of the mixing efficiencies for IDT-1, IDT-2, and dual IDT of the 40 MHz IDT design at a fixed flow rate of  $1500 \mu\text{L}/\text{h}$  for equal energy inputs into the system for the single and dual IDTs.

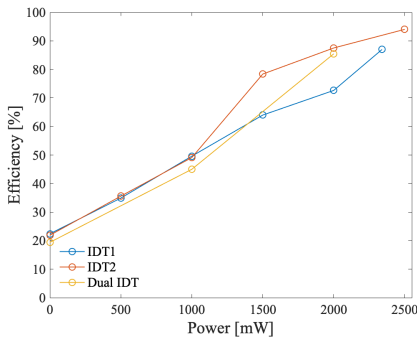


(a) Fixed flow rate of  $1000 \mu\text{L}/\text{h}$ .

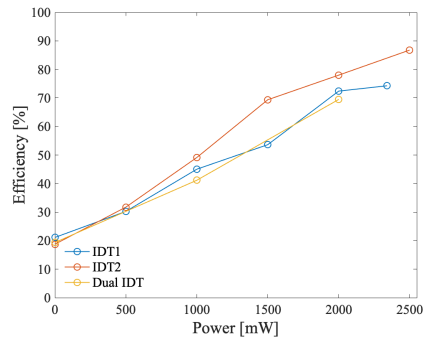


(b) Fixed power of  $1000 \text{ mW}$  for the single IDTs and  $500 \text{ mW}$  for the dual IDT.

**Figure F.21:** Comparison of the mixing efficiencies for IDT-1, IDT-2, and dual IDT of the  $80 \text{ MHz}$  IDT design at a fixed flow rate of  $1000 \mu\text{L}/\text{h}$  and fixed power of  $1000 \text{ mW}$  for the single IDTs and  $500 \text{ mW}$  for the dual IDT.



(a) Fixed flow rate of  $1500 \mu\text{L}/\text{h}$ .



(b) Fixed flow rate of  $2000 \mu\text{L}/\text{h}$ .

**Figure F.22:** Comparison of the mixing efficiencies for IDT-1, IDT-2, and dual IDT of the  $80 \text{ MHz}$  IDT design at a fixed flow rate of  $1000 \mu\text{L}/\text{h}$  and  $2000 \mu\text{L}/\text{h}$  for equal energy inputs into the system for the single and dual IDTs.

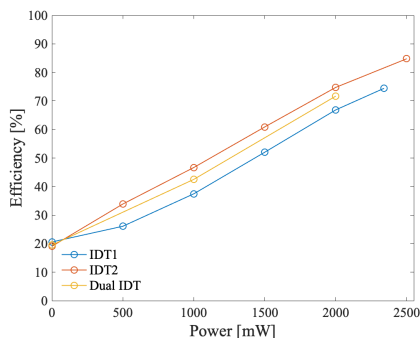
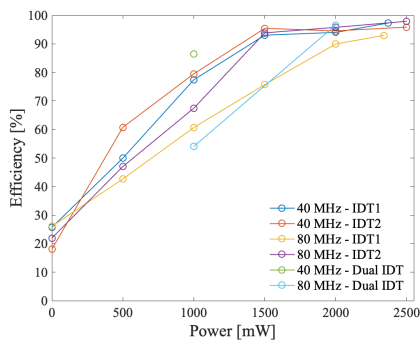
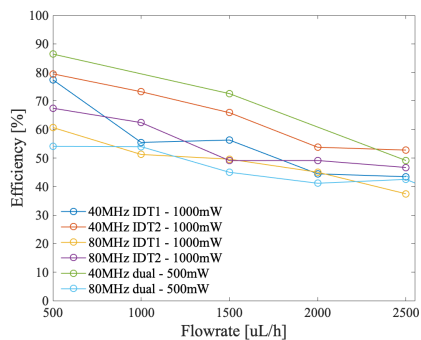


**Figure F.23:** Comparison of the mixing efficiencies for IDT-1, IDT-2, and dual IDT of the 80 MHz IDT design at a fixed flow rate of  $2500 \mu\text{L}/\text{h}$  for equal energy inputs into the system for the single and dual IDTs.



(a) Fixed flow rate of  $500 \mu\text{L}/\text{h}$ .



(b) Fixed power of 1000 mW for the single IDTs and 500 mW for the dual IDT.

**Figure F.24:** Comparison of the mixing efficiencies for IDT-1, IDT2, and dual IDT of the 40 MHz and 80 MHz IDT designs at a fixed flow rate of  $500 \mu\text{L}/\text{h}$  and fixed power of 1000 mW for the single IDTs and 500 mW for the dual IDT.



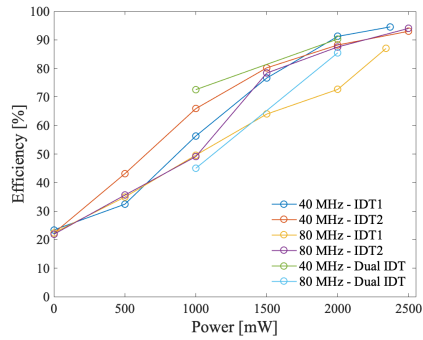


**Figure F.25:** Comparison of the mixing efficiencies for IDT-1, IDT-2, and dual IDT of the 40 MHz and 80 MHz designs at a fixed flow rate of  $1500 \mu L/h$  for equal energy inputs into the system for the single and dual IDTs.

